A STUDY OF THE FIELD MODULATED GENERATOR SYSTEM

By

CHI-CHENG TSUNG

Diploma
Taiwan Provincial
Taipei Institute of Technology
Taipei, Taiwan
1957

Master of Science
Oklahoma State University
Stillwater, Oklahoma
1972

Submitted to the Faculty of the Graduate College
of the Oklahoma State University
in partial fulfillment of the requirements
for the Degree of
DOCTOR OF PHILOSOPHY
December, 1976

A STUDY OF THE FIELD MODULATED GENERATOR SYSTEM

Thesis Approved:

R. Ramakumar.

Thesis Adviser

Wm. L. Hughes

E. K. McFarlane

Dean of the Graduate College

PREFACE

This thesis study is concerned with the development of a mathematical model for the field modulated generator system (FMGS) under some idealizing assumptions using a combination of analytical and numerical methods. The validity of the theoretical work is experimentally verified. The results of this study are expected to provide a basic understanding of the interaction of various parameters in the operation of FMGS and lead to guideline for better design, scale-up and control of this system.

First of all, I wish to express my sincere appreciation to Dr. R. Ramakumar, my thesis advisor, for stimulating my interest in this research and for spending much of his valuable time in fruitful discussions. His constant encouragement and great insight into the overall system made this thesis possible.

I appreciate the assistance and help of Dr. H. Jack Allison, the chairman of my doctoral committee. I also appreciate the help and guidance of the other members of my committee, Dr. Eugene K. McLachlan, Dr. William L. Hughes, and Dr. Daniel D. Lingelbach.

The financial supports received from Project Themis in the early stages of my doctoral program and from the National Science Foundation RANN Grant No. GI-39457 and from Grant No. ERDA/NSF-AER 75-00647 during thesis research are gratefully acknowledged. Special thanks are extended to the School of Electrical Engineering, Oklahoma State University,

for providing the experimental facilities and needed support during the experimental investigations.

I do deeply appreciate Dr. Edward L. Shreve, Dr. Craig S. Sims, and Dr. Emmett J. Pybus and their families for their concern and advice on a personal level. A note of thanks is given to Dr. John P. Chandler for his teaching excellence and programming help in solving the non-linear equations encountered in Chapter II.

My special gratitude is expressed to Dr. and Mrs. Julian Q. Lynd for their constant help and generosities in sharing with us their home and domestic warmth during our stay in Stillwater.

I would like to thank to my wife, Syou-Tao Chiang, daughter, Ju-Fong, and Son, Ken-Tseon, for their understanding, patience and sacrifices during my study in this country.

Finally, I would like to dedicate this thesis to my parents, brothers, and sisters for their constant encouragement and unwavering confidence in my ability to successfully complete my doctoral program.

TABLE OF CONTENTS

LIST OF TABLES

LIST OF FIGURES

LIST OF SYMBOLS

$a_{\ell o}$	Normalized Fourier coefficient, dc component as defined by Equation (2.4.20).
a_{an}, $a_{\ell n}$	Normalized Fourier coefficients; n-th harmonic component as defined by Equation (2.4.14) or (2.4.16).
A	Constant defined by Equation (2.3.29).
A_1	Constant defined by Equation (2.3.19).
A_p	Mean area per pole, m^2.
b_{an}, $b_{\ell n}$	Normalized Fourier coefficients; n-th harmonic component as defined by Equation (2.4.15) or (2.4.17).
B	Constant defined by Equation (2.3.20).
B_r	Maximum air-gap flux density, Wb/m^2.
B_{rav}	Average air-gap flux density, Wb/m^2.
C	Stator tuning (bridge-input) capacitance per phase, F.
C_ℓ	Load capacitance, F.
C_3	Capacitance in the output filter circuit, F.
C_4	Rotor tuning capacitance, F.
d	Mean diameter of the machine in the air-gap, m.
D	Constant defined by Equation (2.3.30).
D_1	Constant defined by Equation (2.3.21).
e_a, e_b, e_c	Instantaneous values of voltages induced in the three stator phase windings, V.
e_s	Instantaneous value of stator search coil voltage, V.
E_d	dc (average) output voltage on load for PBRS model, V.
E_{do}	dc (average) output voltage under no-load conditions for PBRS model, V.

E_1	Maximum value of voltage induced per phase in the stator winding, V.
f	Source frequency, Hz.
f_m	Modulation frequency, Hz.
f_r	Basic alternator (source) frequency, Hz.
$f_1, \ldots, f_6$	Functions defined by Equations (2.3.89) through (2.3.94).
g	Radial air-gap length at pole center, m.
i_a, i_b, i_c	Instantaneous values of phase currents in the three stator windings, A.
i_{ac}, i_{bc}, i_{cc}	Instantaneous values of bridge-input capacitor currents, A.
$i_{a\ell}, i_{b\ell}, i_{c\ell}$	Instantaneous values of bridge-input currents, A.
i_{a1}, i_{b1}, i_{c1}	Instantaneous values of fundamental components of stator currents, A.
i_{cr}	Instantaneous value of current through rotor tuning capacitor, A.
i_e	Instantaneous value of rotor circuit input current, A.
i_ℓ	Instantaneous value of load current, A.
i_r	Instantaneous value of rotor winding current, A.
I_{a1}	Maximum value of i_{a1}, A.
I_{cr}	Maximum value of i_{cr}, A.
I_d	dc (average) output current for PBRS model, A.
I_e	Maximum value of i_e, A.
$I_{e\ rms}$	RMS value of i_e, A.
I_ℓ	Maximum value of i_ℓ, A.
$I_{\ell o}$	Magnitude of dc component of i_ℓ, A.
I_r	Maximum value of fundamental component of i_r, A.
I_{sc}	Maximum value of current measured when stator phase terminals are shorted under ac excitation, A.
I_{rdc}	Rotor input dc current, A.

I_{rms}	RMS value of i_r, A.
I_o	Initial value of source inductor current, A.
I_1	Maximum value of fundamental component of stator phase (source) current, A.
k_d	Distribution factor for stator winding, dimensionless.
k_f	Factor defined by Equation (3.4.2), dimensionless.
k_p	Pitch factor for stator winding, dimensionless.
k_t	Constant defined by Equation (3.4.38), N•m/At.
k_1, k_2	Constants defined by Equation (2.3.22).
k_5, k_6	Constants defined by Equation (2.3.31).
K	Normalizing factor defined by Equation (2.4.5).
K_{an} or $K_{\ell n}$	Normalized magnitude of the n-th harmonic component of source current of phase-a or load current as defined by Equation (2.4.3) or (2.4.8).
$K_{\ell o}$	Normalized magnitude of $I_{\ell o}$ as defined by Equation (2.4.20).
K_{val}	Normalized magnitude of V_{al} as defined by Equation (2.4.12).
K_1	Constant defined by Equation (2.3.34).
K_2	Constant defined by Equation (2.3.25).
ℓ	Active iron length of the machine, m.
L	Stator commutating (source) inductance per phase, H.
L_ℓ	Load inductance, H.
L_r	Rotor winding inductance, H.
L_{re}	Effective inductance of rotor winding, H.
L_3, L_4	Inductors in the output filter circuit.
m	Modulation frequency ratio, (f_r/f_m), dimensionless.
m_f	Fundamental MMF across air-gap as a function of x and t, set-up by the rotor winding, At.

m_r	Resultant fundamental MMF across air-gap, as a function of x and t, At.
M	Mutual inductance between stator and rotor windings, H.
M_a	Maximum value of armature reaction MMF, At.
M_f	Maximum value of fundamental MMF across air-gap set-up by the rotor winding, At.
M_r	Maximum value of fundamental MMF across air-gap, At.
N_r	Number of turns per pole in the rotor winding.
N_s	Number of stator turns in series per phase.
p	Number of poles.
r_1, r_2	Constants defined by Equation (2.3.23).
r_3, r_4	Constants defined by Equation (2.3.32).
R_ℓ	Load resistance, Ω.
t	Time, s.
T	Period as defined by Equation (2.4.21), s.
v_a, v_b, v_c	Instantaneous values of bridge-input voltages, V.
v_{al}	Instantaneous value of fundamental component of phase-a bridge-input voltage, V.
v_ℓ	Instantaneous value of load voltage, V.
v_r	Instantaneous value of rotor circuit input voltage, V.
V_{al}	Maximum value of v_{al}, V.
V_ℓ	Maximum value of v_ℓ, V.
V_L	Voltage drop across low frequency (ω_m) equivalent source impedance, V.
V_r	Maximum value of v_r, V.
V_{rms}	RMS value of v_r, V.
V_o	Initial value of bridge-input (capacitor) voltage, V.

x	Distance along the mean diameter of the machine, m.
X_C	Capacitive reactance of bridge-input capacitor at frequency f_r, Ω.
X_L	Commutating reactance of stator (source) per phase at frequency f_r, Ω.
α_1	Constant defined by Equation (2.3.33).
α_2	Constant defined by Equation (2.3.24).
β	Angle by which e_a leads $\omega_r t = 0$, rad.
β'	Angle defined by Equation (3.3.11), rad.
γ	Value of $\omega_r t$ at which diode pair 1 starts conduction, rad. (See Figures 4, 5 & 40)
δ	Angle by which M_r lags M_f, rad.
δ'	Angle defined by Equation (3.3.9), rad.
θ	Angle which is equal to $\omega_r t$ or ωt, rad.
θ_o	Angle between rotor axis and axis of stator coil at $\omega_r t = 0$, rad.
θ_o'	Angle defined by Equation (3.3.8)
θ_1	Angle which is equal to $(\theta + \theta_o)$, rad.
μ_o	Permeability of free space, $4\pi \times 10^{-7}$, H/m.
ν	Angle by which v_{a1} lags e_a, rad.
ν'	Angle defined by (3.3.10), rad.
ϕ_{an} or $\phi_{\ell n}$	Phase angle of the n-th harmonic component of source current of phase-a or load current as defined by Equation (2.4.4) or (2.4.9), rad.
ϕ_{va1}	Angle by which v_{a1} lags $\omega_r t = 0$, as defined by Equation (2.4.13), rad.
ϕ_{va1}'	Angle defined by Equation (3.3.12), rad.

ϕ_1	Angle by which i_{a1} lags e_a, rad.
ϕ_1'	Angle defined by Equation (3.3.13).
Φ_r	Magnetic flux per pole, Wb.
ω	Source electrical angular frequency, rad/s.
ω_m	Modulation angular frequency, rad/s.
ω_r	Alternator electrical angular frequency, rad/s.

CHAPTER I

INTRODUCTION

1.1 General Literature Survey

Variable-speed adjustable-frequency (VSAF) systems have interested researchers for many years [1]. These systems have several important practical applications. They can serve as variable-voltage variable-frequency power sources for electric drives and ground transportation, deriving their mechanical input from an unregulated shaft. As variable-speed constant-frequency (VSCF) systems, they are useful in vehicle power generation and in the utilization of alternate energy sources such as geothermal and wind.

A variety of variable-speed constant-frequency systems have been proposed. They generally fall into two broad categories.

(A) Differential Methods

(i) Mechanical techniques (variable ratio gears, planetary gear systems, hydraulic pump-motor arrangement, etc.) to obtain constant or nearly constant speed and the use of synchronous or induction generators.

(ii) Electrical techniques (such as feeding slip frequency power to rotor) to obtain constant frequency. Frequency make-up generator is a typical example belonging to this category.

(B) Non-Differential Methods

(i) Static frequency changer; AC-DC-AC (ADA) conversion system.

(ii) Rotary devices that do not employ solid-state switching techniques; AC commutator generators (ACCG).

(iii) Judicious synthesis of rotating machines with solid-state switching devices such as diodes and thyristors.

a) Cycloconverter type frequency changers.

b) Amplitude modulated frequency changer employing square wave modulation.

c) Field modulation and demodulation techniques.

1) High frequency switching.

2) Low frequency switching--Field Modulated Generator System (FMGS) under development at Oklahoma State University.

Mechanical techniques [2] employ various speed control devices and infinitely-variable transmission systems to obtain constant speed from an unregulated shaft. These devices are, in general, heavy, bulky and entail high maintenance costs.

Frequency make-up generator [3,4] employs a rectifier-inverter for processing and feeding slip frequency power to rotor to set up a synchronously rotating air-gap flux. This system requires a large slip-frequency power feeding capability to operate over a wide speed range. Moreover, a complicated procedure is involved in obtaining gating signals, especially when operating 'through' and 'above' synchronous speed.

ADA conversion [5] is a mature technology, developed for use in high-voltage dc (HVDC) transmission systems. Operation of ADA systems

in conjunction with power grids is fairly well understood. Applications are limited by the cost of power processing and filtering equipment.

ACCG [6,7] utilizes the frequency changing characteristics of a commutator machine to obtain a constant frequency output using commutator and brushes. This scheme requires a large and expensive machine. In addition, commutators require constant maintenance.

Cycloconverter type frequency changers [8,9] use solid-state switching devices to obtain constant-frequency ac from a variable frequency ac source. Drawbacks associated with this scheme are the extensive filtering required to obtain an acceptable output waveform, expensive control devices, less adaptive to sudden input and speed changes, and the necessity of switching thyristors at high voltage and power levels. They have reactive power output capability and are quite expensive, suitable for use only in specialized applications.

Amplitude modulated frequency changer [10] is an ac-to-ac power converter. It modulates a sinusoidal carrier with a square-wave whose frequency is a submultiple of the carrier frequency and whose zero crossings coincide with the zero crossings of the carrier. Output is obtained by suppressing one sideband component automatically by the proper choice of phase differences between the three modulating signals used for the three phases. This system, when operating under a continuously varying shaft speed, will have difficulties in commutation and filtering as well. Only discrete frequencies are available from this form of naturally commutated modulation.

Field modulation and demodulation techniques use an electromagnetic modulator in the form of exciting the rotating field coil with alternating current at the desired low frequency. Output is obtained by

demodulation techniques which employ either a high frequency or a low frequency switching scheme.

Wickson [11] has proposed a high frequency switching scheme employing a set of solid-state switching devices synchronized with the positive and negative half-cycles of the high frequency waveform with relative phase reversal to produce the required low frequency at the output terminals. Because of the use of transistors as switching devices, this type of generator is practical only in small ratings (up to about 10 kVA).

Bernstein and Schmitz [12] proposed a low frequency switching scheme using thyristors for envelope switching. For three-phase operation, the demodulator circuit is made up of two three-phase half-wave rectifier circuits connected in parallel (6-phase double-way rectifier). This scheme results in line-to-line short circuits during commutation and necessitates derating of the machine to allow for additional losses that occur due to the presence of harmonics. Additional loss and poor regulation result due to the insertion of "source resistors" between stator terminals and rectifiers.

Another low frequency switching scheme, developed by Hughes et al. [13], employs a parallel-bridge rectifier system (PBRS) to obtain a full-wave rectified waveform (with some harmonics superimposed) which is then switched by a thyristor inverter at nearly zero voltage points to obtain a constant frequency output [14,15]. The use of PBRS eliminates line-to-line short circuits and capacitors at bridge-inputs reduce excitation requirements, improve regulation and efficiency.

Figure 1 shows a block diagram of the field modulated generator system (FMGS) for single-phase output. In this diagram, FMGS is

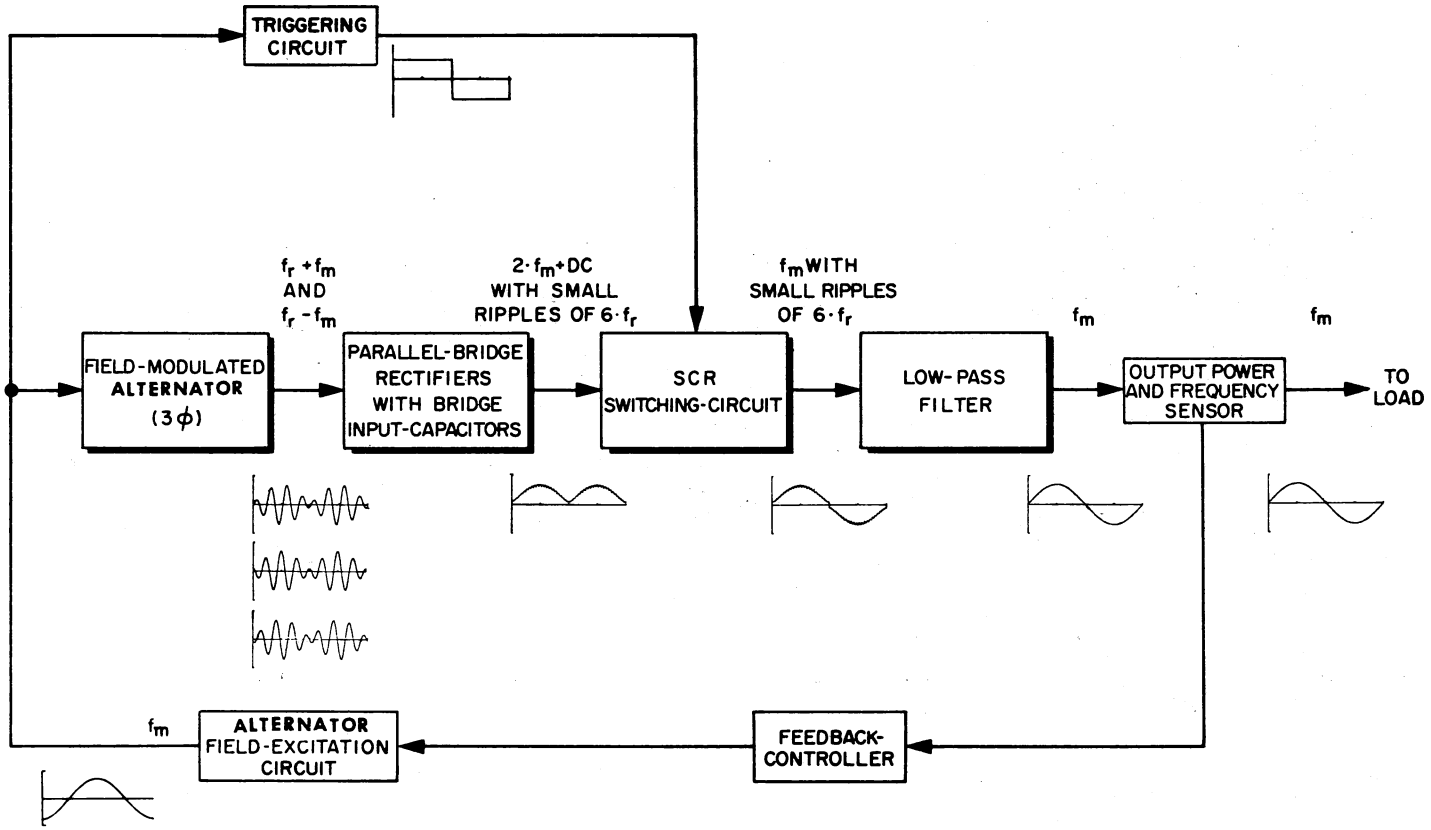

Figure 1. FMGS Block Diagram

represented by eight different functional blocks. It is clear from this block diagram that field modulated alternator, PBRS with bridge-input capacitors, SCR switching circuit, and low-pass filter constitute the essential parts of the system. The waveforms at various points and their phase relationships shown in the block diagram provide a pictorial view of the operation of the system. For three-phase output, three separate (core stacks) magnetic circuits, PBRS, thyristor inverters and filtering circuits are required [16]. This particular scheme is believed to have advantages over others in size, weight, regulation and cost. Field modulated generator systems have been under development and study at Oklahoma State University since 1970. A brief description of the operation of the system and a schematic diagram are given in the next Section.

1.2 Description of the Field Modulated Generator System (FMGS)

Figure 2 shows a simplified single-phase schematic of the field modulated frequency down converter system. It is built around a high-reactance high-frequency (approximately 10 times the output frequency required) three-phase alternator. Terminals of the wound-rotor are brought out through a conventional slip ring arrangement, although salient-pole structure is equally suited for this purpose. Both rotor and stator are laminated to minimize iron losses. The six stator leads are connected to three full-wave bridges as shown, one across each of the phases. Outputs of the bridges are tied in parallel across the load through a silicon controlled rectifier switching system. Stator tuning capacitors C are connected across each of the stator windings to

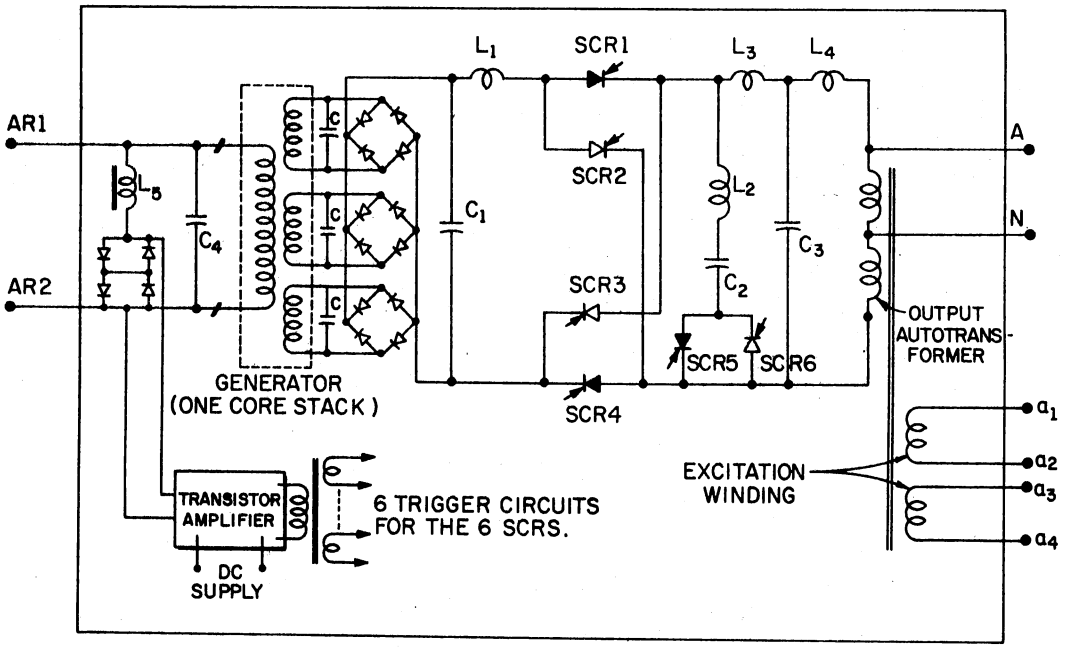

Figure 2. Simplified Single-Phase Schematic of the Field Modulated Generator System

decrease excitation requirements (both watts and vars). The small capacitor C_1 and the inductor L_1 prevent any rapid voltage variations that may occur at the machine terminals from damaging the silicon controlled rectifiers. Main switching process is accomplished by the four controlled rectifiers, SCR1 through SCR4. Commutating circuit consisting of L_2, C_2 and the controlled rectifiers SCR5 and SCR6 aid in this switching process, especially when the load is not purely resistive.

At the start of one half of the low frequency cycle, SCR1, SCR4 and SCR5 are triggered together. Capacitor C_2 charges up to the peak value of the full-wave rectified voltage appearing across the parallel bridge arrangement. At the end of this half cycle, SCR2, SCR3 and SCR6 are triggered together and simultaneously SCR1, SCR4 and SCR5 are shut-off.

The voltage across capacitor C_2 now is of such a polarity (top + and bottom -) as to help turn off SCR1 and SCR4. In this process, capacitor C_2 discharges and starts to recharge in the opposite direction through SCR6 to the peak value of the voltage as before. At the end of this second half cycle, the voltage across capacitor C_2 (top -, bottom +) will aid in shutting off SCR2 and SCR3. This charging and discharging of C_2 is repeated once every half cycle. The size of C_2 depends on the accuracy of the timing of the SCR trigger signals and on the reactive nature of the load. The small inductance L_2 is provided as a safeguard against sudden voltage variations from appearing across SCR5 and SCR6. Filtering the switched output is performed by the tuned circuit consisting of filter capacitor C_3, inductors L_3 and L_4 and the output autotransformer. In addition to filtering, capacitance C_3 aids the system to handle lagging power factor loads.

The field winding is excited by an ac power source of frequency f_m. Since excitation fixes the output frequency, care must be excercised in the design of this part of the system. In case the system is required to be completely independent, an inverter-dc source combination must be used to excite the field. The dc power might come from an exciter alternator-rectifier unit mounted on the same shaft as the main generator. The volt-ampere capacity required of the excitation source can be greatly decreased by partial tuning of the field circuit by properly choosing capacitor C_4. In series with inductance L_5, a back-to-back diode combination is used to obtain the triggering signals. The rotor input current lags the rotor applied voltage by nearly $\pi/2$. The current through L_5 and the diodes also lags the input voltage by nearly $\pi/2$. Thus the current through the back-to-back diode combination is nearly in

phase with the rotor input current. The voltage picked up across this diode combination is a square wave with zero crossings coincident with the zeros of the rotor winding current. This square wave is fed to a high frequency transformer with six secondaries. The output of each secondary is used to trigger one of the six controlled rectifiers.

Several single-phase and three-phase FMGS prototypes with ratings ranging from 10 to 60 kVA have been designed, fabricated and tested at Oklahoma State University over the past six years.

1.3 Problem Statement

The objective of this thesis research is to analyze and develop a mathematical model for the FMGS. The first step in the analysis of any complicated system is to develop an idealized model under certain simplifying assumptions. These assumptions can be relaxed one by one or in groups in later investigations to study the ensuing modifications and changes in the behavior of the system. The idealized model developed in this thesis should lead to a basic understanding of the interaction of various parameters in the operation of the FMGS. Results of this study are expected to provide guidelines for better designs and scale-up of this system.

1.4 Outline of the Method of Study

Analysis and modeling of FMGS is complicated by the inherent rectification, inversion and filtering processes involved and the manner in which their effects are reflected back into the machine and affect its behavior. Presence of stator and rotor tuning capacitors further complicates the problem by providing closed paths for harmonic currents to

circulate. Factors such as accuracy of timing of thyristor triggering signals, power factor of the load, design of the magnetic circuit, range of rotor speed variations and nonlinearities introduced by circuit elements, all influence the overall performance of the system.

The task of modeling FMGS is approached by dividing the system into several sub-systems for separate studies. The results of all these analyses are then combined to obtain the model sought for. In the following paragraphs, brief descriptions of the procedures used to study the sub-systems and the manner in which the results are brought together are given.

(A) Study of the Parallel-Bridge Rectifier System (PBRS) With Bridge-Input Capacitors

As mentioned earlier, the nucleus of the FMGS is an alternator feeding into a PBRS with bridge-input capacitors. Therefore, a thorough study of PBRS with bridge-input capacitors is the logical first-step in modeling the entire system.

Both experimental and analytical techniques were employed in developing understanding of the operation of PBRS with bridge-input capacitors. Circuit differential equations were set-up for various voltages and currents in the idealized model of this sub-system. These equations were solved using proper initial values and boundary conditions. In this process, two angles, γ and β, related to the 'on' and 'off' conditions of various diodes, play a key role. Values of these angles were numerically evaluated by solving a set of non-linear algebraic equations obtained by application of proper boundary conditions. Theoretical values of γ and β are presented with non-dimensional circuit

constants (X_L/R_ℓ) and (X_L/X_C) as parameters. Experimental verification of these theoretical results provide good correlation and confidence in the theory developed.

(B) Harmonic Analysis of PBRS Waveforms

Incorporating solid-state power conditioning devices at the outputs of conventional rotating machines distorts the waveforms and introduces harmonics in various parts of the system. Harmonic analysis of key waveforms would provide vital information leading to proper approximations in the development of the model. Among the multitude of waveforms in the system, source current i_a, bridge-input voltage v_a, and load current i_ℓ, are of particular interest. Analysis of i_a and v_a provide information that directly affect the operation of the alternator. With a purely resistive load, i_ℓ and v_ℓ are identical and only one (i_ℓ was chosen) need to be analyzed. Analysis of i_ℓ gives data necessary to estimate the amplitude of the modulated envelope and to design the output filter.

Since the expressions for the waveforms are lengthy and involved, numerical methods are used to evaluate Fourier coefficients. Amplitudes of harmonic components are normalized with respect to either the maximum value of voltage induced in the stator (source) winding, or the maximum value of stator (source) current per phase when the bridge-input terminals are short-circuited. Results of this analysis, phase angles and normalized magnitudes, are plotted in graphical form with (X_L/X_C) and (X_L/R_ℓ) as parameters.

(C) Development of Idealized Model

An idealized model for the alternator and PBRS is formed as the first step in the model development. It is known that the waveforms in the system are, in general, non-sinusoidal in nature. However, in the idealized model, only fundamental components are considered. Phase relationships can then be expressed in vector diagram form and the system, it is believed, can be analyzed with reasonable accuracy. Relationships between maximum values of load voltage, current and maximum values of stator (source) current, induced voltage per phase under modulation are derived from the results of PBRS harmonic analysis. These relationships can be coupled with alternator performance equations to form the FMGS model.

(D) Experimental Verification of the Idealized Model

As the final step in the model development, a series of experimental investigations are undertaken to verify the validity of the idealized model. These experiments are designed to verify the model in two stages. In the first stage, PBRS model is verified and in the second, field modulated alternator-PBRS combination is tested and the results correlated with theory.

1.5 Organization of the Thesis

Chapter II presents a theoretical analysis of PBRS with bridge-input capacitors. Results of the harmonic analysis of various voltage and current waveforms are presented in graphical form in terms of normalized values.

Chapter III developes the idealized FMGS model. A detailed analysis is made to establish relationships between various parameters of the

system. The model is developed in the form of performance equations and vector diagrams.

Chapter IV documents the results of experimental investigations conducted to verify the idealized PBRS and FMGS models. Experimental procedures, data and oscillograms are recorded. Theoretical and experimental values are compared and sources of errors are discussed.

The thesis concludes with a presentation of the summary of results and suggestions for further work in Chapter V.

CHAPTER II

PARALLEL-BRIDGE RECTIFIER SYSTEM (PBRS) STUDIES

2.1 Introduction

Electronic power converter systems have been under study at least since the beginning of this century and are continuing to interest researchers [17]. Dortort [18], Witzke et al. [19], and others have made detailed studies of the six-phase double-way and double-wye rectifier schemes. However, these conventional schemes are not suitable for use at the outputs of three-phase high-frequency (approximately 1 kHz) alternators because of their inherent high commutating reactances which will result in line-to-line short circuits during commutation [20]. For such cases, the parallel-bridge rectifier system (PBRS) offers the advantage of eliminating line-to-line short circuits and thereby improving their power output capability and efficiency.

Ramakumar et al. [21], have presented a detailed analysis of the PBRS for both resistive and inductive load conditions when there are no capacitors at bridge-inputs. Results of this analysis have been applied successfully to study the operation of alternators with PBRS under dc excitation [22]. This study demonstrated that fundamental components of source currents obtained from PBRS analysis yield results which agree fairly well with experimental observations.

It is well known that the use of proper stator tuning capacitors

will decrease the excitation requirements and improve the efficiency of an alternator. Similar advantages are present in the case of FMGS also.

The central role of PBRS with bridge-input capacitors in the overall performance of FMGS suggests that this circuit be studied first in detail. Consequently, detailed investigations (both experimental and analytical) of this circuit under resistive load conditions were undertaken [23,24]. This Chapter summarizes the results of the theoretical studies in this area.

Section 2.2 begins with a brief description of PBRS and the circuit model formulated based on idealizing assumptions. The general nature of waveforms is discussed to illustrate the circuit interactions within the idealized model.

Section 2.3 presents the mathematical formulation of circuit differential equations and their solution using proper boundary conditions. The key angles γ and β are introduced and evaluated by solving a set of nonlinear algebraic equations. The evaluated values are plotted with (X_L/X_C) and (X_L/R_ℓ) as parameters.

Section 2.4 discusses the computation of Fourier coefficients for the waveforms of interest. Results of the Fourier analysis are presented in terms of phase angles and normalized magnitudes, plotted with (X_L/X_C) and (X_L/R_ℓ) as parameters.

2.2 Idealized Model and Waveforms

The parallel-bridge rectifier system (PBRS) under study consists of three full-wave bridges with a capacitor across each pair of bridge-input terminals, each combination of full-wave bridge and capacitor being connected to one of the three isolated phases of a three-phase power

supply (or alternator), with their outputs tied in parallel across a variable load resistance.

Figure 3 shows an idealized PBRS model. The source impedance is assumed to be purely reactive. This is a reasonable approximation commonly used in the study of practical systems. If a three-phase alternator is used as the source, then the inductance L will represent the effective commutating inductance of the machine per phase. All diodes are assumed to be ideal switches with zero forward voltage drops and zero reverse currents.

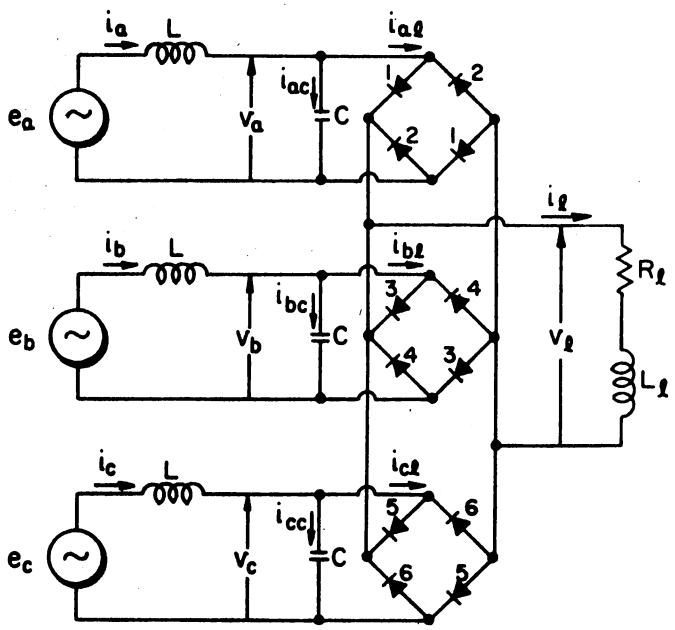

$$e_a = E_1 \sin(\Theta + \beta)$$
$$e_b = E_1 \sin(\Theta + \beta - \tfrac{2\pi}{3})$$
$$e_c = E_1 \sin(\Theta + \beta + \tfrac{2\pi}{3})$$

Figure 3. Idealized PBRS Model

Figure 4 illustrates the load current waveform and its relationship to bridge-input currents of phases a, b and c. It is periodic with a period of $\pi/3$. Within this period, it consists of two specific parts. The first part is formed when only two bridges are conducting with the third phase decoupled from the load (due to the presence of the capacitor) and the second part is the result of simultaneous conduction of all three bridges. In the analysis to follow, a one-half cycle (0 to π) corresponding to the source waveform is chosen. This is divided into six parts and the quantities corresponding to these intervals are marked with subscripts 1 through 6 respectively. As a matter of convenience, the half-cycle corresponding to phase-a is considered. Waveforms for phases b and c will be similar, except for the inherent phase differences of $\pm 2\pi/3$. In Figure 4, intervals 1, 3 and 5 correspond to

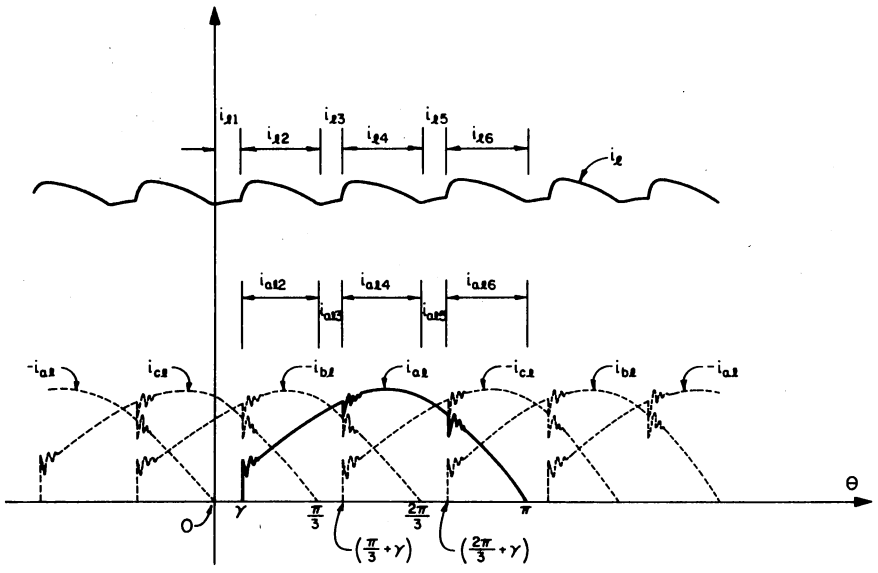

Figure 4. Waveforms of Load Current and Bridge-Input Currents

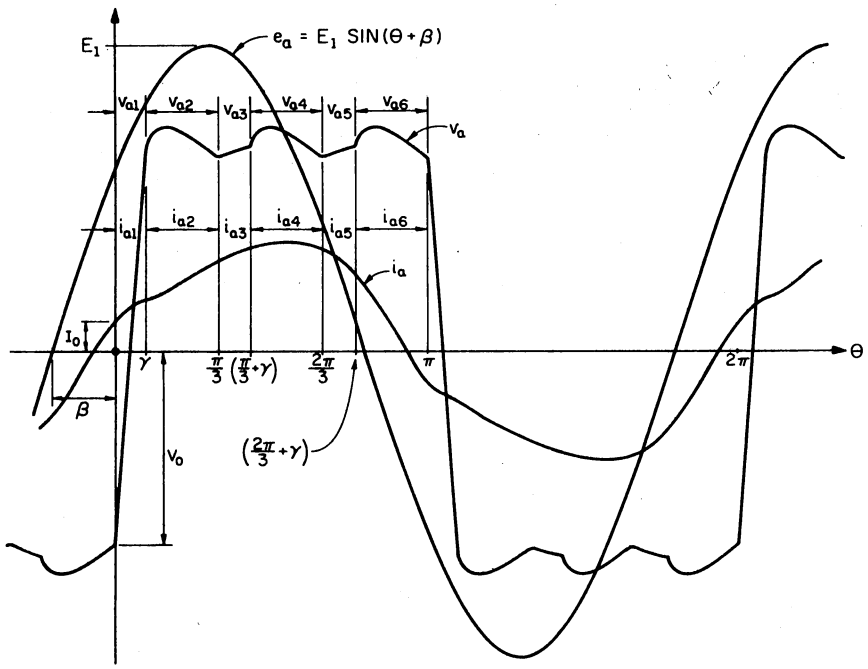

Figure 5. General Nature of Waveforms for Phase-a ($X_L/X_C \simeq 0.04$)

decoupling durations of phases a, c and b; intervals 2, 4 and 6 correspond to simultaneous conduction of all three bridges.

The general nature of waveforms for phase-a is illustrated in Figure 5. It shows the phase relationship between the source voltage e_a, bridge-input voltage v_a and the source current i_a for a small value (around 0.04) of the ratio (X_L/X_C). The significance of the angles γ and β is evident from this Figure. Time zero is chosen such that at $t = 0^-$, diode pair 2 (in Figure 3) stops conducting.

2.3 Circuit Analysis

Expressions for various voltages and currents will be derived in

six stages, marked (A) through (F). Integration constants (k_1, k_2, k_5, k_6) and angles (γ and β) appearing in these expressions will be evaluated towards the end of this Section. The model being analyzed (Figure 3) and the notation used have already been discussed.

(A) Derivation of the Load Current

The instantaneous voltages of the three ideal voltage sources are

$$e_a = E_1 \sin(\omega t + \beta) \tag{2.3.1}$$

$$e_b = E_1 \sin(\omega t + \beta - \frac{2\pi}{3}) \tag{2.3.2}$$

$$e_c = E_1 \sin(\omega t + \beta + \frac{2\pi}{3}) \tag{2.3.3}$$

The currents in each phase circuit in general are (refer Figure 3):

$$i_a = i_{a\ell} + i_{ac} \tag{2.3.4}$$

$$i_b = i_{b\ell} + i_{bc} \tag{2.3.5}$$

$$i_c = i_{c\ell} + i_{cc} \tag{2.3.6}$$

During $0^+ \leq t \leq (\gamma/\omega)^-$, phase-a circuit is decoupled ($i_{a\ell 1} = 0$) from the other two phases as shown in Figure 6. The load current $i_{\ell 1}(t)$ is represented by

$$i_{\ell 1} = -i_{b\ell 3} + i_{c\ell 5} \tag{2.3.7}$$

Assuming ideal diodes, the bridge-input voltage is equal to the load voltage when conduction of a pair of diodes occurs. Circuit equations for phases b and c are

$$-v_{b3} = -e_b + L \frac{di_{b3}}{dt} = R_\ell i_{\ell 1} + L_\ell \frac{di_{\ell 1}}{dt} \tag{2.3.8}$$

$$v_{c5} = e_c - L \frac{di_{c5}}{dt} = R_\ell i_{\ell 1} + L_\ell \frac{di_{\ell 1}}{dt} \tag{2.3.9}$$

Substituting (2.3.2), (2.3.3), (2.3.5) and (2.3.6) into above, the

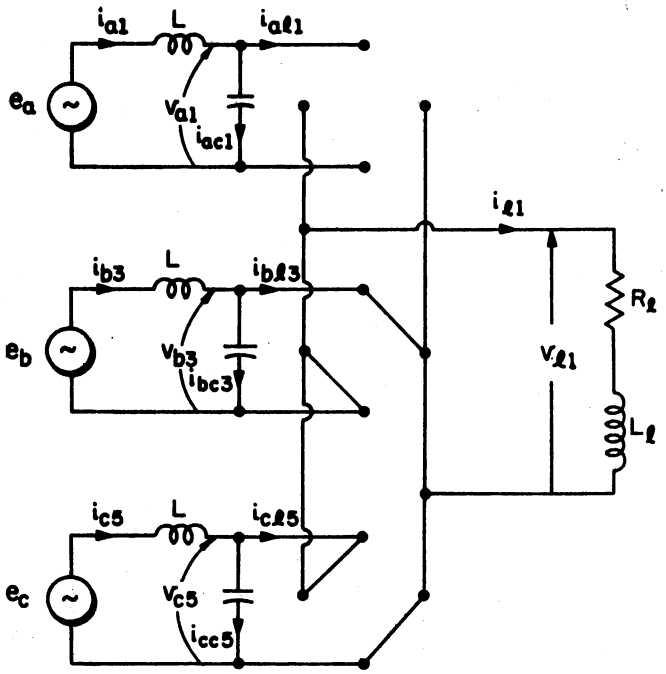

Figure 6. Illustrating the Status of the System During $0^+ \leq t \leq \frac{\gamma}{\omega}^-$

following differential equations are obtained.

$$-E_1 \sin(\omega t + \beta - \tfrac{2\pi}{3}) + L \frac{d}{dt}(i_{b\ell 3} + i_{bc3}) = R_\ell\, i_{\ell 1} + L_\ell \frac{di_{\ell 1}}{dt} \qquad (2.3.10)$$

$$E_1 \sin(\omega t + \beta + \tfrac{2\pi}{3}) - L \frac{d}{dt}(i_{c\ell 5} + i_{cc5}) = R_\ell\, i_{\ell 1} + L_\ell \frac{di_{\ell 1}}{dt} \qquad (2.3.11)$$

Adding (2.3.10) and (2.3.11) results in

$$2R_\ell\, i_{\ell 1} + 2L_\ell \frac{di_{\ell 1}}{dt} + L \frac{di_{\ell 1}}{dt} + L \frac{d}{dt}(-i_{bc3} + i_{cc5}) = \sqrt{3}\, E_1 \cos(\omega t + \beta) \qquad (2.3.12)$$

General expressions for bridge-input capacitance currents are

$$i_{ac} = C \frac{dv_a}{dt} \qquad (2.3.13)$$

$$i_{bc} = C \frac{dv_b}{dt} \tag{2.3.14}$$

$$i_{cc} = C \frac{dv_c}{dt} \tag{2.3.15}$$

Based on (2.3.14) and (2.3.15), following relationship must hold

$$-i_{bc3} + i_{cc5} = 2\,C \frac{d}{dt}\left(R_\ell\, i_{\ell 1} + L_\ell \frac{di_{\ell 1}}{dt}\right) \tag{2.3.16}$$

Substituting (2.3.16) into (2.3.12), and rearranging, differential equation for $i_{\ell 1}$ is obtained.

$$\frac{d^3 i_{\ell 1}}{dt^3} + \frac{R_\ell}{L_\ell}\frac{d^2 i_\ell}{dt^2} + \frac{2L_\ell + L}{2L\,L_\ell\,C}\frac{di_{\ell 1}}{dt} + \frac{R_\ell}{L\,L_\ell\,C}\, i_{\ell 1} = \frac{\sqrt{3}E_1}{2L\,L_\ell C}\cos(\omega t + \beta) \tag{2.3.17}$$

For purely resistive loads, $L_\ell = 0$ and (2.3.17) becomes

$$\frac{d^2 i_{\ell 1}}{dt^2} + A_1 \frac{di_{\ell 1}}{dt} + B\, i_{\ell 1} = D_1 \sin(\omega t + \beta + \frac{\pi}{2}) \tag{2.3.18}$$

where

$$A_1 \equiv \frac{1}{2CR_\ell} \tag{2.3.19}$$

$$B \equiv \frac{1}{LC} \tag{2.3.20}$$

$$D_1 \equiv \frac{\sqrt{3}E_1}{2LCR_\ell} \tag{2.3.21}$$

Solution of (2.3.18) is

$$i_{\ell 1}(t) = k_1\, e^{r_1 t} + k_2\, e^{r_2 t} + \frac{\sqrt{3}E_1}{K_2}\sin(\omega t + \beta - \alpha_2 + \frac{\pi}{2}) \tag{2.3.22}$$

where

$$r_1, r_2 = \frac{-A_1 \pm \sqrt{A_1^2 - 4B}}{2} \tag{2.3.23}$$

$$\alpha_2 \equiv \tan^{-1}\frac{\omega L}{(1 - \omega^2 LC)\,2\,R_\ell} \tag{2.3.24}$$

$$K_2 \equiv \sqrt{(1 - \omega^2 LC)^2 4R_\ell^2 + \omega^2 L^2}$$

and k_1, k_2 are constants to be determined later.

The roots r_1 and r_2 become imaginary when $4B > A_1^2$ which corresponds to $(X_L X_C/R_\ell^2) < 16$.

It is clear from Figure 4 that load current during $(\frac{\gamma}{\omega})^+ \leq t \leq (\frac{\pi}{3\omega})^-$ is defined to be $i_{\ell 2}(t)$ and it results from simultaneous conduction in all three-phases. Therefore,

$$i_{\ell 2} = i_{a\ell 2} - i_{b\ell 4} + i_{c\ell 6} \tag{2.3.26}$$

Differential equation satisfied by $i_{\ell 2}$ can be obtained by procedures similar to the ones used in the derivation of Equation (2.3.17). The result is:

$$\frac{d^3 i_{\ell 2}}{dt^3} + \frac{R_\ell}{L_\ell}\frac{d^2 i_{\ell 2}}{dt^2} + \frac{3L_\ell + L}{3L\,L_\ell\,C}\frac{di_{\ell 2}}{dt} + \frac{R_\ell}{L\,L_\ell\,C}\,i_{\ell 2} = \frac{2E_1}{3L\,L_\ell\,C}\sin(\omega t + \beta + \tfrac{\pi}{3}) \tag{2.3.27}$$

For purely resistive loads, $L_\ell = 0$ and (2.3.27) becomes

$$\frac{d^2 i_{\ell 2}}{dt^2} + A\frac{di_{\ell 2}}{dt} + B\,i_{\ell 2} = D\sin(\omega t + \beta + \tfrac{\pi}{3}) \tag{2.3.28}$$

where

$$A \equiv \frac{1}{3CR_\ell} \tag{2.3.29}$$

$$D \equiv \frac{2E_1}{3LCR_\ell} \tag{2.3.30}$$

Solution of (2.3.28) is

$$i_{\ell 2}(t) = k_5\,e^{r_3 t} + k_6\,e^{r_4 t} + \frac{2E_1}{K_1}\sin(\omega t + \beta - \alpha_1 + \tfrac{\pi}{3}) \tag{2.3.31}$$

where

$$r_3,\ r_4 = \frac{-A \pm \sqrt{A^2 - 4B}}{2} \tag{2.3.32}$$

$$\alpha_1 \equiv \tan^{-1}\frac{\omega L}{(1 - \omega^2 LC)\ 3\ R_\ell} \tag{2.3.33}$$

$$K_1 \equiv \sqrt{(1 - \omega^2 LC)^2 9R_\ell^2 + \omega^2 L^2} \qquad (2.3.34)$$

and k_5, k_6 are constants to be determined later. The roots r_3 and r_4 become imaginary when $4B > A^2$ which corresponds to $(X_L X_C/R_\ell^2) > 36$. This condition is more restictive than the one discussed earlier. For practical systems, circuit parameter values will be restricted to the range $\infty > (X_L X_C/R_\ell^2) > 36$ under rated conditions.

Expressions for $i_{\ell 3}$ and $i_{\ell 5}$ can be obtained from (2.3.22) by replacing t by $(t - \frac{\pi}{3\omega})$ and $(t - \frac{2\pi}{3\omega})$ respectively. Similarly, $i_{\ell 4}$ and $i_{\ell 6}$ can be obtained from (2.3.31) by replacing t by $(t - \frac{\pi}{3\omega})$ and $(t - \frac{2\pi}{3\omega})$ respectively. The expressions for $i_{\ell 3}$ through $i_{\ell 6}$ are summarized below.

$$i_{\ell 3}(t) = k_1 e^{r_1(t - \frac{\pi}{3\omega})} + k_2 e^{r_2(t - \frac{\pi}{3\omega})} + \frac{\sqrt{3}E_1}{K_2} \sin(\omega t + \beta - \alpha_2 + \tfrac{\pi}{6}) \qquad (2.3.35)$$

$$i_{\ell 4}(t) = k_5 e^{r_3(t - \frac{\pi}{3\omega})} + k_6 e^{r_4(t - \frac{\pi}{3\omega})} + \frac{2E_1}{K_1} \sin(\omega t + \beta - \alpha_1) \qquad (2.3.36)$$

$$i_{\ell 5}(t) = k_1 e^{r_1(t - \frac{2\pi}{3\omega})} + k_2 e^{r_2(t - \frac{2\pi}{3\omega})} + \frac{\sqrt{3}E_1}{K_2} \sin(\omega t + \beta - \alpha_2 - \tfrac{\pi}{6}) \qquad (2.3.37)$$

and

$$i_{\ell 6}(t) = k_5 e^{r_3(t - \frac{2\pi}{3\omega})} + k_6 e^{r_4(t - \frac{2\pi}{3\omega})} + \frac{2E_1}{K_1} \sin(\omega t + \beta - \alpha_1 - \tfrac{\pi}{3}) \qquad (2.3.38)$$

(B) Derivation of $i_{a1}(t)$ for $0^+ \leq t \leq \frac{\gamma}{\omega}^+$

At the instant $t = 0^-$, phase-a circuit becomes decoupled from the other two ($i_{a\ell 1} = 0$) with an initial current of I_o in L and an initial

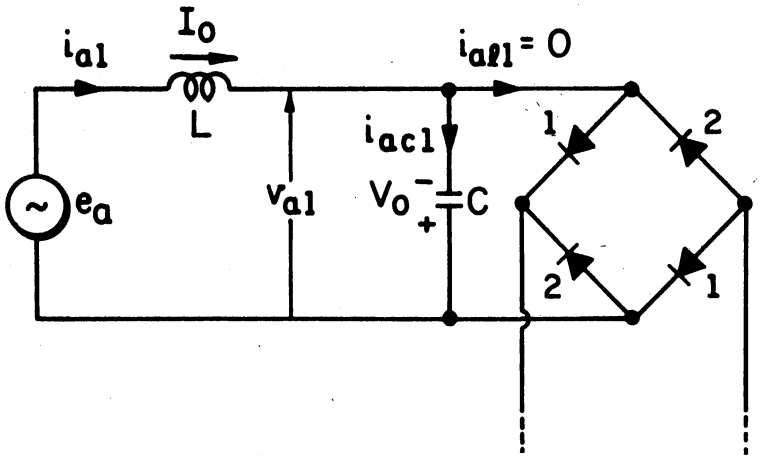

Figure 7. Illustrating the Status of Phase-a Circuit at $t = 0^+$

Voltage of $-V_o$ across C as shown in Figure 7. During this time interval, the circuit equation is

$$L\frac{di_{a1}}{dt} + \frac{1}{C}\int i_{a1}\,dt = E_1 \sin(\omega t + \beta) \tag{2.3.39}$$

Solving (2.3.39) with proper initial conditions yields

$$i_{a1}(t) = \left(I_o - \frac{E_1}{1-\omega^2 LC}\,\omega C\cos\beta\right)\cos\frac{t}{\sqrt{LC}} + \sqrt{\frac{C}{L}}\left(V_o + \frac{E_1}{1-\omega^2 LC}\sin\beta\right)\sin\frac{t}{\sqrt{LC}}$$

$$+ \frac{E_1}{1-\omega^2 LC}\,\omega C\cos(\omega t + \beta) \tag{2.3.40}$$

(C) Derivation of Bridge-Input Current

Define

$$I_{a\ell 2} \equiv i_{a\ell 2}(\gamma/\omega)^+ \tag{2.3.41}$$

Current continuity in L at $t = (\gamma/\omega)$ requires

$$i_{a1}(\gamma/\omega)^- = i_{a2}(\gamma/\omega)^+ \tag{2.3.42}$$

Applying (2.3.4), (2.3.42) becomes

$$i_{a1}(\gamma/\omega)^- = i_{ac2}(\gamma/\omega)^+ + i_{a\ell 2}(\gamma/\omega)^+ \tag{2.3.43}$$

Now, applying (2.3.13) and (2.3.41) to (2.3.43) yields

$$I_{a\ell 2} = i_{a1}(\gamma/\omega)^- - C \left.\frac{dv_{a2}}{dt}\right|_{t = (\frac{\gamma}{\omega})^+} \tag{2.3.44}$$

However, for purely resistive loads,

$$v_{a2}(\gamma/\omega)^+ = R_\ell \; i_{\ell 2}(\gamma/\omega)^+ \tag{2.3.45}$$

Substituting (2.3.45) into (2.3.44) yields

$$I_{a\ell 2} = i_{a1}(\gamma/\omega)^- - C \; R_\ell \left.\frac{di_{\ell 2}}{dt}\right|_{t = (\frac{\gamma}{\omega})^+} \tag{2.3.46}$$

Define

$$I_{a2} \equiv i_{a1}(\gamma/\omega)^- \tag{2.3.47}$$

Differentiating (2.3.31) once and evaluating the result at $t = (\gamma/\omega)$, the following is obtained.

$$\left.\frac{di_{\ell 2}}{dt}\right|_{t = (\gamma/\omega)} = k_5 \; r_3 \; e^{\frac{\gamma r_3}{\omega}} + k_6 \; r_4 \; e^{\frac{\gamma r_4}{\omega}} + \frac{2E_1}{K_1}\,\omega \cos(\gamma + \beta - \alpha_1 + \tfrac{\pi}{3}) \tag{2.3.48}$$

With the help of (2.3.47) and (2.3.48), (2.3.46) can be written as

$$I_{a\ell 2} = I_{a2} - C \; R_\ell \left[k_5 \; r_3 \; e^{\frac{\gamma r_3}{\omega}} + k_6 \; r_4 \; e^{\frac{\gamma r_4}{\omega}} + \frac{2E_1}{K_1}\,\omega \cos(\gamma + \beta - \alpha_1 + \tfrac{\pi}{3})\right] \tag{2.3.49}$$

where, as defined by (2.3.47), I_{a2} is obtained by evaluating (2.3.40) at $t = (\gamma/\omega)$ as given below.

$$I_{a2} = \left(I_o - \frac{E_1}{1-\omega^2 LC}\,\omega\, C \cos\beta\right) \cos\frac{\gamma}{\omega\sqrt{LC}} + \sqrt{\frac{C}{L}}\left(V_o + \frac{E_1}{1-\omega^2 LC}\sin\beta\right)\sin\frac{\gamma}{\omega\sqrt{LC}}$$

$$+ \frac{E_1}{1-\omega^2 LC}\,\omega\, C \cos(\gamma + \beta) \tag{2.3.50}$$

At $t = (\gamma/\omega)^+$, diode pair 1 starts to conduct and bridge-input voltage v_{a2} becomes equal to the load voltage $v_{\ell 2}$ (refer Figures 4 and 5). This condition is expressed by the following equation.

$$v_{a2} = e_a - L \frac{di_{a2}}{dt} = R_\ell i_{\ell 2} + L_\ell \frac{di_{\ell 2}}{dt} = v_{\ell 2} \tag{2.3.51}$$

Using (2.3.1), (2.3.4) and (2.3.13) in the above equation and rearranging, relationship between bridge-input current $i_{a\ell 2}$, source voltage e_a and load current $i_{\ell 2}$ becomes

$$\frac{di_{a\ell 2}}{dt} = \frac{E_1}{L} \sin(\omega t + \beta) - \frac{R_\ell}{L} i_{\ell 2} - \frac{L_\ell}{L} \frac{di_{\ell 2}}{dt} - CR_\ell \frac{d^2 i_{\ell 2}}{dt^2} - L_\ell C \frac{d^3 i_{\ell 2}}{dt^3} \tag{2.3.52}$$

For purely resistive loads, the above equation becomes

$$\frac{di_{a\ell 2}}{dt} = \frac{E_1}{L} \sin(\omega t + \beta) - \frac{R_\ell}{L} i_{\ell 2} - CR_\ell \frac{d^2 i_{\ell 2}}{dt^2} \tag{2.3.53}$$

Integrating (2.3.53) from $(\gamma/\omega)^+$ to t yields

$$\begin{aligned} i_{a\ell 2}(t) = {} & \frac{E_1}{\omega L} [\cos(\gamma + \beta) - \cos(\omega t + \beta)] - k_5 R_\ell \left(\frac{1}{Lr_3} + Cr_3\right)\left(e^{r_3 t} - e^{\frac{\gamma r_3}{\omega}}\right) \\ & - k_6 R_\ell \left(\frac{1}{Lr_4} + Cr_4\right)\left(e^{r_4 t} - e^{\frac{\gamma r_4}{\omega}}\right) + \frac{2E_1}{K_1} R_\ell \left(\frac{1}{\omega L} - \omega C\right) \cdot \\ & [\cos(\omega t + \beta - \alpha_1 + \tfrac{\pi}{3}) - \cos(\gamma + \beta - \alpha_1 + \tfrac{\pi}{3})] + I_{a\ell 2} \end{aligned} \tag{2.3.54}$$

Circuit conditions at $t = (\frac{\pi}{3\omega})$ yields

$$i_{ac2}(\tfrac{\pi}{3\omega})^- + i_{a\ell 2}(\tfrac{\pi}{3\omega})^- = i_{ac3}(\tfrac{\pi}{3\omega})^+ + i_{a\ell 3}(\tfrac{\pi}{3\omega})^+ \tag{2.3.55}$$

Applying (2.3.13) to above and rearranging, the expression of $i_{a\ell 3}$ for purely resistive loads becomes

$$i_{a\ell 3}(\tfrac{\pi}{3\omega})^+ = i_{a\ell 2}(\tfrac{\pi}{3\omega})^- - CR_\ell \left[\frac{di_{\ell 3}}{dt}(\tfrac{\pi}{3\omega})^+ - \frac{di_{\ell 2}}{dt}(\tfrac{\pi}{3\omega})^- \right] \tag{2.3.56}$$

Again, define

$$I_{a\ell 3} \equiv i_{a\ell 3}(\tfrac{\pi}{3\omega})^+ \tag{2.3.57}$$

Differentiate (2.3.31) and (2.3.35) once, then, evaluate the results as well as $i_{a\ell 2}$ from (2.3.54) at $t = (\frac{\pi}{3\omega})$. Using these results in (2.3.56), phase-a bridge-input current at the beginning of interval 3 is obtained as given below.

$$I_{a\ell 3} = \frac{E_1}{\omega L}[\cos(\gamma + \beta) - \cos(\beta + \tfrac{\pi}{3})] - k_5 R_\ell (\frac{1}{Lr_3} + Cr_3)(e^{\frac{\pi r_3}{3\omega}} - e^{\frac{\gamma r_3}{\omega}})$$
$$- k_6 R_\ell(\frac{1}{Lr_4} + Cr_4)(e^{\frac{\pi r_4}{3\omega}} - e^{\frac{\gamma r_4}{\omega}}) + \frac{2E_1}{K_1} R_\ell(\frac{1}{\omega L} - \omega C)[\cos(\beta - \alpha_1 + \tfrac{2\pi}{3})$$
$$- \cos(\gamma + \beta - \alpha_1 + \tfrac{\pi}{3})] + I_{a\ell 2} - CR_\ell [k_1 r_1 + k_2 r_2 + \frac{\sqrt{3}E_1}{K_2}\omega \cdot$$
$$\cos(\beta - \alpha_2 + \tfrac{\pi}{2}) - k_5 r_3 e^{\frac{\pi r_3}{3\omega}} - k_6 r_4 e^{\frac{\pi r_4}{3\omega}} - \frac{2E_1}{K_1}\omega \cos(\beta - \alpha_1 + \tfrac{2\pi}{3})] \quad (2.3.58)$$

By a procedure similar to the one used in obtaining (2.3.52), the first derivative of bridge-input current during interval 3 is

$$\frac{di_{a\ell 3}}{dt} = \frac{E_1}{L}\sin(\omega t + \beta) - \frac{R_\ell}{L} i_{\ell 3} - \frac{L_\ell}{L}\frac{di_{\ell 3}}{dt} - CR_\ell \frac{d^2 i_{\ell 3}}{dt^2} - L_\ell C \frac{d^3 i_{\ell 3}}{dt^3} \quad (2.3.59)$$

For purely resistive loads, $L_\ell = 0$, and the above becomes:

$$\frac{di_{a\ell 3}}{dt} = \frac{E_1}{L}\sin(\omega t + \beta) - \frac{R_\ell}{L} i_{\ell 3} - CR_\ell \frac{d^2 i_{\ell 3}}{dt^2} \quad (2.3.60)$$

Integrating (2.3.60) from $(\frac{\pi}{3\omega})^+$ to t yields

$$i_{a\ell 3}(t) = \frac{E_1}{\omega L}[\cos(\beta + \tfrac{\pi}{3}) - \cos(\omega t + \beta)] - k_1 R_\ell(\frac{1}{Lr_1} + Cr_1)[e^{r_1(t - \frac{\pi}{3\omega})} - 1]$$
$$- k_2 R_\ell (\frac{1}{Lr_2} + Cr_2)[e^{r_2(t - \frac{\pi}{3\omega})} - 1] + \frac{\sqrt{3}E_1}{K_2} R_\ell (\frac{1}{\omega L} - \omega C)\cdot$$
$$[\cos(\omega t + \beta - \alpha_2 + \tfrac{\pi}{6}) - \cos(\beta - \alpha_2 + \tfrac{\pi}{2})] + I_{a\ell 3} \quad (2.3.61)$$

Repeating similar procedures, initial and instantaneous values of bridge-input currents during intervals 4, 5 and 6 are derived and the

results are given below.

$$I_{a\ell 4} = \frac{E_1}{\omega L}[\cos(\beta + \tfrac{\pi}{3}) - \cos(\gamma + \beta + \tfrac{\pi}{3})] - k_1 R_\ell (\frac{1}{Lr_1} + Cr_1)(e^{\frac{\gamma r_1}{\omega}} - 1)$$
$$- k_2 R_\ell (\frac{1}{Lr_2} + Cr_2)(e^{\frac{\gamma r_2}{\omega}} - 1) + \frac{\sqrt{3}E_1}{K_2} R_\ell (\frac{1}{\omega L} - \omega C) \cdot$$
$$[\cos(\gamma + \beta - \alpha_2 + \tfrac{\pi}{2}) - \cos(\beta - \alpha_2 + \tfrac{\pi}{2})] + I_{a\ell 3}$$
$$- CR_\ell\{k_5 r_3 e^{\frac{\gamma r_3}{\omega}} + k_6 r_4 e^{\frac{\gamma r_4}{\omega}} + \frac{2E_1}{K_1}\omega \cos(\gamma + \beta - \alpha_1 + \tfrac{\pi}{3})$$
$$- [k_1 r_1 e^{\frac{\gamma r_1}{\omega}} + k_2 r_2 e^{\frac{\gamma r_2}{\omega}} + \frac{\sqrt{3}E_1}{K_2}\omega \cos(\gamma + \beta - \alpha_2 + \tfrac{\pi}{2})]\} \qquad (2.3.62)$$

$$i_{a\ell 4}(t) = \frac{E_1}{\omega L}[\cos(\gamma + \beta + \tfrac{\pi}{3}) - \cos(\omega t + \beta)] - k_5 R_\ell (\frac{1}{Lr_3} + Cr_3) \cdot$$
$$[e^{r_3(t - \frac{\pi}{3\omega})} - e^{\frac{\gamma r_3}{\omega}}] - k_6 R_\ell (\frac{1}{Lr_4} + Cr_4)[e^{r_4(t - \frac{\pi}{3\omega})} - e^{\frac{\gamma r_4}{\omega}}]$$
$$+ \frac{2E_1}{K_1} R_\ell (\frac{1}{\omega L} - \omega C)[\cos(\omega t + \beta - \alpha_1) - \cos(\gamma + \beta - \alpha_1 + \tfrac{\pi}{3})]$$
$$+ I_{a\ell 4} \qquad (2.3.63)$$

$$I_{a\ell 5} = \frac{E_1}{\omega L}[\cos(\gamma + \beta + \tfrac{\pi}{3}) - \cos(\beta + \tfrac{2\pi}{3})] - k_5 R_\ell (\frac{1}{Lr_3} + Cr_3) \cdot$$
$$(e^{\frac{\pi r_3}{3\omega}} - e^{\frac{\gamma r_3}{\omega}}) - k_6 R_\ell (\frac{1}{Lr_4} + Cr_4)(e^{\frac{\pi r_4}{3\omega}} - e^{\frac{\gamma r_4}{\omega}}) + \frac{2E_1}{K_1} R_\ell \cdot$$
$$(\frac{1}{\omega L} - \omega C)[\cos(\beta - \alpha_1 + \tfrac{2\pi}{3}) - \cos(\gamma + \beta - \alpha_1 + \tfrac{\pi}{3})] + I_{a\ell 4}$$
$$- CR_\ell\{k_1 r_1 + k_2 r_2 + \frac{\sqrt{3}E_1}{K_2}\omega \cos(\beta - \alpha_2 + \tfrac{\pi}{2})$$
$$- [k_5 r_3 e^{\frac{\pi r_3}{3\omega}} + k_6 r_4 e^{\frac{\pi r_4}{3\omega}} + \frac{2E_1}{K_1}\omega \cos(\beta - \alpha_1 + \tfrac{2\pi}{3})]\} \qquad (2.3.64)$$

$$i_{a\ell 5}(t) = \frac{E_1}{\omega L}\left[\cos\left(\beta + \frac{2\pi}{3}\right) - \cos(\omega t + \beta)\right] - k_1 R_\ell \left(\frac{1}{Lr_1} + Cr_1\right)\cdot$$
$$\left[e^{r_1\left(t - \frac{2\pi}{3\omega}\right)} - 1\right] - k_2 R_\ell \left(\frac{1}{Lr_2} + Cr_2\right)\left[e^{r_2\left(t - \frac{2\pi}{3\omega}\right)} - 1\right]$$
$$+ \frac{\sqrt{3}E_1}{K_2} R_\ell \left(\frac{1}{\omega L} - \omega C\right)\left[\cos\left(\omega t + \beta - \alpha_2 - \frac{\pi}{6}\right) - \cos\left(\beta - \alpha_2 + \frac{\pi}{2}\right)\right]$$
$$+ I_{a\ell 5} \qquad (2.3.65)$$

$$I_{a\ell 6} = \frac{E_1}{\omega L}\left[\cos\left(\beta + \frac{2\pi}{3}\right) - \cos\left(\gamma + \beta + \frac{2\pi}{3}\right)\right] - k_1 R_\ell \left(\frac{1}{Lr_1} + Cr_1\right)\left(e^{\frac{\gamma r_1}{\omega}} - 1\right)$$
$$- k_2 R_\ell \left(\frac{1}{Lr_2} + Cr_2\right)\left(e^{\frac{\gamma r_2}{\omega}} - 1\right) + \frac{\sqrt{3}E_1}{K_2} R_\ell \left(\frac{1}{\omega L} - \omega C\right)\cdot$$
$$\left[\cos\left(\gamma + \beta - \alpha_2 + \frac{\pi}{2}\right) - \cos\left(\beta - \alpha_2 + \frac{\pi}{2}\right)\right] + I_{a\ell 5}$$
$$- C R_\ell \left\{k_5 r_3 e^{\frac{\gamma r_3}{\omega}} + k_6 r_4 e^{\frac{\gamma r_4}{\omega}} + \frac{2E_1}{K_1}\omega \cos\left(\gamma + \beta - \alpha_1 + \frac{\pi}{3}\right)\right.$$
$$\left. - \left[k_1 r_1 e^{\frac{\gamma r_1}{\omega}} + k_2 r_2 e^{\frac{\gamma r_2}{\omega}} + \frac{\sqrt{3}E_1}{K_2}\omega \cos\left(\gamma + \beta - \alpha_2 + \frac{\pi}{2}\right)\right]\right\} \qquad (2.3.66)$$

$$i_{a\ell 6}(t) = \frac{E_1}{\omega L}\left[\cos\left(\gamma + \beta + \frac{2\pi}{3}\right) - \cos(\omega t + \beta)\right] - k_5 R_\ell \left(\frac{1}{Lr_3} + Cr_3\right)\cdot$$
$$\left[e^{r_3\left(t - \frac{2\pi}{\omega}\right)} - e^{\frac{\gamma r_3}{\omega}}\right] - k_6 R_\ell \left(\frac{1}{Lr_4} + Cr_4\right)\left[e^{r_4\left(t - \frac{2\pi}{3\omega}\right)} - e^{\frac{\gamma r_4}{\omega}}\right]$$
$$+ \frac{2E_1}{K_1} R_\ell \left(\frac{1}{\omega L} - \omega C\right)\left[\cos\left(\omega t + \beta - \alpha_1 - \frac{\pi}{3}\right) - \cos\left(\gamma + \beta - \alpha_1 + \frac{\pi}{3}\right)\right]$$
$$+ I_{a\ell 6} \qquad (2.3.67)$$

(D) Derivation of Phase-a Source Current

From (2.3.4) and (2.3.13), the source current during interval 2 can be expressed as

$$i_{a2}(t) = i_{a\ell 2} + C \frac{dv_{a2}}{dt} \tag{2.3.68}$$

For $t \geq (\gamma/\omega)^+$, $i_{a\ell} \neq 0$; with ideal diodes, the following relationship must hold during interval 2.

$$v_{a2} = v_{\ell 2} = R_\ell \, i_{\ell 2} + L_\ell \frac{di_{\ell 2}}{dt} \tag{2.3.69}$$

Substituting (2.3.69) in (2.3.68),

$$i_{a2}(t) = i_{a\ell 2} + C \, R_\ell \frac{di_{\ell 2}}{dt} + L_\ell \, C \frac{d^2 i_{\ell 2}}{dt^2} \tag{2.3.70}$$

With $L_\ell = 0$, the above becomes

$$i_{a2}(t) = i_{a\ell 2} + C \, R_\ell \frac{di_{\ell 2}}{dt} \tag{2.3.71}$$

Differentiate both sides of (2.3.31) and obtain

$$\frac{di_{\ell 2}}{dt} = k_5 \, r_3 \, e^{r_3 t} + k_6 \, r_4 \, e^{r_4 t} + \frac{2E_1}{K_1} \omega \cos(\omega t + \beta - \alpha_1 + \tfrac{\pi}{3}) \tag{2.3.72}$$

Substituting (2.3.54) and (2.3.72) into (2.3.71), and rearranging, the following expression results.

$$\begin{aligned} i_{a2}(t) = {} & \frac{E_1}{\omega L} [\cos(\gamma + \beta) - \cos(\omega t + \beta)] + \frac{2E_1}{K_1} R_\ell \{\frac{1}{\omega L} [\cos(\omega t + \beta - \alpha_1 + \tfrac{\pi}{3}) \\ & - \cos(\gamma + \beta - \alpha_1 + \tfrac{\pi}{3})] + \omega C \cos(\gamma + \beta - \alpha_1 + \tfrac{\pi}{3})\} \\ & + k_5 \, R_\ell \, [(\frac{1}{Lr_3} + Cr_3) \, e^{\frac{\gamma r_3}{\omega}} - \frac{1}{Lr_3} e^{r_3 t}] \\ & + k_6 \, R_\ell \, [(\frac{1}{Lr_4} + Cr_4) \, e^{\frac{\gamma r_4}{\omega}} - \frac{1}{Lr_4} e^{r_4 t}] + I_{a\ell 2} \end{aligned} \tag{2.3.73}$$

By repeating the process demonstrated above, source currents during intervals 3 through 6 can be derived. The results are given below.

$$i_{a3}(t) = \frac{E_1}{\omega L}\left[\cos\left(\beta + \frac{\pi}{3}\right) - \cos(\omega t + \beta)\right] + \frac{\sqrt{3}E_1}{K_2} R_\ell \left\{\frac{1}{\omega L} \cdot \right.$$

$$\left[\cos\left(\omega t + \beta - \alpha_2 + \frac{\pi}{6}\right) - \cos\left(\beta - \alpha_2 + \frac{\pi}{2}\right)\right] + \omega C \cos\left(\beta - \alpha_2 + \frac{\pi}{2}\right)\Big\}$$

$$+ k_1 R_\ell \left[\left(\frac{1}{Lr_1} + Cr_1\right) - \frac{1}{Lr_1} e^{r_1\left(t - \frac{\pi}{3\omega}\right)}\right]$$

$$+ k_2 R_\ell \left[\left(\frac{1}{Lr_2} + Cr_2\right) - \frac{1}{Lr_2} e^{r_2\left(t - \frac{\pi}{3\omega}\right)}\right] + I_{a\ell 3} \qquad (2.3.74)$$

$$i_{a4}(t) = \frac{E_1}{\omega L}\left[\cos\left(\gamma + \beta + \frac{\pi}{3}\right) - \cos(\omega t + \beta)\right] + \frac{2E_1}{K_1} R_\ell \left\{\frac{1}{\omega L} \cdot \right.$$

$$\left[\cos(\omega t + \beta - \alpha_1) - \cos\left(\gamma + \beta - \alpha_1 + \frac{\pi}{3}\right)\right]$$

$$+ \omega C \cos\left(\gamma + \beta - \alpha_1 + \frac{\pi}{3}\right)\Big\}$$

$$+ k_5 R_\ell \left[\left(\frac{1}{Lr_3} + Cr_3\right) e^{\frac{\gamma r_3}{\omega}} - \frac{1}{Lr_3} e^{r_3\left(t - \frac{\pi}{3\omega}\right)}\right]$$

$$+ k_6 R_\ell \left[\left(\frac{1}{Lr_4} + Cr_4\right) e^{\frac{\gamma r_4}{\omega}} - \frac{1}{Lr_4} e^{r_4\left(t - \frac{\pi}{3\omega}\right)}\right] + I_{a\ell 4} \qquad (2.3.75)$$

$$i_{a5}(t) = \frac{E_1}{\omega L}\left[\cos\left(\beta + \frac{2\pi}{3}\right) - \cos(\omega t + \beta)\right] + \frac{\sqrt{3}E_1}{K_2} R_\ell \left\{\frac{1}{\omega L} \cdot \right.$$

$$\left[\cos\left(\omega t + \beta - \alpha_2 - \frac{\pi}{6}\right) - \cos\left(\beta - \alpha_2 + \frac{\pi}{2}\right)\right] + \omega C \cos\left(\beta - \alpha_2 + \frac{\pi}{2}\right)\Big\}$$

$$+ k_1 R_\ell \left[\left(\frac{1}{Lr_1} + Cr_1\right) - \frac{1}{Lr_1} e^{r_1\left(t - \frac{2\pi}{3\omega}\right)}\right]$$

$$+ k_2 R_\ell \left[\left(\frac{1}{Lr_2} + Cr_2\right) - \frac{1}{Lr_2} e^{r_2\left(t - \frac{2\pi}{3\omega}\right)}\right] + I_{a\ell 5} \qquad (2.3.76)$$

$$i_{a6}(t) = \frac{E_1}{\omega L}[\cos(\gamma + \beta + \tfrac{2\pi}{3}) - \cos(\omega t + \beta)] + \frac{2E_1}{K_1} R_\ell \{\frac{1}{\omega L} \cdot$$

$$[\cos(\omega t + \beta - \alpha_1 - \tfrac{\pi}{3}) - \cos(\gamma + \beta - \alpha_1 + \tfrac{\pi}{3})]$$

$$+ \omega C \cos(\gamma + \beta - \alpha_1 + \tfrac{\pi}{3})\}$$

$$+ k_5 R_\ell [(\frac{1}{Lr_3} + Cr_3) e^{\frac{\gamma r_3}{\omega}} - \frac{1}{Lr_3} e^{r_3(t - \frac{2\pi}{3\omega})}]$$

$$+ k_6 R_\ell [(\frac{1}{Lr_4} + Cr_4) e^{\frac{\gamma r_4}{\omega}} - \frac{1}{Lr_4} e^{r_4(t - \frac{2\pi}{3\omega})}] + I_{a\ell 6} \qquad (2.3.77)$$

(E) Derivation of v_a and i_{ac}

From the circuit configuration,

$$v_{an} = e_a - L \frac{di_{an}}{dt} \qquad \text{for } n = 1, 2, \ldots, 6 \qquad (2.3.78)$$

and

$$i_{acn} = C \frac{dv_{an}}{dt} \qquad \text{for } n = 1, 2, \ldots, 6 \qquad (2.3.79)$$

(F) Derivation of V_o and I_o

At the instant $t = 0^+$, the initial bridge-input capacitor voltage is defined from symmetry as

$$V_o \equiv -v_{a1}(0)^+ = R_\ell \, i_{\ell 2}(\tfrac{\pi}{3\omega})^- + L_\ell \left.\frac{di_{\ell 2}}{dt}\right|_{t = (\frac{\pi}{3\omega})^-} \qquad (2.3.80)$$

Evaluating (2.3.31) for $t = \frac{\pi}{3\omega}$ and substituting into above with $L_\ell = 0$ results

$$V_o = R_\ell [k_5 e^{\frac{\pi r_3}{3\omega}} + k_6 e^{\frac{\pi r_4}{3\omega}} + \frac{2E_1}{K_1} \sin(\beta - \alpha_1 + \tfrac{2\pi}{3})] \qquad (2.3.81)$$

Similarly, at $t = 0^+$, the initial inductor current is equal to $i_{a1}(0)^-$ or $-i_{a6}(\pi/\omega)^-$. Therefore,

$$i_{a1}(0)^+ = i_{a1}(0)^- = -i_{a6}(\pi/\omega)^- \tag{2.3.82}$$

For simplicity, let

$$I_o = -i_{a6}(\pi/\omega)^- \tag{2.3.83}$$

Using (2.3.13) in (2.3.4) yields

$$i_{a6}(\tfrac{\pi}{\omega})^- = i_{a\ell 6}(\tfrac{\pi}{\omega})^- + C \left.\frac{dv_{\ell 6}}{dt}\right|_{t = (\frac{\pi}{\omega})^-} \tag{2.3.84}$$

But

$$v_{\ell 6} = R_\ell\, i_{\ell 6} + L_\ell \frac{di_{\ell 6}}{dt} \tag{2.3.85}$$

Substituting (2.3.85) into (2.3.84),

$$i_{a6}(\tfrac{\pi}{\omega})^- = i_{a\ell 6}(\tfrac{\pi}{\omega})^- + C\, R_\ell \left.\frac{di_{\ell 6}}{dt}\right|_{t = (\frac{\pi}{\omega})^-} + L_\ell\, C \left.\frac{d^2 i_{\ell 6}}{dt^2}\right|_{t = (\frac{\pi}{\omega})^-} \tag{2.3.86}$$

With $L_\ell = 0$, $i_{a\ell 6}(\pi/\omega)^- = 0$ and

$$i_{a6}(\tfrac{\pi}{\omega})^- = C\, R_\ell \left.\frac{di_{\ell 6}}{dt}\right|_{t = (\frac{\pi}{\omega})^-} \tag{2.3.87}$$

Differentiate (2.3.38) and substitute in (2.3.87). Then from (2.3.82) and (2.3.83),

$$I_o = -C\, R_\ell \left[k_5\, r_3\, e^{\frac{\pi r_3}{3\omega}} + k_6\, r_4\, e^{\frac{\pi r_4}{3\omega}} + \frac{2E_1}{K_1}\,\omega \cos(\beta - \alpha_1 + \tfrac{2\pi}{3})\right] \tag{2.3.88}$$

(G) Evaluation of Constants

The next step in the analysis is to evaluate the four constants k_1, k_2, k_5, k_6 and the two angles γ and β for specified circuit parameters L, E_1, f, C and R_ℓ. Six equations are necessary for computing these values and they are found by applying the following boundary conditions.

$$f_1 \equiv v_{a1}(\gamma/\omega)^- - i_{\ell 2}(\gamma/\omega)^+ R_\ell = 0 \tag{2.3.89}$$

$$f_2 \equiv [I_{a\ell 3} + I_{a\ell 5}] - i_{\ell 1}(0)^+ = 0 \tag{2.3.90}$$

$$f_3 \equiv i_{\ell 1}(0)^+ - i_{\ell 2}(\tfrac{\pi}{3\omega})^- = 0 \tag{2.3.91}$$

$$f_4 \equiv i_{\ell 1}(\gamma/\omega)^- - i_{\ell 2}(\gamma/\omega)^+ = 0 \tag{2.3.92}$$

$$f_5 \equiv [I_{a\ell 3} + I_{a\ell 5}] - [i_{a\ell 2}(\tfrac{\pi}{3\omega})^- + i_{a\ell 4}(\tfrac{2\pi}{3\omega})^-] = 0 \tag{2.3.93}$$

$$f_6 \equiv [i_{a\ell 3}(\tfrac{\pi}{3\omega} + \tfrac{\gamma}{\omega})^- + i_{a\ell 5}(\tfrac{2\pi}{3\omega} + \tfrac{\gamma}{\omega})^-] - [I_{a\ell 2} + I_{a\ell 4} + I_{a\ell 6}] = 0 \tag{2.3.94}$$

By the proper application of relevant equations into (2.3.89) through (2.3.94) and rearranging, complete expressions for f_1 through f_6 are obtained as given below.

$$f_1 = \frac{E_1}{1-\omega^2 LC}\sin(\gamma + \beta) + \sqrt{\frac{L}{C}}\left(I_o - \frac{E_1}{1-\omega^2 LC}\omega C\cos\beta\right)\sin(\tfrac{\gamma}{\omega\sqrt{LC}})$$

$$- \left(V_o + \frac{E_1}{1-\omega^2 LC}\sin\beta\right)\cos(\tfrac{\gamma}{\omega\sqrt{LC}})$$

$$- [k_5 e^{\frac{\gamma r_3}{\omega}} + k_6 e^{\frac{\gamma r_4}{\omega}} + \frac{2E_1}{K_1}\sin(\gamma + \beta - \alpha_1 + \tfrac{\pi}{3})]\, R_\ell = 0 \tag{2.3.95}$$

$$f_2 = \frac{E_1}{\omega L}[2\cos(\gamma+\beta) + \sqrt{3}\sin\beta] - k_1 R_\ell \left(\frac{1}{Lr_1} + Cr_1\right)\left(e^{\frac{\gamma r_1}{\omega}} - 1\right)$$

$$- k_2 R_\ell \left(\frac{1}{Lr_2} + Cr_2\right)\left(e^{\frac{\gamma r_2}{\omega}} - 1\right) - 3k_5 R_\ell \left(\frac{1}{Lr_3} + Cr_3\right)\left(e^{\frac{\pi r_3}{3\omega}} - e^{\frac{\gamma r_3}{\omega}}\right)$$

$$- 3k_6 R_\ell \left(\frac{1}{Lr_4} + Cr_4\right)\left(e^{\frac{\pi r_4}{3\omega}} - e^{\frac{\gamma r_4}{\omega}}\right)$$

$$+ \frac{6E_1}{K_1} R_\ell \left(\frac{1}{\omega L} - \omega C\right)\left[\cos\left(\beta - \alpha_1 + \frac{2\pi}{3}\right) - \cos\left(\gamma + \beta - \alpha_1 + \frac{\pi}{3}\right)\right]$$

$$+ \frac{\sqrt{3}E_1}{K_2} R_\ell \left(\frac{1}{\omega L} - \omega C\right)\left[\cos\left(\gamma + \beta - \alpha_2 + \frac{\pi}{2}\right) - \cos\left(\beta - \alpha_2 + \frac{\pi}{2}\right)\right]$$

$$- 3C R_\ell \left\{k_1 r_1 + k_2 r_2 + \frac{\sqrt{3}E_1}{K_2}\omega\cos\left(\beta - \alpha_2 + \frac{\pi}{2}\right)\right.$$

$$\left. - \left[k_5 r_3 e^{\frac{\pi r_3}{3\omega}} + k_6 r_4 e^{\frac{\pi r_4}{3\omega}} + \frac{2E_1}{K_1}\omega\cos\left(\beta - \alpha_1 + \frac{2\pi}{3}\right)\right]\right\}$$

$$- C R_\ell \left\{k_5 r_3 e^{\frac{\gamma r_3}{\omega}} + k_6 r_4 e^{\frac{\gamma r_4}{\omega}} + \frac{2E_1}{K_1}\omega\cos\left(\gamma + \beta - \alpha_1 + \frac{\pi}{3}\right)\right.$$

$$\left. - \left[k_1 r_1 e^{\frac{\gamma r_1}{\omega}} + k_2 r_2 e^{\frac{\gamma r_2}{\omega}} + \frac{\sqrt{3}E_1}{K_2}\omega\cos\left(\gamma + \beta - \alpha_2 + \frac{\pi}{2}\right)\right]\right\}$$

$$+ 2I_{a\ell 2} - \left[k_1 + k_2 + \frac{\sqrt{3}E_1}{K_2}\sin\left(\beta - \alpha_2 + \frac{\pi}{2}\right)\right] = 0 \qquad (2.3.96)$$

$$f_3 = k_1 + k_2 + \frac{\sqrt{3}E_1}{K_2}\sin\left(\beta - \alpha_2 + \frac{\pi}{2}\right)$$

$$- \left[k_5 e^{\frac{\pi r_3}{3\omega}} + k_6 e^{\frac{\pi r_4}{3\omega}} + \frac{2E_1}{K_1}\sin\left(\beta - \alpha_1 + \frac{2\pi}{3}\right)\right] = 0 \qquad (2.3.97)$$

$$f_4 = k_1 e^{\frac{\gamma r_1}{\omega}} + k_2 e^{\frac{\gamma r_2}{\omega}} + \frac{\sqrt{3}E_1}{K_2} \sin(\gamma + \beta - \alpha_2 + \frac{\pi}{2})$$

$$- [k_5 e^{\frac{\gamma r_3}{\omega}} + k_6 e^{\frac{\gamma r_4}{\omega}} + \frac{2E_1}{K_1} \sin(\gamma + \beta - \alpha_1 + \frac{\pi}{3})] = 0 \qquad (2.3.98)$$

$$f_5 = k_1 r_1 + k_2 r_2 + \frac{\sqrt{3}E_1}{K_2} \omega \cos(\beta - \alpha_2 + \frac{\pi}{2})$$

$$- [k_5 r_3 e^{\frac{\pi r_3}{3\omega}} + k_6 r_4 e^{\frac{\pi r_4}{3\omega}} + \frac{2E_1}{K_1} \omega \cos(\beta - \alpha_1 + \frac{2\pi}{3})] = 0 \qquad (2.3.99)$$

$$f_6 = I_{a\ell 2} - 2C R_\ell \{k_5 r_3 e^{\frac{\gamma r_3}{\omega}} + k_6 r_4 e^{\frac{\gamma r_4}{\omega}} + \frac{2E_1}{K_1} \omega \cos(\gamma + \beta - \alpha_1 + \frac{\pi}{3})$$

$$- [k_1 r_1 e^{\frac{\gamma r_1}{\omega}} + k_2 r_2 e^{\frac{\gamma r_2}{\omega}} + \frac{\sqrt{3}E_1}{K_2} \omega \cos(\gamma + \beta - \alpha_2 + \frac{\pi}{2})]\} = 0$$

(2.3.100)

To increase computational accuracy, evaluation of the six constants was made by following the steps listed below.

1. Make an initial guess for γ_i and β_i and substitute them into (2.3.97) through (2.3.100) to form four linear simultaneous equations.
2. Solve these linear simultaneous equations for k_1, k_2, k_5 and k_6.
3. Substitute the values obtained in (2.3.95) and (2.3.96) to form two nonlinear equations in γ and β.
4. Solve the two nonlinear equations to obtain improved values γ_{i+1} and β_{i+1}.
5. Using the result of step 4, repeat steps 1 through 4 until

specified convergence criteria are met.

Marquardt's method [25] was used to compute the six constants. An IBM 360 digital computer was employed in this process.

Calculated results are presented in Figure 8 as a family of curves showing the values of γ and β for different values of the ratios (X_L/X_C) and (X_L/X_ℓ) in the region $\infty > \frac{X_L X_C}{R_\ell^2} > 36$. This region includes the primary range of interest for different parameter ratios. Obviously, the ratio (X_L/X_C) approaching zero corresponds to the case C = 0. Under these circumstances, $\gamma = 0$ and the angles β should be equal to $\tan^{-1}(\frac{X_L}{3R_\ell})$, a relationship derived by Ramakumar, et al., (reference 21). Calculated K_1, k_2, k_5 and k_6 are presented in Figure 9 through 12.

2.4 Harmonic Analysis of Resulting Waveforms

In this Section, PBRS waveforms of interest for FMGS modeling and output filter design are analyzed and their harmonic components are computed. The waveforms of interest are i_a, i_ℓ and v_a, and expressions for these have been derived in Section 2.3 of this Chapter.

Fourier series expansions for i_a, i_ℓ and v_a are given below.

$$i_a(t) = \sum_{n=1,3,5,\ldots}^{\infty} K\,(a_{an} \cos n\omega t + b_{an} \sin n\omega t) \qquad (2.4.1)$$

$$= \sum_{n=1,3,5,\ldots}^{\infty} K\,K_{an} \sin(n\omega t - \phi_{an}) \qquad (2.4.2)$$

where

$$K_{an} = \sqrt{a_{an}^2 + b_{an}^2} \qquad (2.4.3)$$

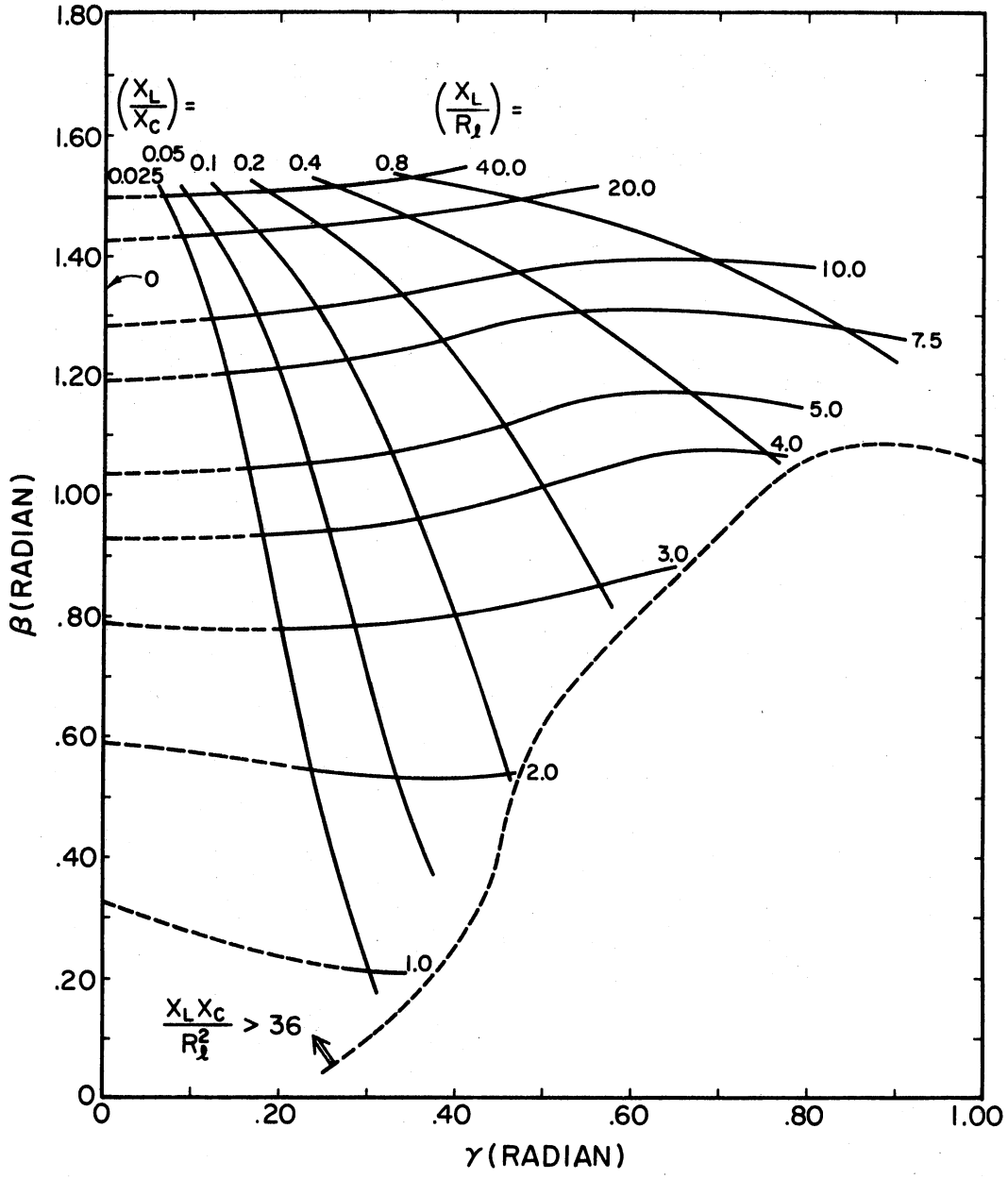

Figure 8. Theoretical Values of γ and β

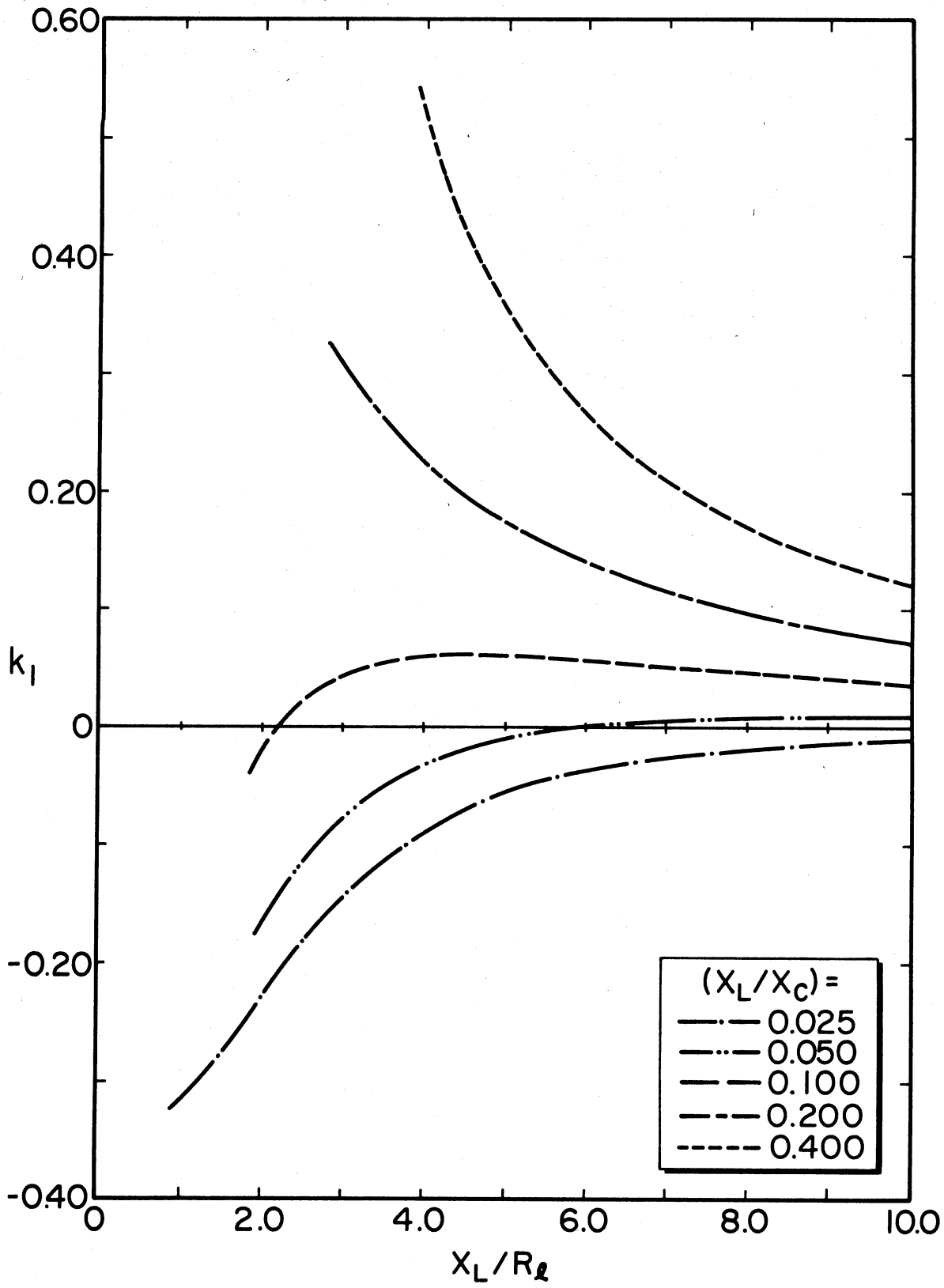

Figure 9. Theoretical Values of k_1

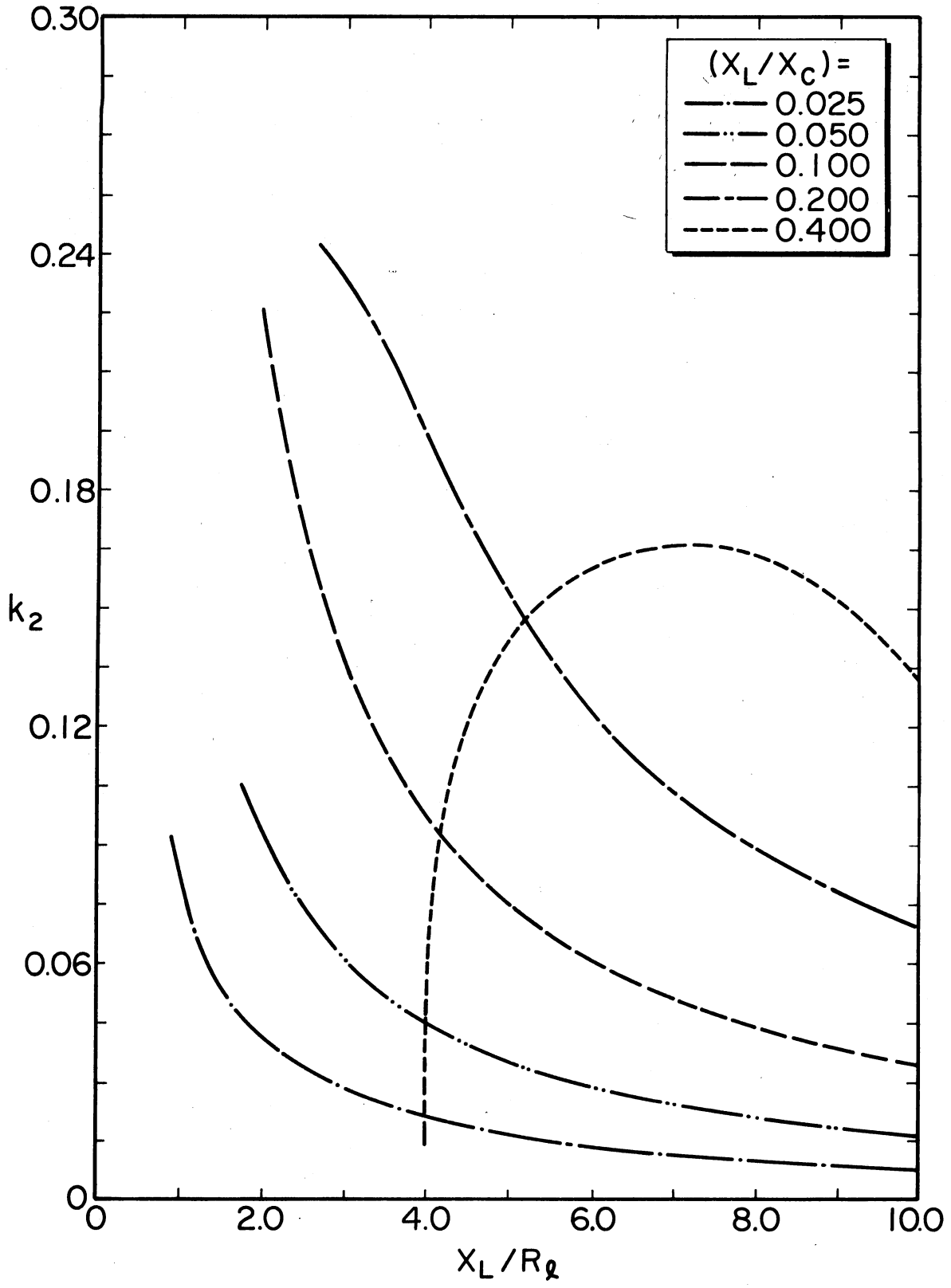

Figure 10. Theoretical Values of k_2

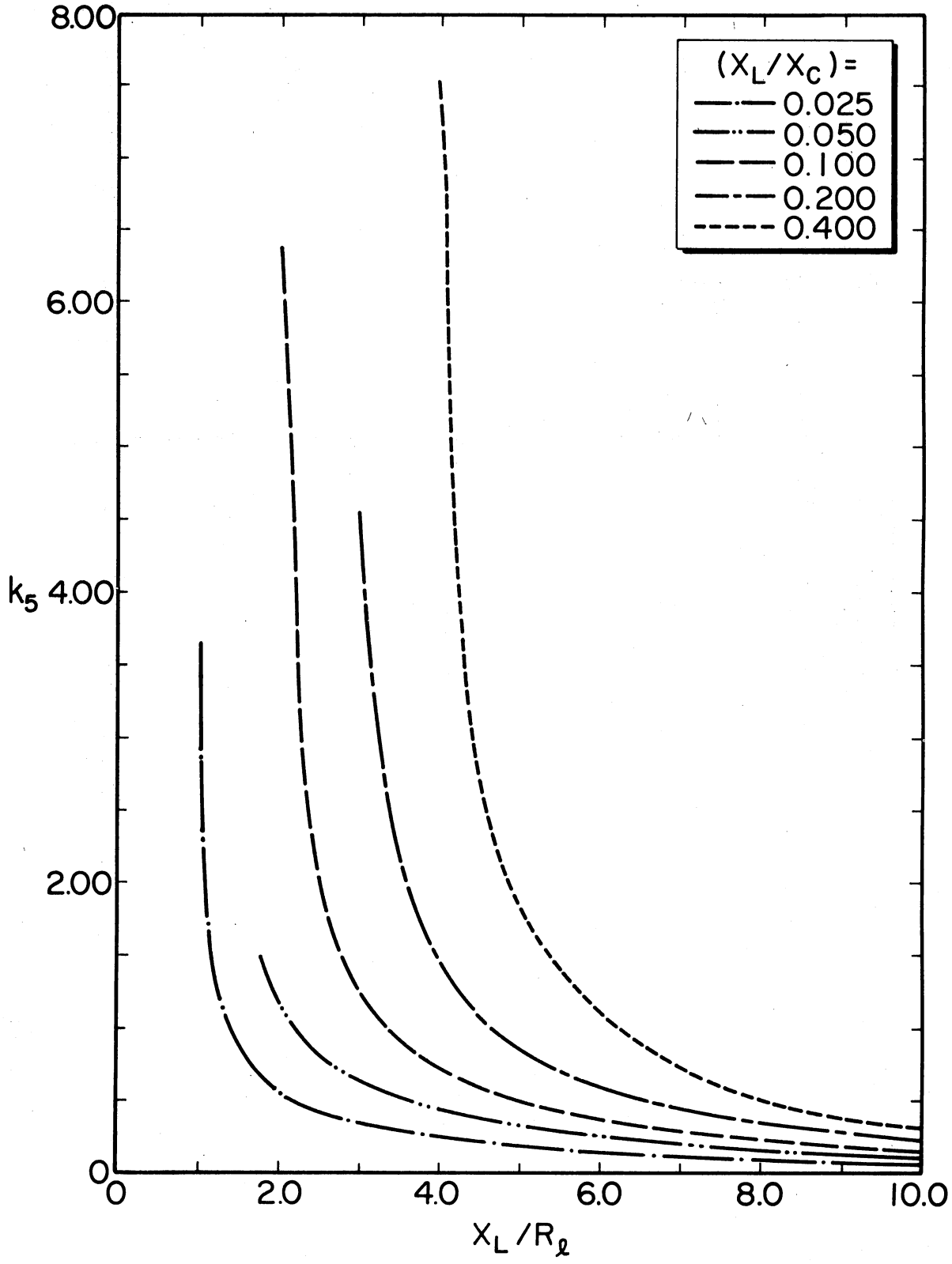

Figure 11. Theoretical Values of k_5

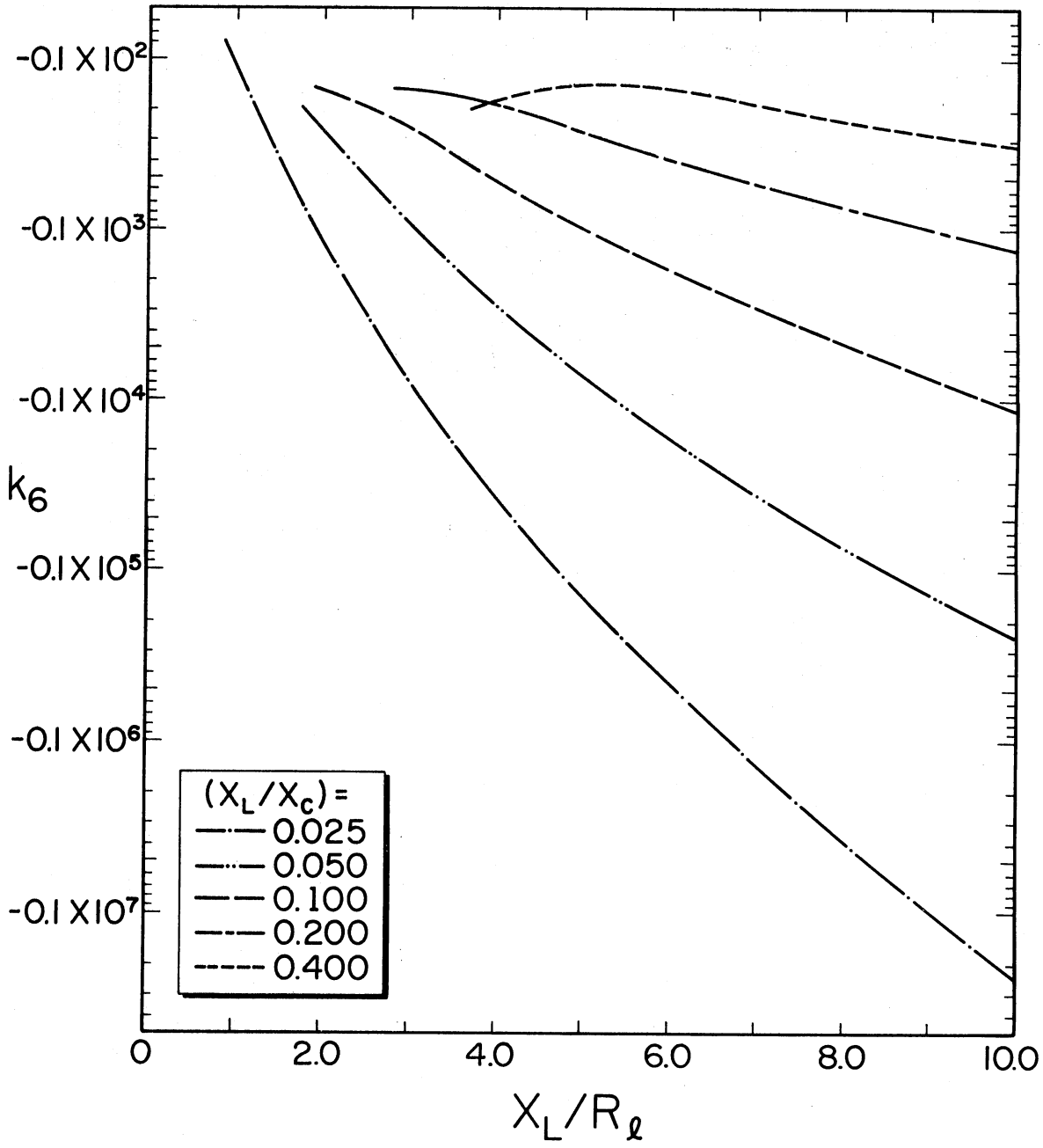

Figure 12. Theoretical Values of k_6

$$\phi_{an} = -\tan^{-1} \frac{a_{an}}{b_{an}} \tag{2.4.4}$$

$$K = \frac{E_1}{\omega L} \tag{2.4.5}$$

$$i_\ell(t) = K K_{\ell o} + \sum_{n=6,12,18,\ldots}^{\infty} K (a_{\ell n} \cos n\omega t + b_{\ell n} \sin n\omega t) \tag{2.4.6}$$

$$= K K_{\ell o} + \sum_{n=6,12,18,\ldots}^{\infty} K K_{\ell n} \sin(n\omega t - \phi_{\ell n}) \tag{2.4.7}$$

where

$$K_{\ell n} = \sqrt{a_{\ell n}^2 + b_{\ell n}^2} \tag{2.4.8}$$

$$\phi_{\ell n} = -\tan^{-1} \frac{a_{\ell n}}{b_{\ell n}} \tag{2.4.9}$$

$$v_a(t) = \sum_{n=1,3,5,\ldots}^{\infty} E_1 (a_{van} \cos n\omega t + b_{van} \sin n\omega t) \tag{2.4.10}$$

$$= \sum_{n=1,3.5,\ldots}^{\infty} E_1 K_{van} \sin(n\omega t - \phi_{van}) \tag{2.4.11}$$

where

$$K_{van} = \sqrt{a_{van}^2 + b_{van}^2} \tag{2.4.12}$$

$$\phi_{van} = -\tan^{-1} \frac{a_{van}}{b_{van}} \tag{2.4.13}$$

The results will be presented in a normalized form using the normalizing factors, K and E_1, for current and voltage respectively. The normalization factor K represents the maximum value of source (stator) current per phase when the bridge-input terminals are short circuited. E_1 represents the maximum value of voltage per phase induced in the source (stator) winding.

Normalized Fourier coefficients a_{an}, b_{an}, $a_{\ell n}$, $b_{\ell n}$, a_{van}, b_{van} and $a_{\ell o}$ are given by the well known integrals.

$$a_{an} = \frac{2}{TK} \int_0^T i_a(t) \cos n\omega t \, dt, \quad n \geq 1 \tag{2.4.14}$$

$$b_{an} = \frac{2}{TK} \int_0^T i_a(t) \sin n\omega t \, dt, \quad n \geq 1 \tag{2.4.15}$$

$$a_{\ell n} = \frac{2}{TK} \int_0^T i_\ell(t) \cos n\omega t \, dt, \quad n \geq 1 \tag{2.4.16}$$

$$b_{\ell n} = \frac{2}{TK} \int_0^T i_\ell(t) \sin n\omega t \, dt, \quad n \geq 1 \tag{2.4.17}$$

$$a_{van} = \frac{2}{TE_1} \int_0^T v_a(t) \cos n\omega t \, dt, \quad n \geq 1 \tag{2.4.18}$$

$$b_{van} = \frac{2}{TE_1} \int_0^T v_a(t) \sin n\omega t \, dt, \quad n \geq 1 \tag{2.4.19}$$

$$a_{\ell o} = \frac{1}{TK} \int_0^T i_\ell(t) \, dt = K_{\ell o} \tag{2.4.20}$$

where

$$T = \frac{1}{f} \tag{2.4.21}$$

Expressions for various voltages and currents are fairly complicated and lengthy. Therefore, numerical method (Romberg integration [26]) and a digital computer (IBM 360) were used for evaluating the Fourier coefficients.

Normalized Fourier coefficients of order 1, 3, 5, 7, 9 and 11 for i_a; 0, 6, 12, 18, 24 and 30 for i_ℓ; and only the fundamental component for v_a were evaluated. Computed angles and normalized magnitudes are plotted with dimensionless circuit constants (X_L/X_C) and (X_L/R_ℓ) as

parameters. In all the calculations, the ratio (X_L/X_C) is varied from 0 to 0.4 with intermediate values at 0.025, 0.05, 0.1 and 0.2. It should be mentioned here that $(X_L/X_C) = 0$ corresponds to the case of no capacitors at bridge-inputs. Figure 13 through Figure 37 show the results.

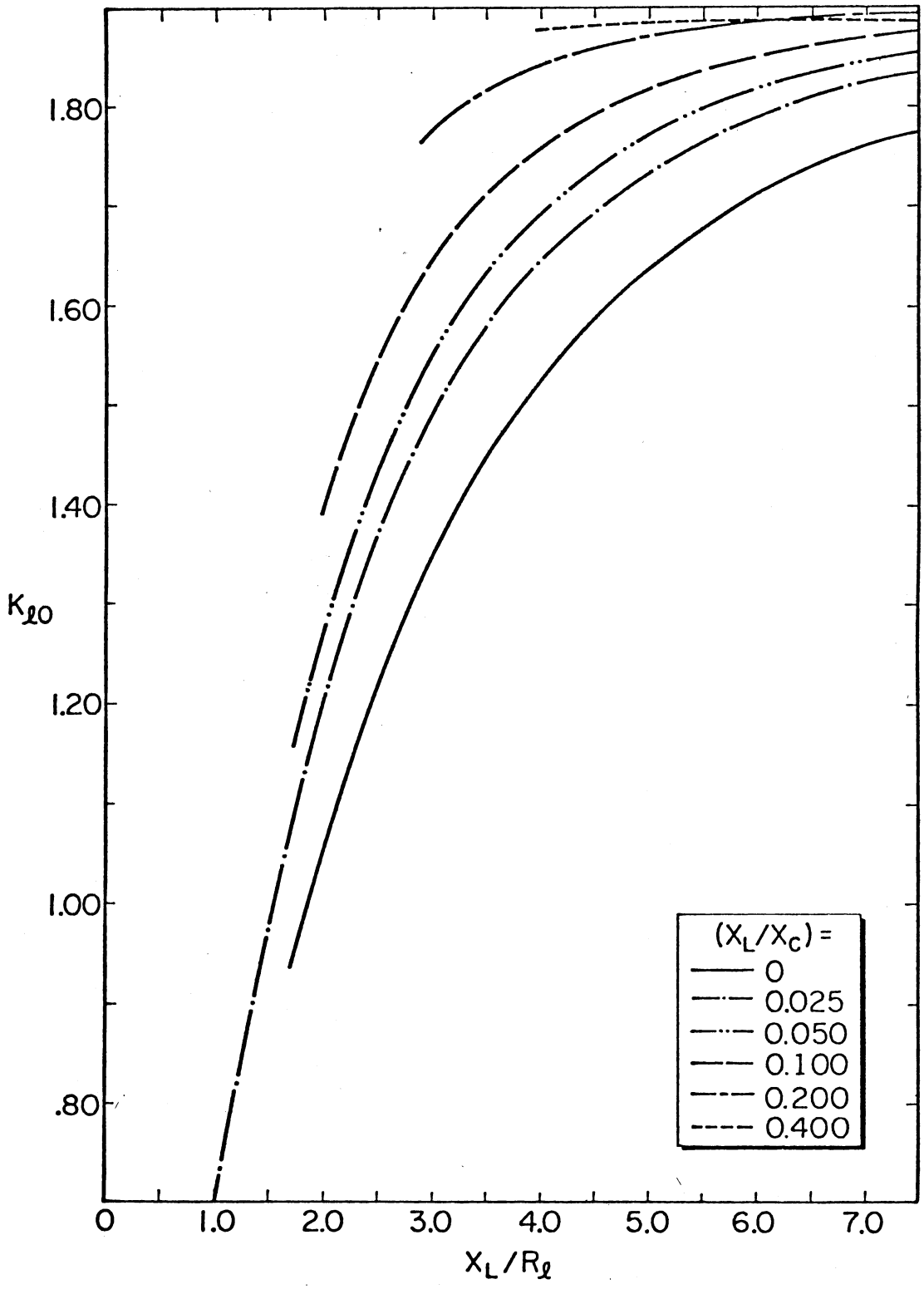

Figure 13. Theoretical Values of $K_{\ell o}$

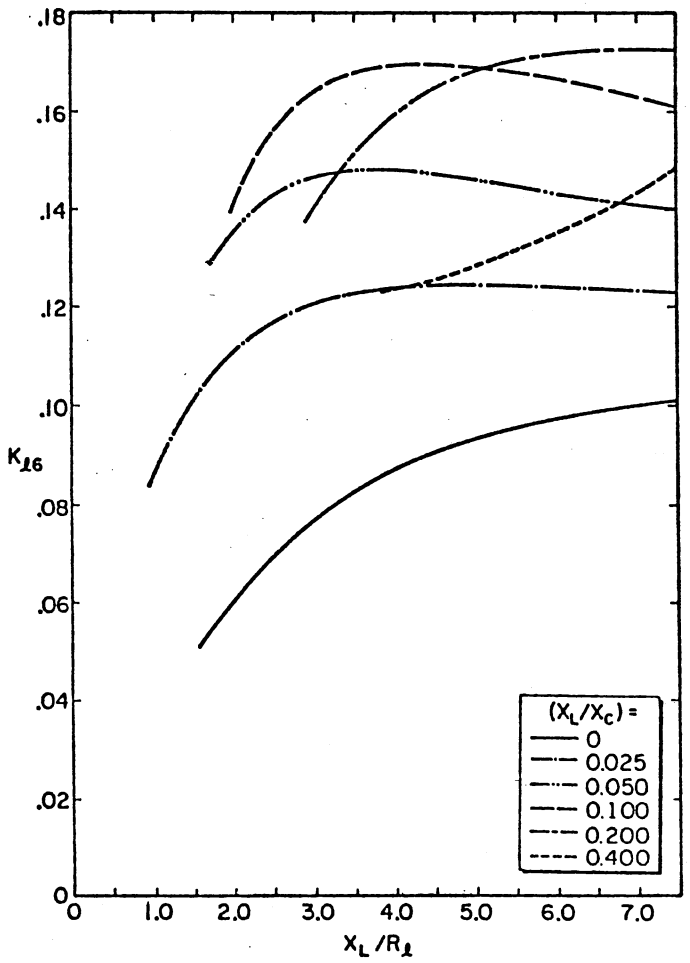

Figure 14. Theoretical Values of $K_{\ell 6}$

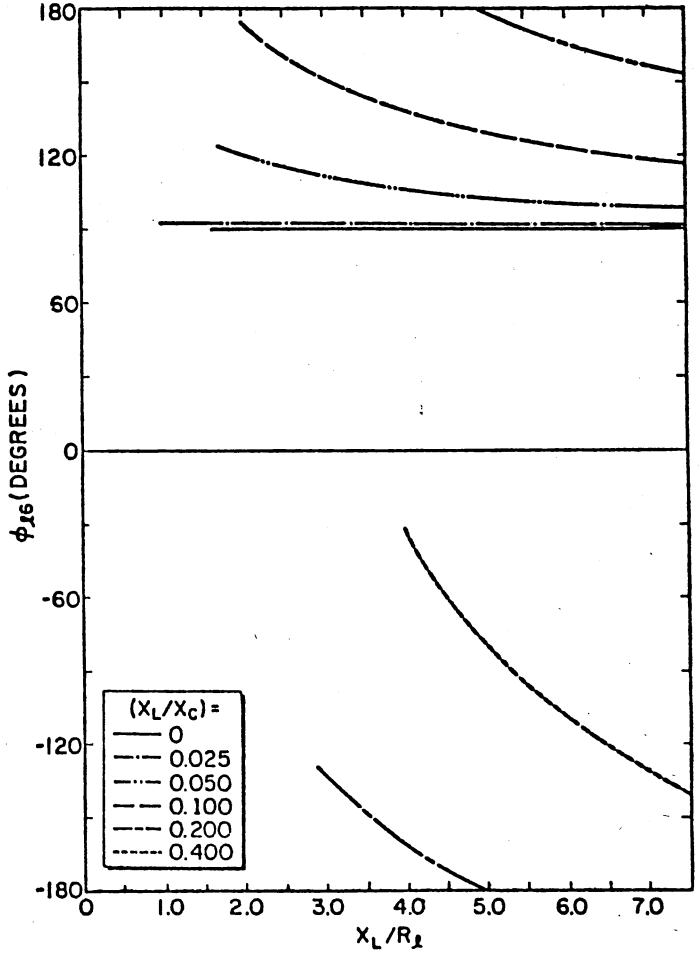

Figure 15. Theoretical Values of $\phi_{\ell 6}$

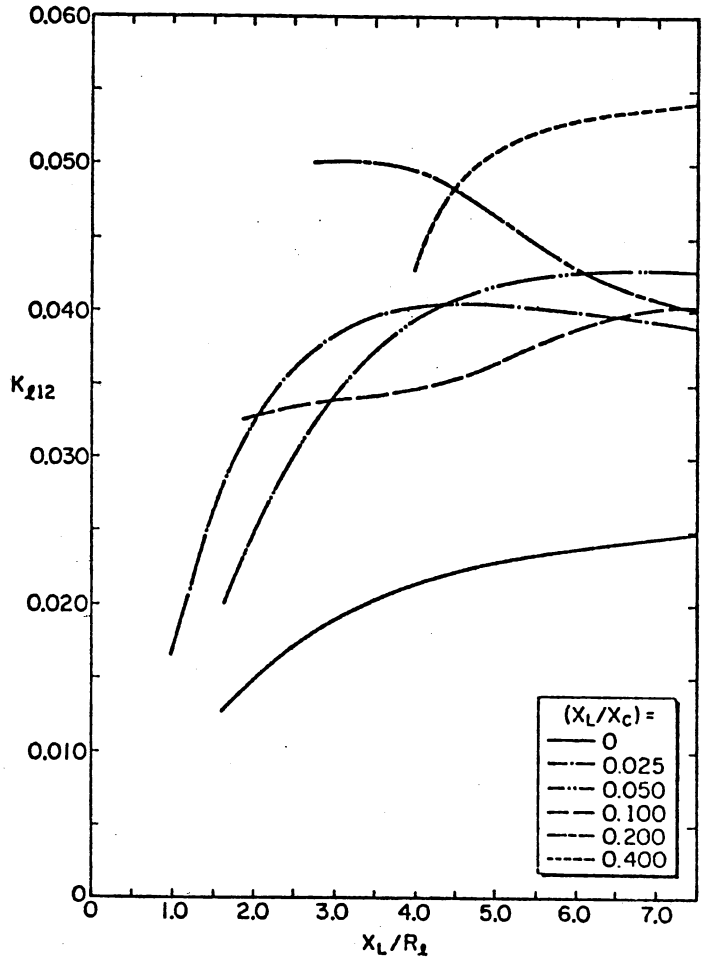

Figure 16. Theoretical Values of $K_{\ell 12}$

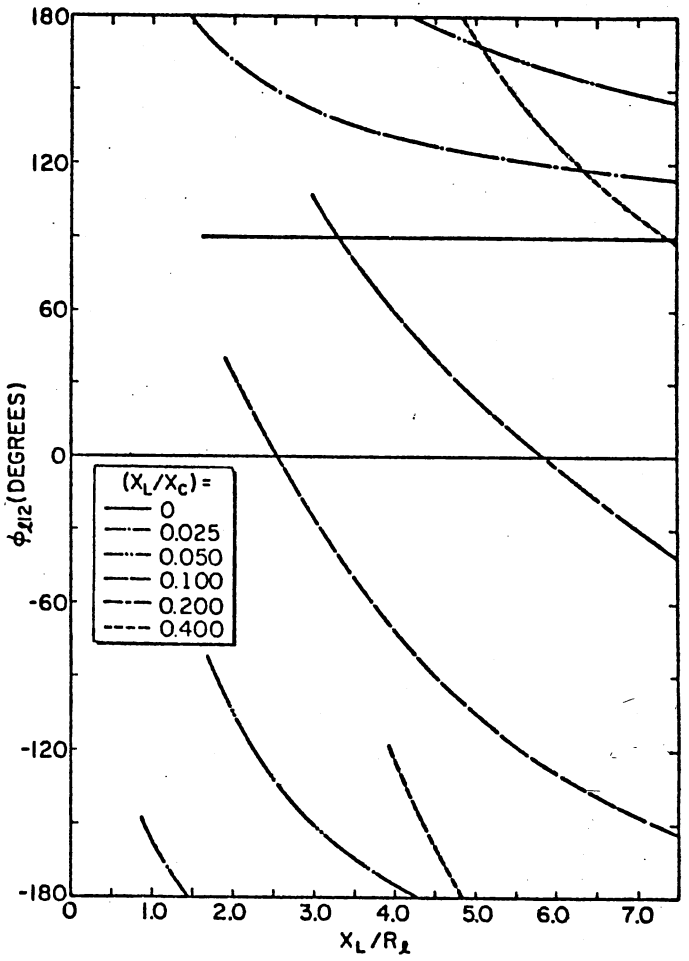

Figure 17. Theoretical Values of $\phi_{\ell 12}$

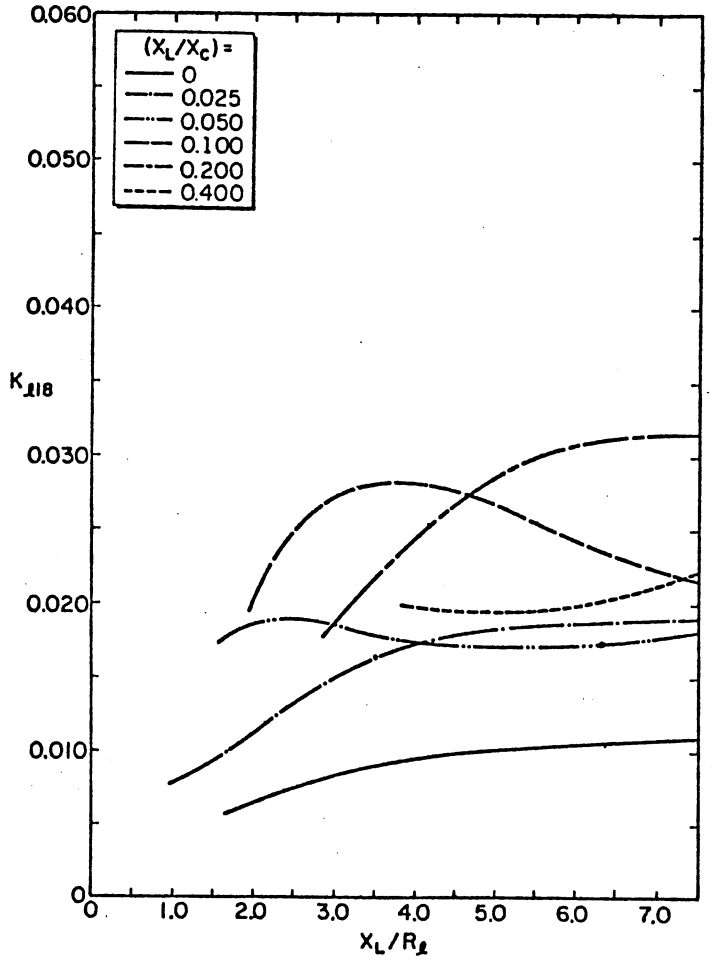

Figure 18. Theoretical Values of $K_{\ell 18}$

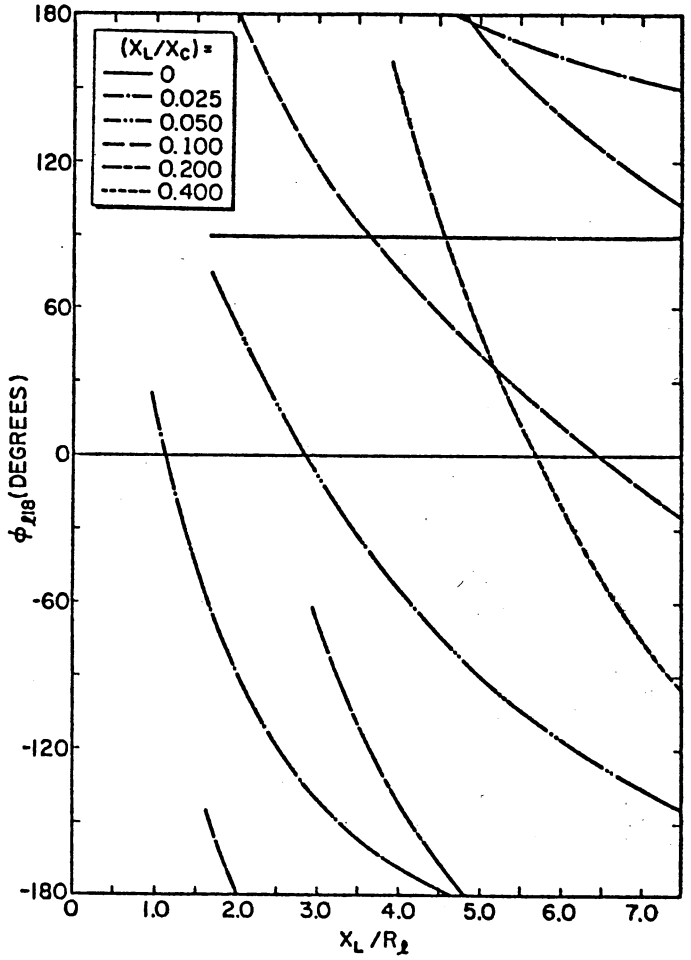

Figure 19. Theoretical Values of $\phi_{\ell 18}$

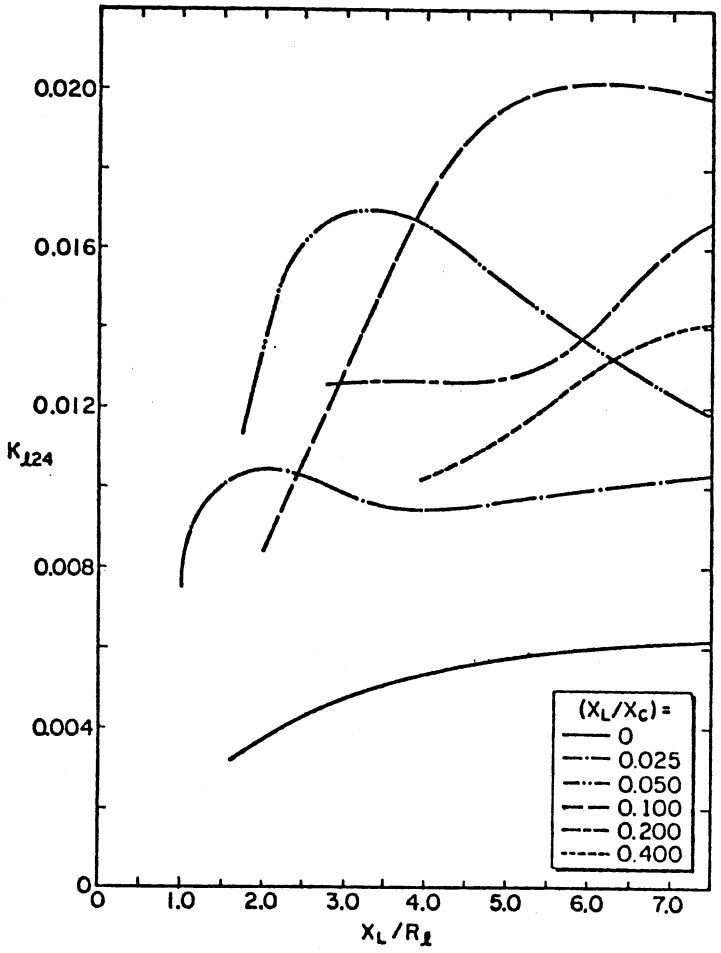

Figure 20. Theoretical Values of $K_{\ell 24}$

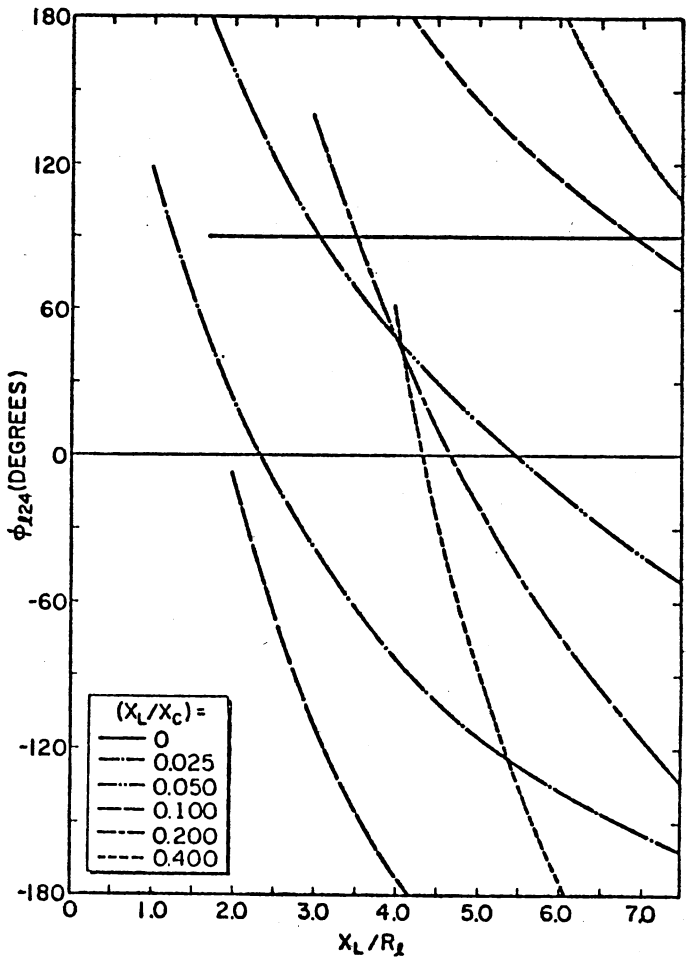

Figure 21. Theoretical Values of $\phi_{\ell 24}$

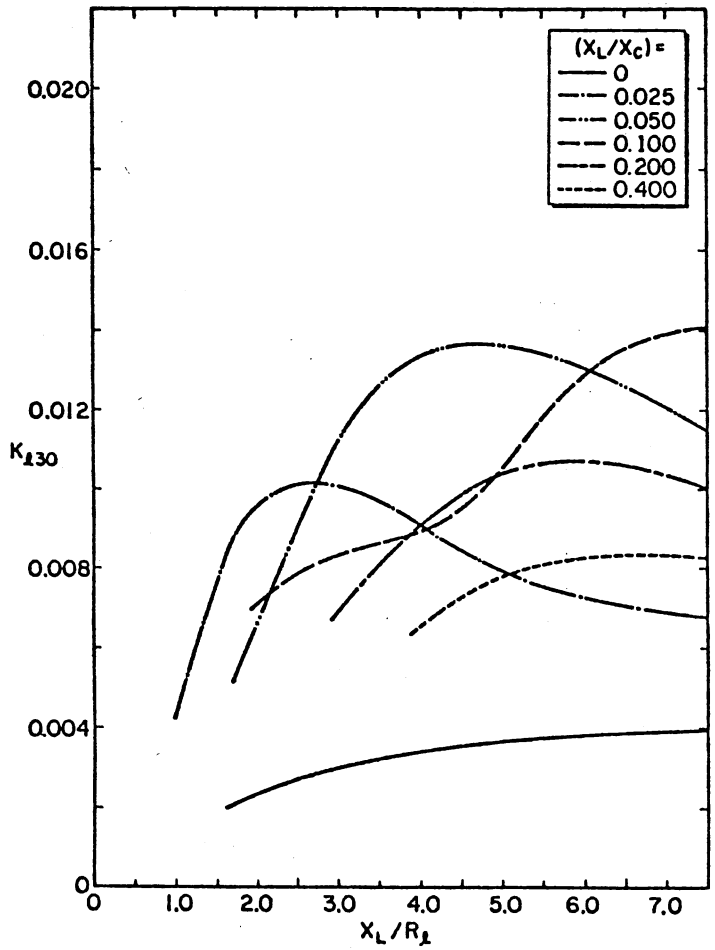

Figure 22. Theoretical Values of $K_{\ell 30}$

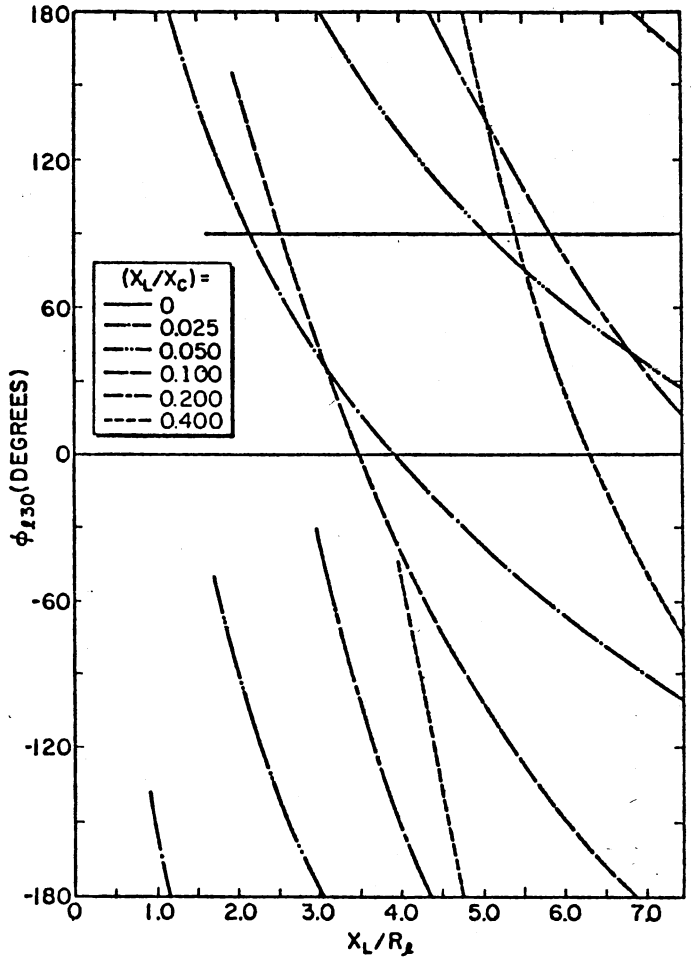

Figure 23. Theoretical Values of $\phi_{\ell 30}$

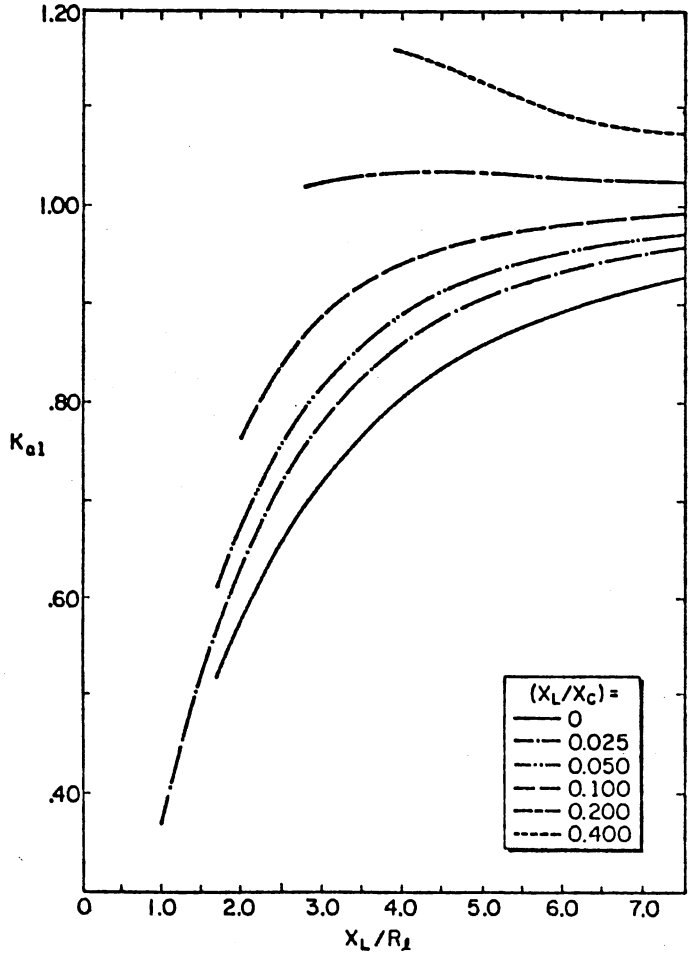

Figure 24. Theoretical Values of K_{al}

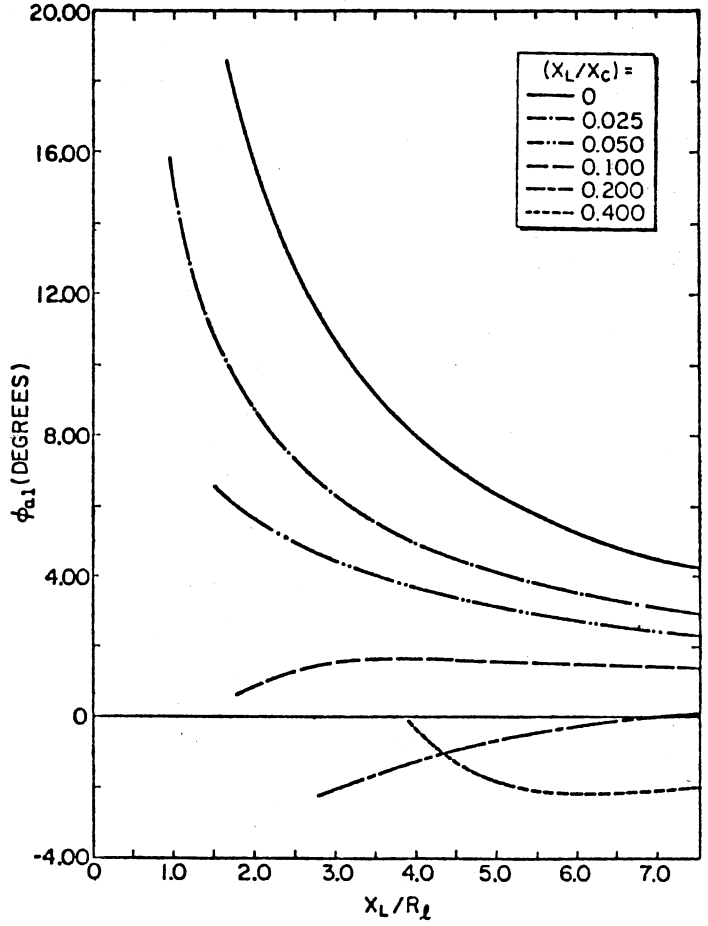

Figure 25. Theoretical Values of ϕ_{al}

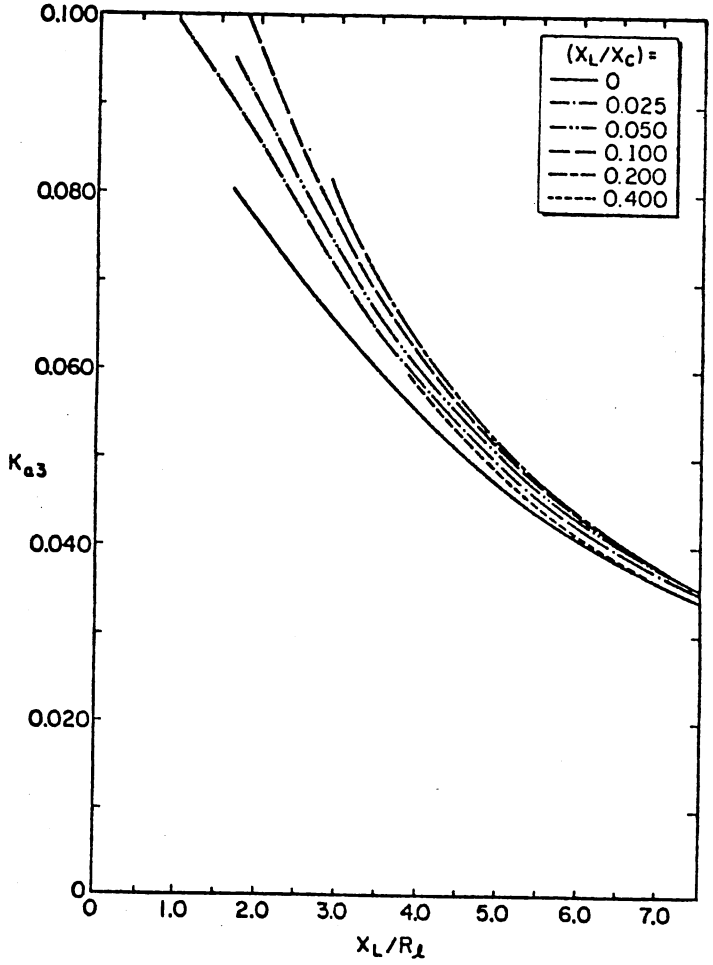

Figure 26. Theoretical Values of K_{a3}

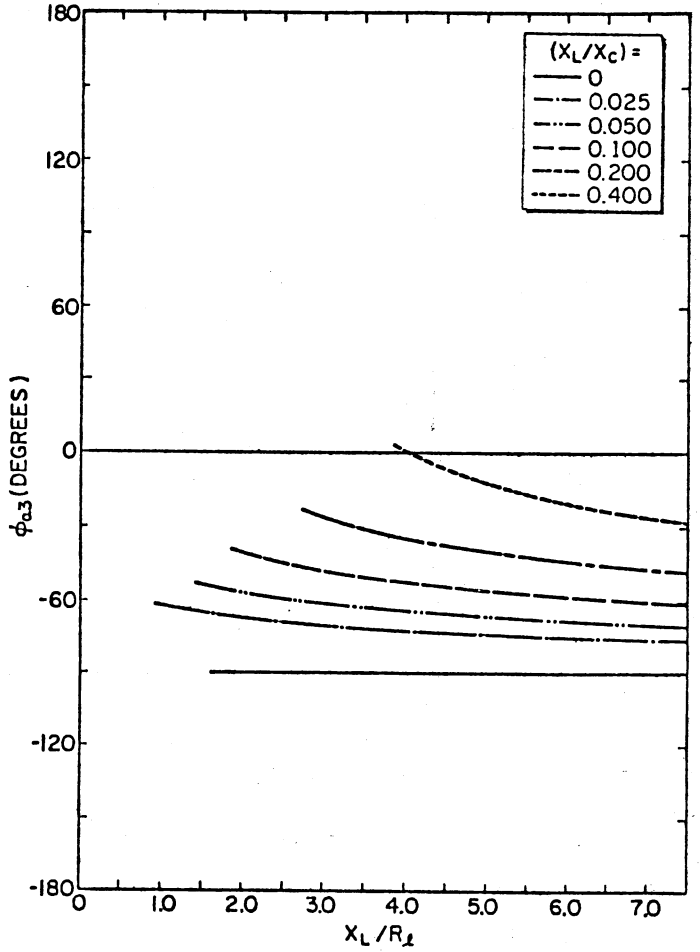

Figure 27. Theoretical Values of ϕ_{a3}

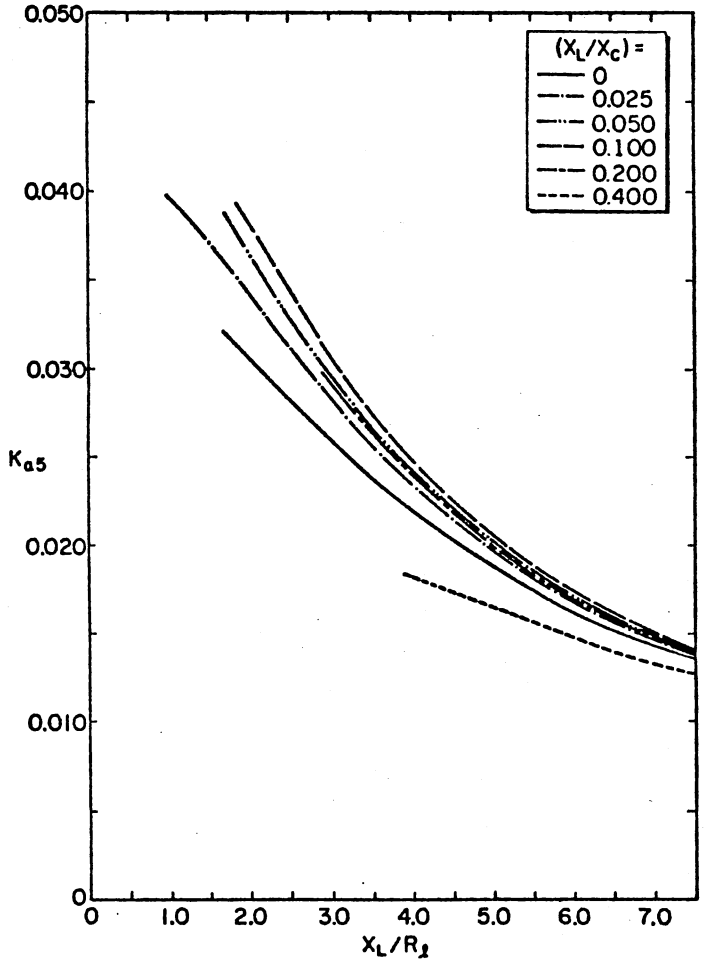

Figure 28. Theoretical Values of K_{a5}

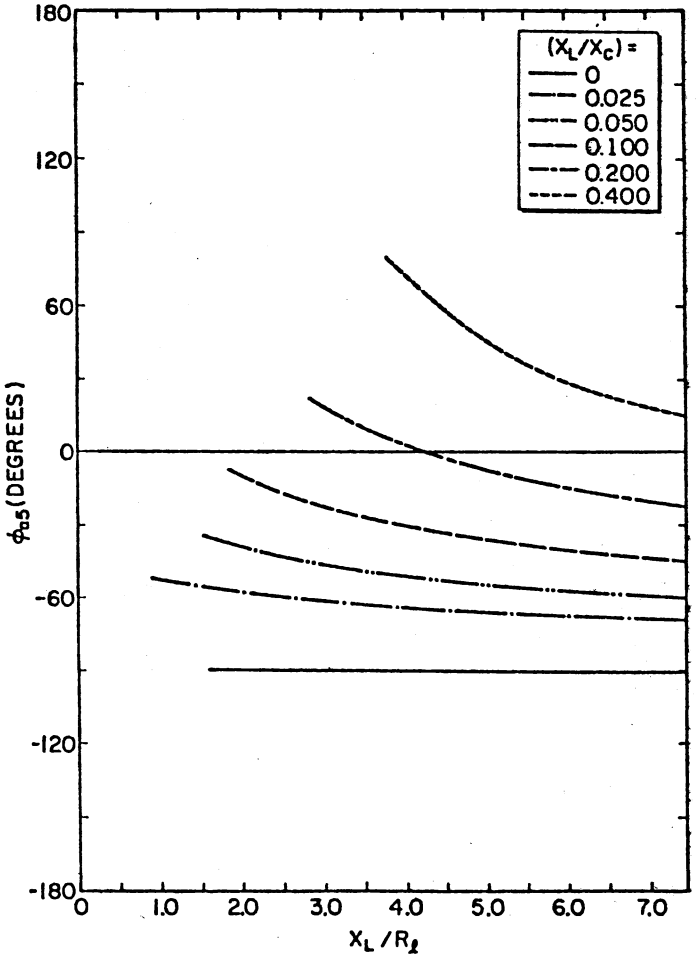

Figure 29. Theoretical Values of ϕ_{a5}

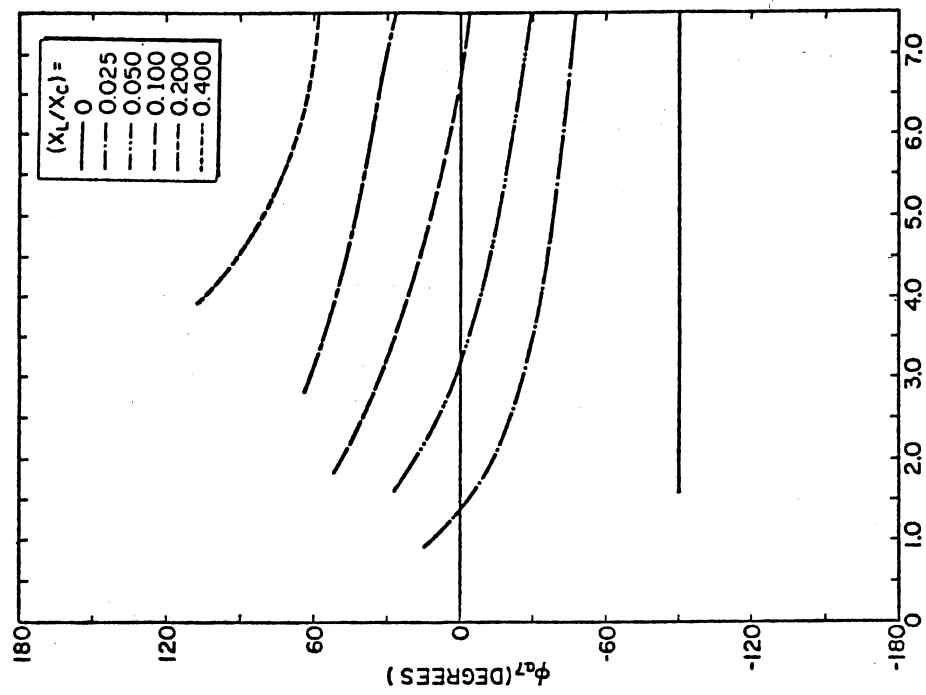

Figure 31. Theoretical Values of ϕ_{a7}

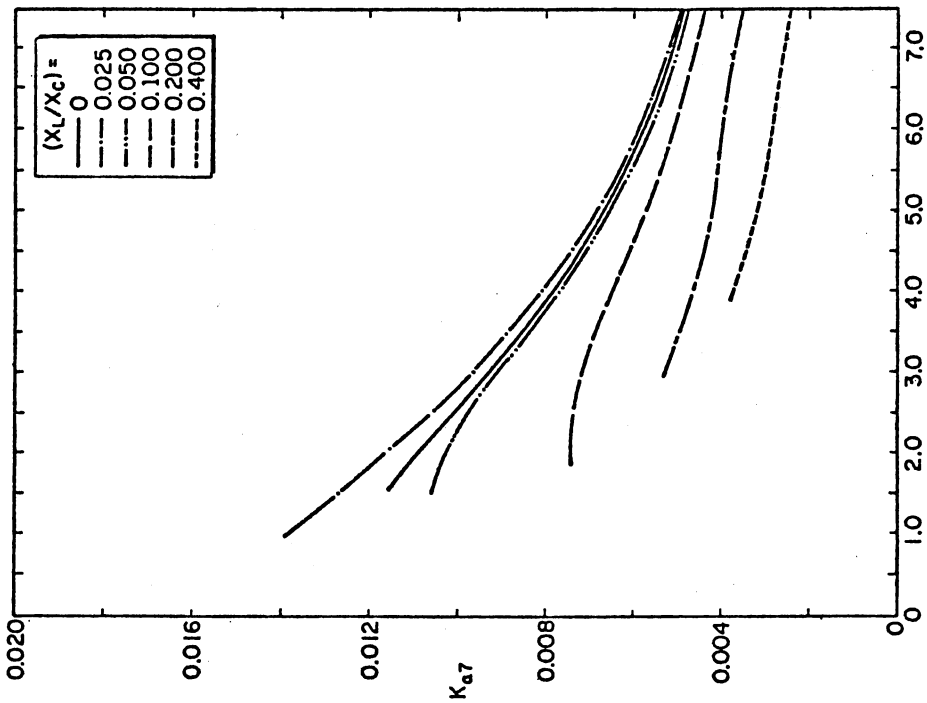

Figure 30. Theoretical Values of K_{a7}

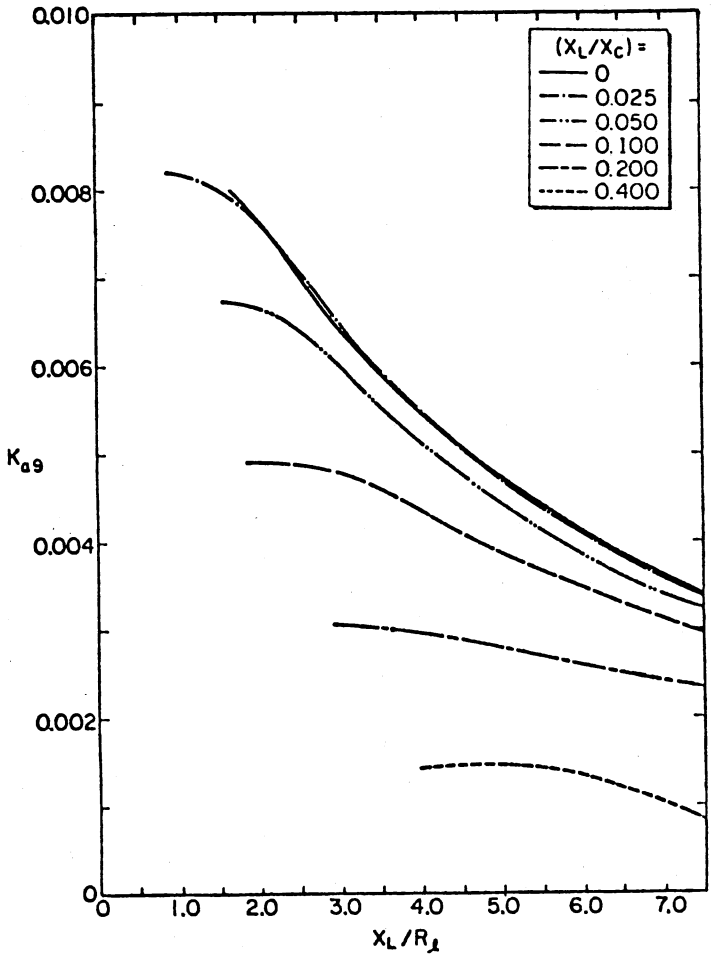

Figure 32. Theoretical Values of K_{a9}

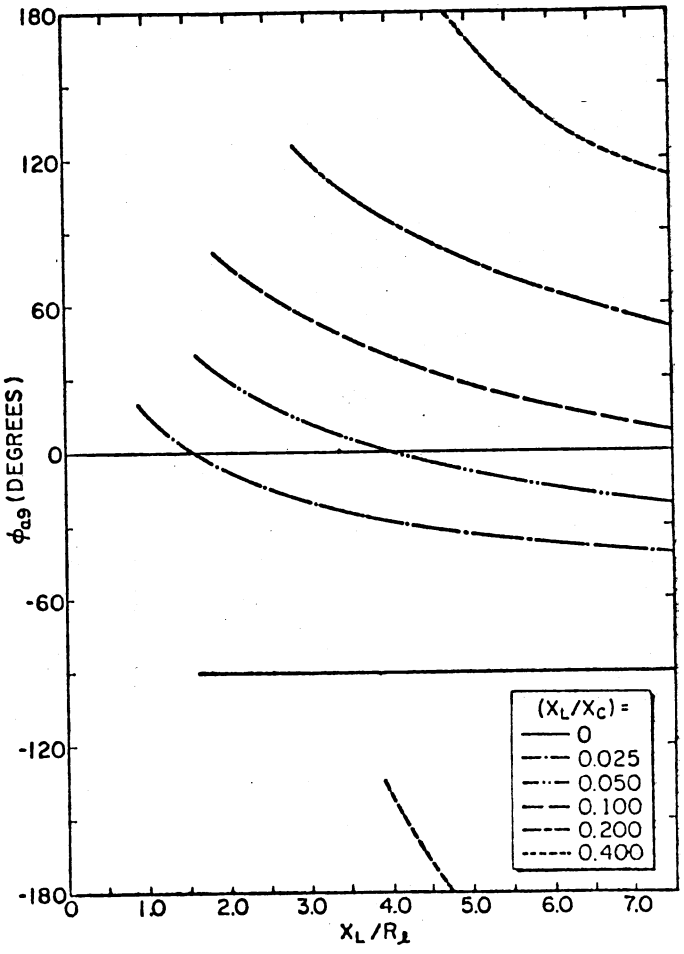

Figure 33. Theoretical Values of ϕ_{a9}

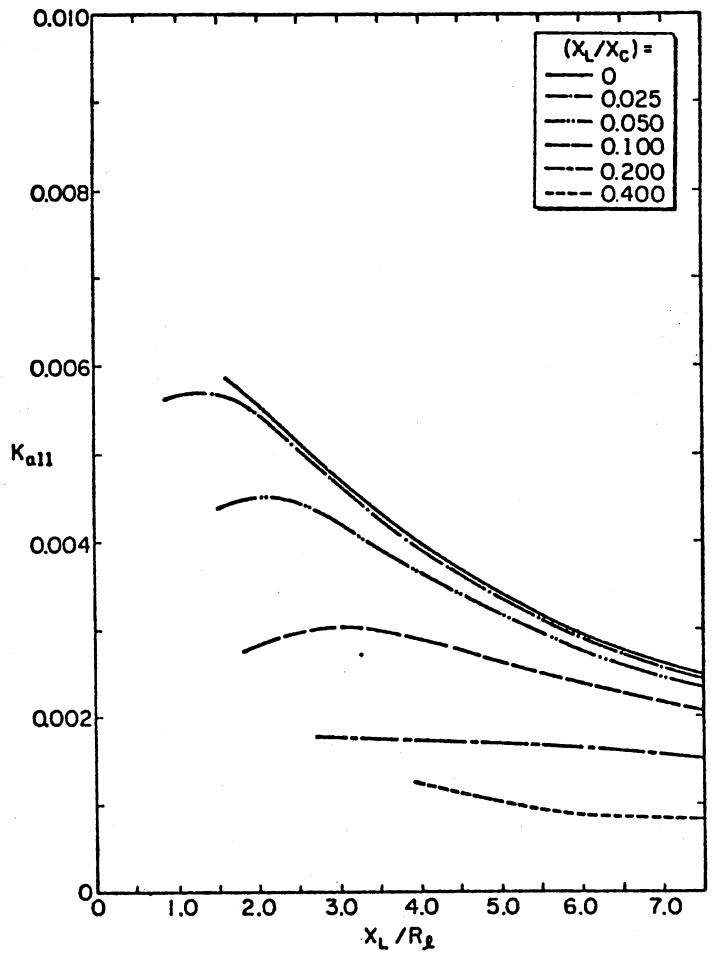

Figure 34. Theoretical Values of K_{all}

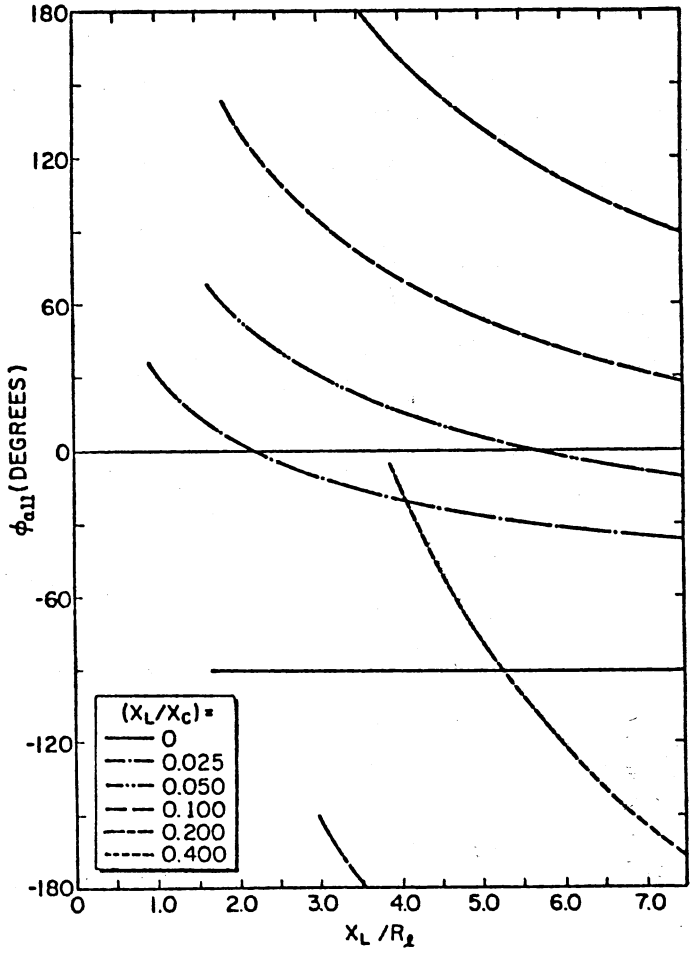

Figure 35. Theoretical Values of ϕ_{all}

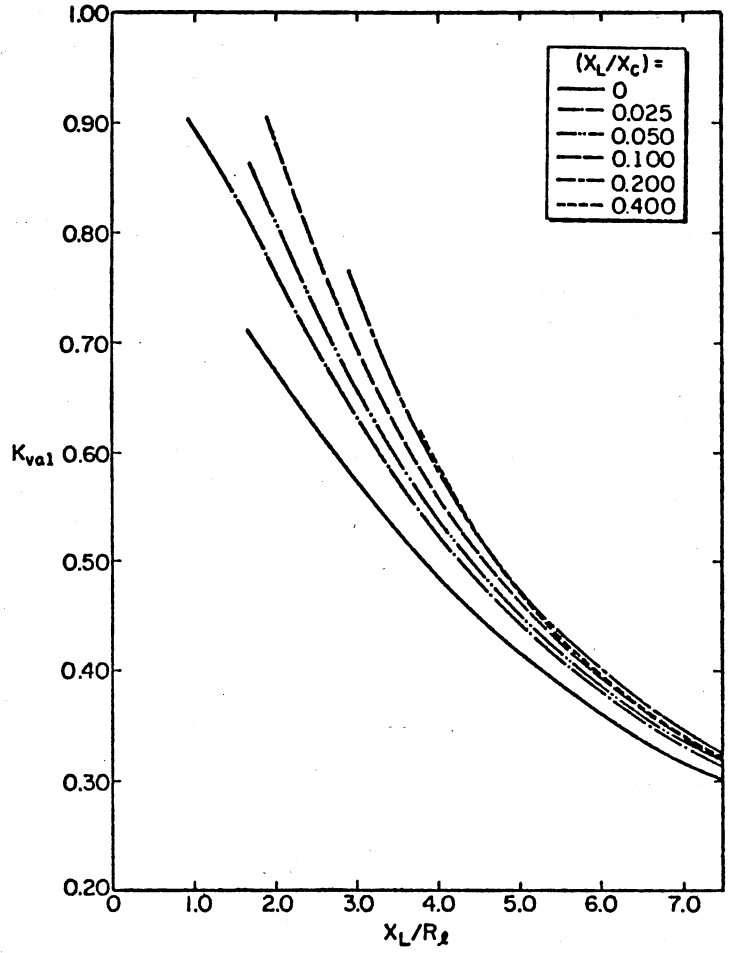

Figure 36. Theoretical Values of K_{val}

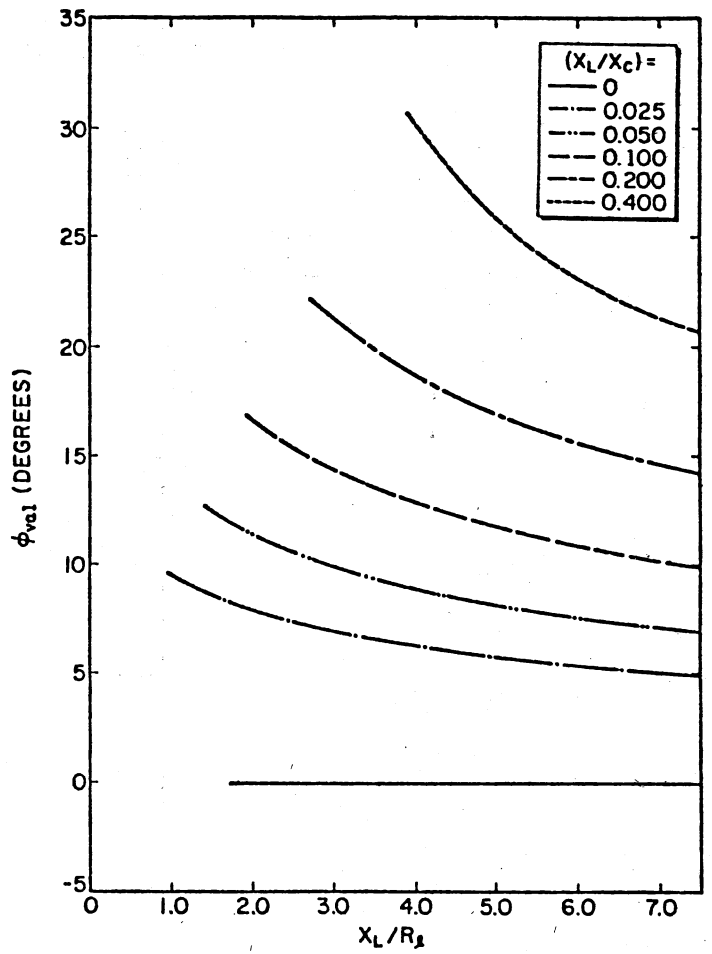

Figure 37. Theoretical Values of ϕ_{val}

CHAPTER III

IDEALIZED MODEL OF FIELD MODULATED GENERATOR SYSTEM

3.1 Introduction

In recent years, there has been a growing interest in the judicious synthesis of solid-state switching devices and rotating machines to achieve a variety of performance characteristics not obtainable from machines alone [27]. Availability of economical high-powered switching devices such as thyristors and diodes is accelerating this process. Various power conditioning circuits for ac and dc motors, frequency converters and cycloconverters are examples of this trend. Field modulated generator systems (FMGS) belong to this growing list. They have promising applications in the field of unconventional power generation and electric drives.

A typical procedure to develop understanding of any sophisticated device is to formulate a mathematical model, which can then be used to better design, scale and utilize that device or system. The task of modeling FMGS [28] essentially involves the synthesis of parallel-bridge rectifier system (PBRS) analysis and machine analysis. PBRS with bridge-input capacitors under resistive loads has been analyzed and harmonic contents of key waveforms were evaluated in Chapter II. This Chapter presents the development of idealized alternator model and the manner in which it is synthesized with PBRS studies with modulation to

form the idealized FMGS model.

Section 3.2 presents the idealizing assumptions made in the development of the model. Section 3.3 details the procedures involved in the application of the results of PBRS studies to the field modulated case. Section 3.4 deals with alternator analysis, performance equations and the development of vector diagrams.

3.2 Assumptions

Coupled circuit models and dynamic circuit theory are commonly employed for analyzing rotating machines [29,30]. However, in the case of field modulated generators, it is more convenient to work in terms of air-gap magnetomotive forces and flux densities because of the non-sinusoidal nature of the terminal voltages at the stator winding terminals under load. Non-sinusoidal terminal voltages are the result of output rectification inherent in the operation of the frequency down conversion scheme. This approach has the added advantage of relating the performance of the machine to such design parameters as main dimensions, flux densities, winding factors and air-gap length and consequently leading to design optimization studies more easily. The following assumptions are made in the analysis presented in this Chapter.

A) A two-pole machine is considered (See Figure 38).

B) Stator and rotor winding resistances are neglected.

C) Modulation frequency is much smaller (<10 per cent) than the basic rotational frequency of the machine throughout the operating speed range.

D) Transformer voltages are neglected as small in comparison with

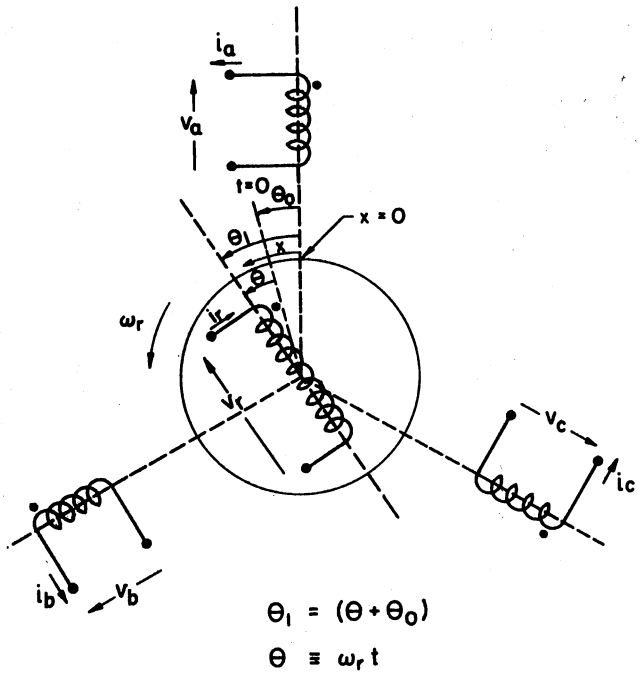

Figure 38. Stator and Rotor Coil Arrangement for the Idealized Alternator

speed voltages in the stator windings.

E) Only fundamental components of stator and rotor winding currents are considered.

F) Only fundamental components of flux and MMF distributions in the air-gap are considered.

G) Saturation effects are neglected.

H) Rotor and stator iron are infinitely permeable.

I) All solid-state devices are ideal.

The machine is modeled as shown in Figure 39 using ideal sources and commutating inductances L per phase.

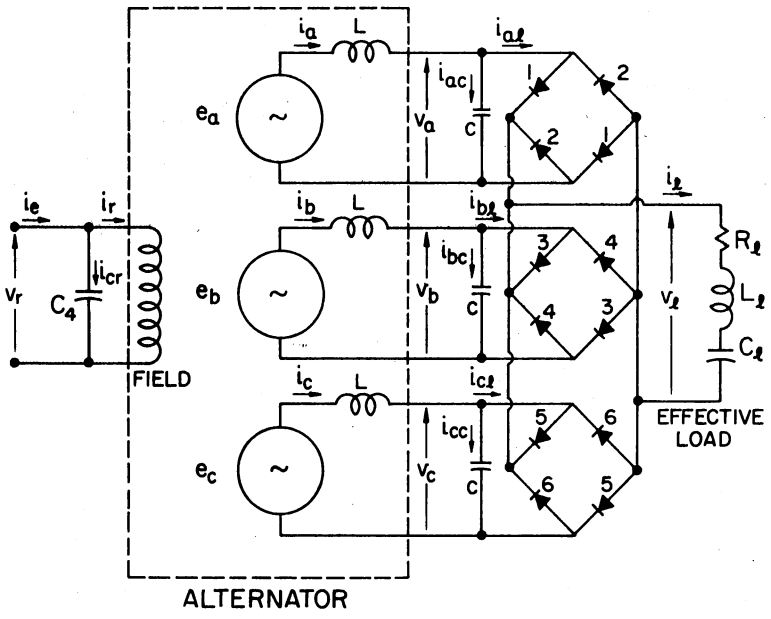

Figure 39. Idealized Circuit Model of FMGS

3.3 Extension of PBRS Studies to the Field Modulated Case

The waveforms discussed in Chapter II are valid for an alternator-PBRS combination under dc excitation, assuming the induced stator phase voltages are purely sinusoidal. Based on this understanding, FMGS waveforms under resistive loads and simusoidal ac excitation (field modulation) can be approximated by using proper modulation factors to the expressions already derived.

Figure 40 shows the general nature of e_a, v_a and i_a waveforms under modulation (with ac sinusoidal excitation) and resistive load. The maximum value of e_a (denoted as E_1) is intentionally chosen to coincide with the peak of the modulation envelope for convenience in

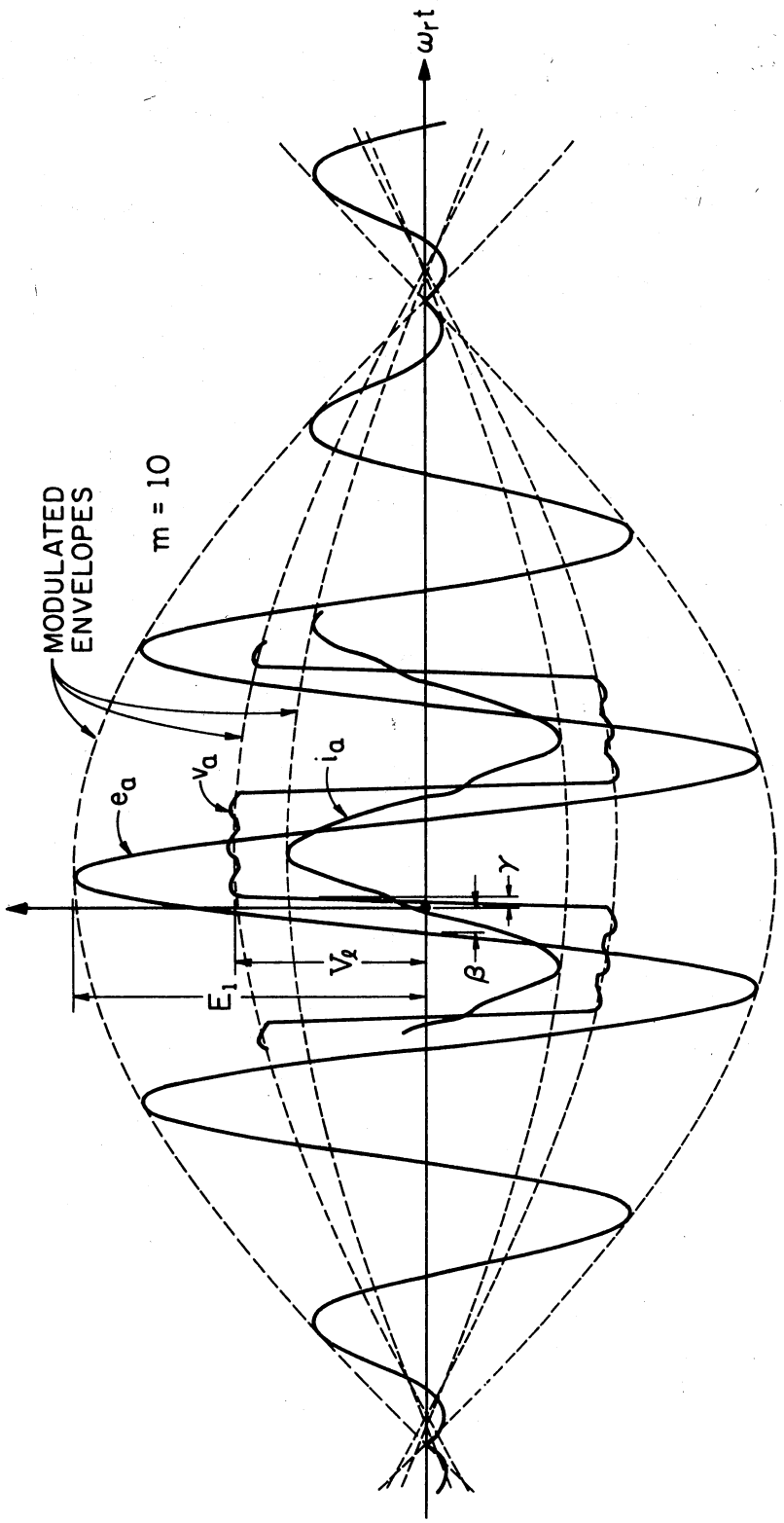

Figure 40. General Nature of e_a, v_a and i_a Waveforms Under Modulation

illustration. It can be seen from Section 2.3 that consideration of complete expressions will be very involved. Therefore, as a first approximation, only fundamental components of currents and voltages are considered. Figure 41 shows the fundamental components and their relative phase positions. This is further illustrated in the high-frequency (ω_r) vector diagram shown in Figure 42. Reference is chosen at t=0 in this vector diagram and in Figure 41.

Magnitudes and relative phase angles of fundamental quantities have already been numerically evaluated by Fourier techniques in Chapter II from the waveforms obtained from an analysis of the circuit model shown in Figure 3. Now define two normalized coefficients $K_{\ell o}$ and K_{a1} as follows.

$$K_{\ell o} \equiv \frac{I_{\ell o}}{K} \tag{3.3.1}$$

$$K_{a1} \equiv \frac{I_{a1}}{K} = \frac{I_1}{K} \tag{3.3.2}$$

E_1 and I_1 can be expressed in terms of $I_{\ell o}$ by combining equations (3.3.1), (3.3.2) and the definition of K.

$$I_1 = K\, K_{a1} = \frac{K_{a1}}{K_{\ell o}}\, I_{\ell o} \tag{3.3.3}$$

$$E_1 = K\, X_L = \frac{X_L}{K_{\ell o}}\, I_{\ell o} \tag{3.3.4}$$

Equations (3.3.3) and (3.3.4) are applicable for the circuit model (Figure 39) with dc excitation. To consider the field-modulated case, it will be assumed that the maximum values V_{a1} and V_ℓ occur at the same instant of time. With this assumption, $I_{\ell o}$ can be replaced by I_ℓ, and E_1 and I_1 can be expressed as follows.

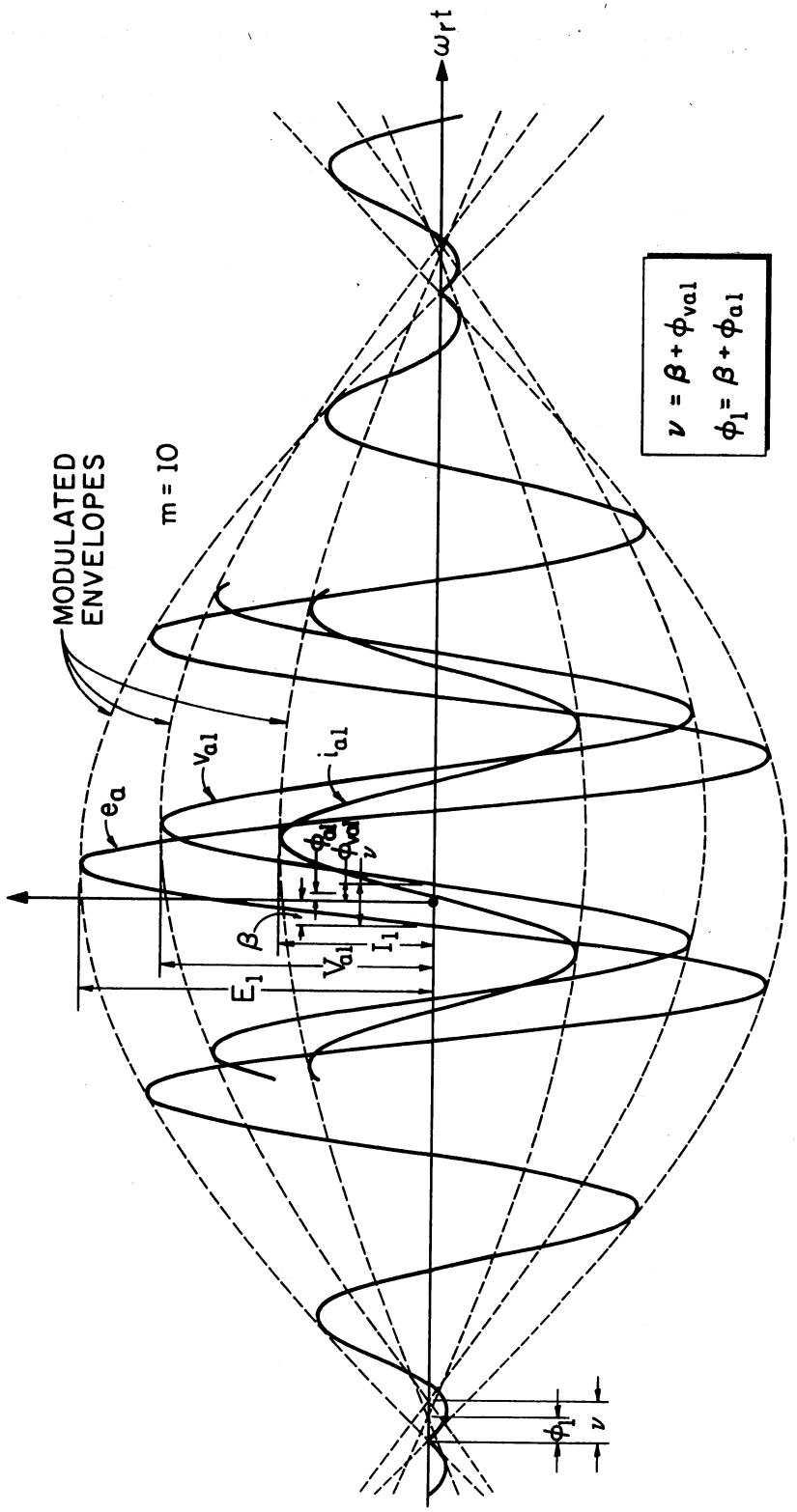

Figure 41. Fundamental Components of e_a, v_a and i_a Waveforms Under Modulation

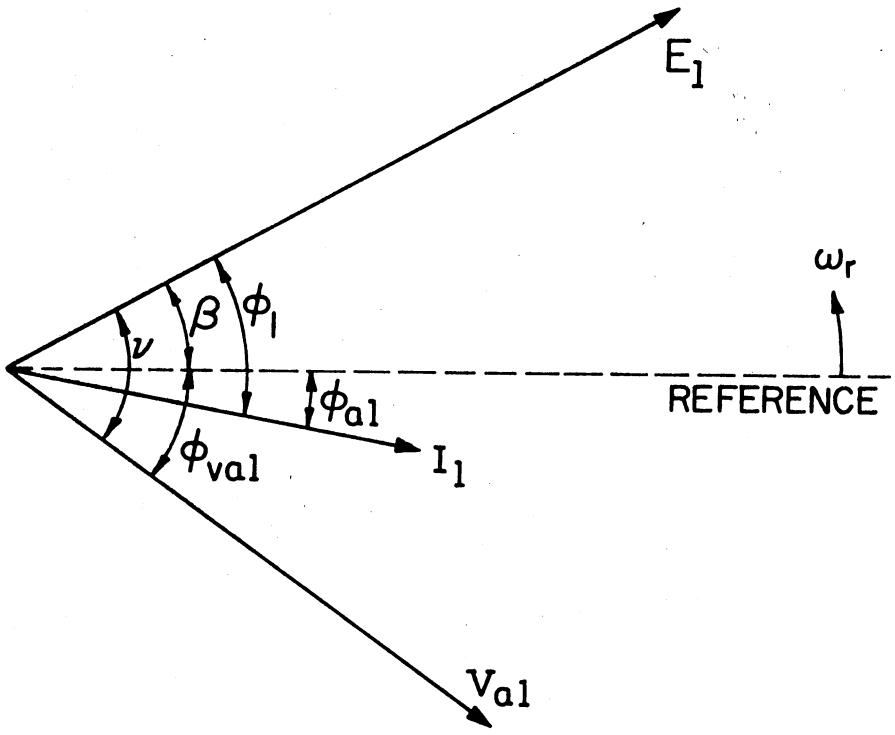

Figure 42. Vector Diagram Illustrating Phase Relationships Between E_1, I_1 and V_{a1} in an Idealized PBRS With a Modulated Source and Resistive Load

$$I_1 = \frac{K_{a1}}{K_{\ell o}} I_\ell \tag{3.3.5}$$

$$E_1 = \frac{X_L}{K_{\ell o}} I_\ell \tag{3.3.6}$$

With E_1 and I_1 known, machine physical data and circuit parameters can be used in conjunction with vector diagrams to obtain several important operating characteristics. These will be discussed in Section 3.4.

Using the relationships derived in ω_r up to this point, it is

possible to develop a low frequency (ω_m) vector diagram. The nature of relative angular frequencies suggests that phase angle in ω_r as viewed from ω_m side would appear to be "scaled down" by the modulation frequency ratio, m, where

$$m = (\omega_r/\omega_m) \tag{3.3.7}$$

A new set of angles are now defined as follows.

$$\theta_o' = \theta_o/m \tag{3.3.8}$$

$$\delta' = \delta/m \tag{3.3.9}$$

$$\nu' = \nu/m \tag{3.3.10}$$

$$\beta' = \beta/m \tag{3.3.11}$$

$$\phi_{val}' = \phi_{val}/m \tag{3.3.12}$$

$$\phi_l' = \phi_l/m \tag{3.3.13}$$

where

$$\nu = \beta + \phi_{val} \tag{3.3.14}$$

$$\phi_l = \beta + \phi_{al} \tag{3.3.15}$$

Figure 43 shows the phase relationships between the quantities I_ℓ, E_l and V_ℓ. Note that all these are at the low frequency ω_m. V_ℓ is chosen as the reference for convenience. Therefore, the reference line corresponding to $\omega_r t = 0$ used in Figure 42 would be somewhere in between V_ℓ and E_l.

Referring to Figure 43, the following vector relationship can be derived.

$$E_l = V_\ell + V_L \tag{3.3.16}$$

$$= V_\ell + (E_l \cos\nu' - V_\ell) + j\, E_l \sin\nu' \tag{3.3.17}$$

In terms of an equivalent impedance Z_{eq}, one can write

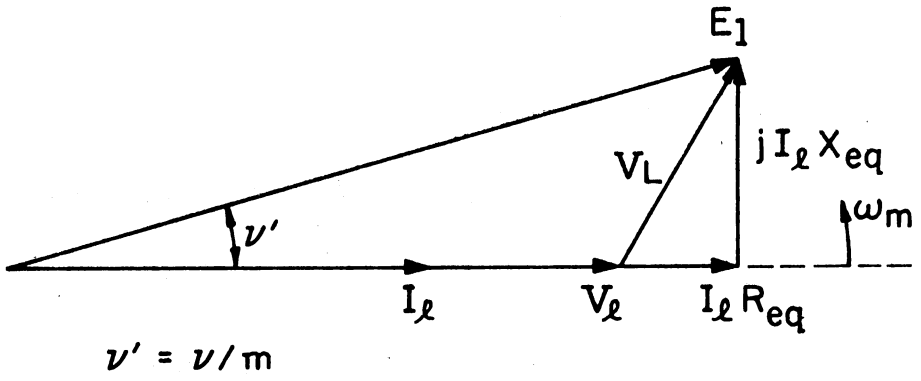

Figure 43. Vector Diagram Illustrating Phase Relationships Between E_1, I_ℓ and V_ℓ in an Idealized PBRS With a Modulated Source and Resistive Load

$$E_1 = V_\ell + I_\ell Z_{eq} \tag{3.3.18}$$

$$= V_\ell + I_\ell R_{eq} + j I_\ell X_{eq} \tag{3.3.19}$$

where

$$R_{eq} = (E_1 \cos\nu' - V_\ell)/I_\ell \tag{3.3.20}$$

$$X_{eq} = (E_1 \sin\nu')/I_\ell \tag{3.3.21}$$

and

$$Z_{eq} = R_{eq} + j X_{eq} \tag{3.3.22}$$

Equation (3.3.19) corresponds to the low frequency (ω_m) equivalent circuit shown in Figure 44. Notice that the angle ν' is a function of (X_L/X_C) and (X_L/R_ℓ). Therefore, e_ℓ and Z_{eq} are functions of load and circuit parameters.

The relationships developed for PBRS under modulation are coupled with alternator performance equations to formulate an idealized FMGS model in the next Section.

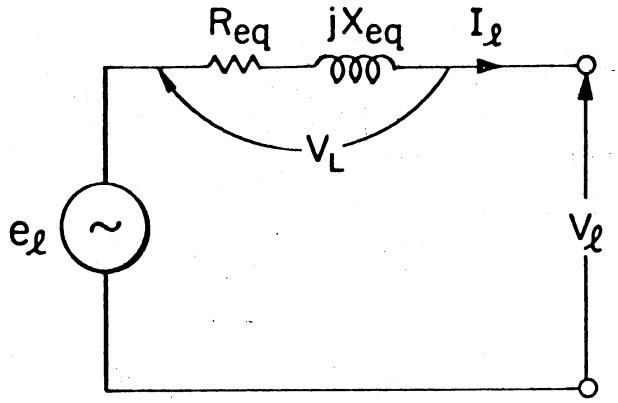

$$e_\ell = E_1 \sin(\omega_m t + \nu')$$

Figure 44. Low Frequency (ω_m) Equivalent Circuit for the Idealized FMGS

3.4 Machine Analysis, Vector Diagrams and Performance Equations

Referring to Figure 38, let the fundamental component of MMF set up by the modulated rotor be

$$m_f = M_f \cos \omega_m t \cos(\omega_r t + \theta_o - \frac{2x}{d}) \qquad (3.4.1)$$

where

$$M_f = N_r I_r k_f \qquad (3.4.2)$$

The resultant MMF in the air-gap, due to the combined action of the fundamental stator and rotor currents will lag the MMF set up by the rotor by an angle δ and the modulation envelope of M_r will lag the rotor winding current by an angle δ' and can be expressed as shown below.

$$m_r = M_r \cos(\omega_m t - \delta') \cos(\omega_r t + \theta_o - \frac{2x}{d} - \delta) \tag{3.4.3}$$

If $\omega_m << \omega_r$, in the normal operating range of the system, δ' will be negligibly small. Then, m_r can be approximated as shown below.

$$m_r = M_r \cos \omega_m t \cos(\omega_r t + \theta_o - \frac{2x}{d} - \delta) \tag{3.4.4}$$

Neglecting transformer voltages, the flux set up by the resultant MMF will induce the following voltages in the three stator windings.

$$e_a = E_1 \cos(\omega_m t - \frac{\pi}{2m} - \delta') \sin(\omega_r t + \theta_o - \delta) \tag{3.4.5}$$

$$e_b = E_1 \cos(\omega_m t - \frac{\pi}{2m} - \delta') \sin(\omega_r t + \theta_o - \delta - \frac{2\pi}{3}) \tag{3.4.6}$$

$$e_c = E_1 \cos(\omega_m t - \frac{\pi}{2m} - \delta') \sin(\omega_r t + \theta_o - \delta + \frac{2\pi}{3}) \tag{3.4.7}$$

Once again, if $\omega_m << \omega_r$, as a first approximation, $(\frac{\pi}{2m} + \delta')$ can be neglected. Then, expressions for the induced voltages in the three stator windings take the form given below.

$$e_a = E_1 \cos \omega_m t \sin(\omega_r t + \theta_o - \delta) \tag{3.4.8}$$

$$e_b = E_1 \cos \omega_m t \sin(\omega_r t + \theta_o - \delta - \frac{2\pi}{3}) \tag{3.4.9}$$

$$e_c = E_1 \cos \omega_m t \sin(\omega_r t + \theta_o - \delta + \frac{2\pi}{3}) \tag{3.4.10}$$

To compute E_1 for a two-pole machine, let Φ_r be the flux per pole. Then,

$$\Phi_r = B_{rav} A_p \tag{3.4.11}$$

$$= (\frac{2}{\pi} B_r)(\frac{\pi d}{2} \ell) \tag{3.4.12}$$

For the idealized machine,

$$B_r = \mu_o M_r / g \tag{3.4.13}$$

Substituting (3.4.13) in (3.4.12) and rearranging, the expression for Φ_r becomes

$$\Phi_r = \mu_o M_r \ell d/g \tag{3.4.14}$$

However,

$$E_1 = \omega_r(N_s k_p k_d) \Phi_r \tag{3.4.15}$$

Substituting (3.4.14) in above, E_1 becomes

$$E_1 = \frac{\mu_o M_r}{g} \omega_r \ell d N_s k_p k_d \tag{3.4.16}$$

Equations (3.4.8) through (3.4.10) give the set of three-phase voltages to be used in the model shown in Figure 39. Fundamental components of stator winding currents can be expressed as follows.

$$i_{a1} = I_1 \cos(\omega_m t - \frac{\pi}{2m} - \delta' - \phi_1') \sin(\omega_r t + \theta_o - \delta - \phi_1) \tag{3.4.17}$$

$$i_{b1} = I_1 \cos(\omega_m t - \frac{\pi}{2m} - \delta' - \phi_1') \sin(\omega_r t + \theta_o - \delta - \phi_1 - \frac{2\pi}{3}) \tag{3.4.18}$$

$$i_{c1} = I_1 \cos(\omega_m t - \frac{\pi}{2m} - \delta' - \phi_1') \sin(\omega_r t + \theta_o - \delta - \phi_1 + \frac{2\pi}{3}) \tag{3.4.19}$$

Following the pattern of approximations made in the development of the idealized and simplified model, the modulating factor is replaced by $\cos(\omega_m t)$. Expressions for the currents then become

$$i_{a1} = I_1 \cos \omega_m t \sin(\omega_r t + \theta_o - \delta - \phi_1) \tag{3.4.20}$$

$$i_{b1} = I_1 \cos \omega_m t \sin(\omega_r t + \theta_o - \delta - \phi_1 - \frac{2\pi}{3}) \tag{3.4.21}$$

$$i_{c1} = I_1 \cos \omega_m t \sin(\omega_r t + \theta_o - \delta - \phi_1 + \frac{2\pi}{3}) \tag{3.4.22}$$

Values of I_1, E_1 and ϕ_1 should be obtained by analyzing the circuit shown in Figure 39 using known values of C, L and effective load impedance at the output terminals of the parallel-bridge rectifier system. This, in general, is not an easy task and several more approximations

may have to be resorted to. For resistive loads, the results derived in Section 3.3 can be used.

Figure 45 illustrates the phase relationship between various fundamental quantities, shown when the modulation amplitude is maximum. The relationship between M_f, M_a and M_r is easily derived.

$$M_f^2 = M_a^2 + M_r^2 + 2M_a M_r \sin \phi_1 \qquad (3.4.23)$$

Maximum value of armature reaction MMF, M_a, is given by

$$M_a = \frac{3}{4} k_p k_d N_s I_1 \qquad (3.4.24)$$

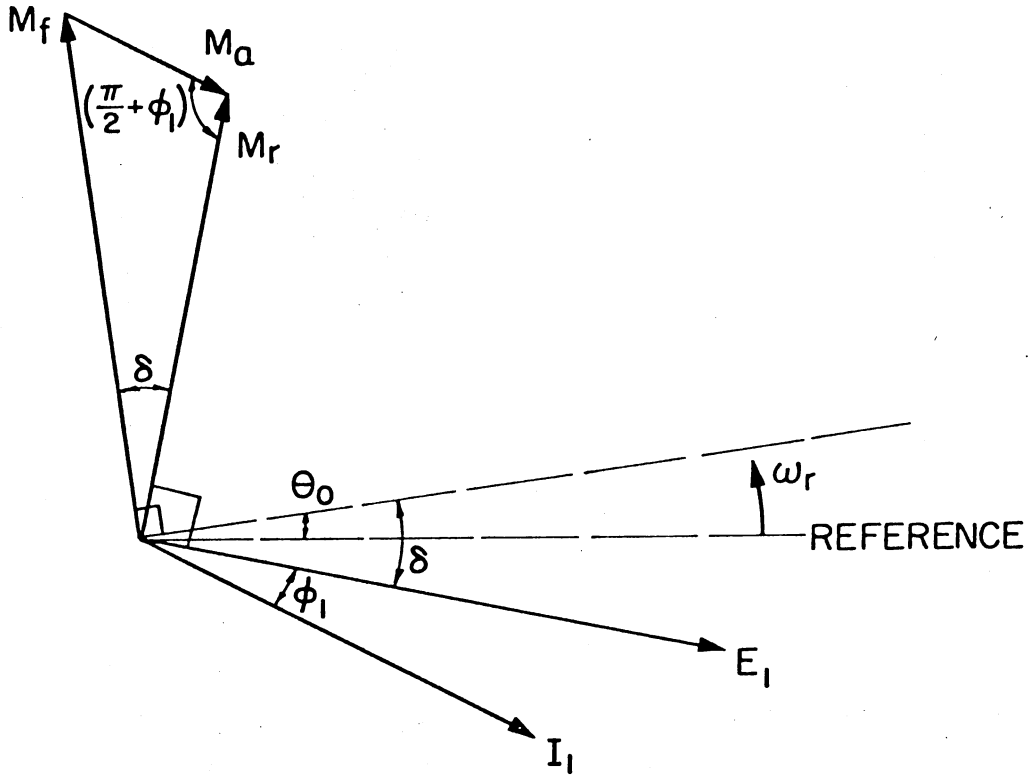

Figure 45. Illustrating Phase Relationships Between Fundamental Quantities for the Idealized Field Modulated Alternator

For concentrated full pitch coils, the expression for M_a in terms of the fundamental component becomes

$$M_a = \frac{3}{\pi} k_p k_d N_s I_1 \tag{3.4.25}$$

The power angle, δ, can be expressed as follows.

$$\delta = \cos^{-1} \left[\frac{M_r + M_a \sin \phi_1}{M_f} \right] \tag{3.4.26}$$

The mutual inductance between stator and rotor windings, M, can be found by utilizing the fact that when $i_a = 0$, $M_r = M_f$. Under this open-circuit condition, voltage induced in the stator phase winding must be due to M_f. Therefore,

$$E_1 \Big|_{i_a = 0} = \omega_r M I_r \tag{3.4.27}$$

$$= \mu_o M_f \omega_r \ell d N_s k_p k_d / g \tag{3.4.28}$$

Equating (3.4.27) and (3.4.28), and using the result in (3.4.2), the final expression for M becomes

$$M = \mu_o N_r k_f \ell d N_s k_p k_d / g \tag{3.4.29}$$

The effective inductance L_{re} of the rotor winding (namely net flux linking the rotor coil per ampere of rotor current) depends on the resultant MMF (and air-gap flux) and therefore depends on I_1, I_r, ϕ_1 and δ. From a review of coupled-circuit analysis concepts, it can be approximated as

$$L_{re} = L_r - \frac{3}{2} M \frac{I_1}{I_r} \sin(\phi_1 + \delta) \tag{3.4.30}$$

When $(\phi_1 + \delta)$ is zero, armature reaction flux wave is in space quadrature with the flux wave set up by the rotor current acting alone. Under the idealizing assumptions made in this study, the total flux

linking the rotor coil will then be the same with and without stator currents. This is equivalent to saying that L_{re} and L_r are equal if $(\phi_1 + \delta)$ is zero. Voltage applied to rotor terminals is given by

$$v_r = -V_r \sin \omega_m t \tag{3.4.31}$$

where

$$V_r = \omega_m L_{re} I_r \tag{3.4.32}$$

The current through rotor winding is

$$i_r = I_r \cos \omega_m t \tag{3.4.33}$$

The current through rotor tuning capacitor C_4 is

$$i_{cr} = -V_r \omega_m C_4 \cos \omega_m t \tag{3.4.34}$$

and the excitation current input to the system will then be

$$i_e = I_e \cos \omega_m t \tag{3.4.35}$$

where

$$I_e = I_r - V_r \omega_m C_4 \tag{3.4.36}$$

Expression for the torque developed will be of the form

$$T = k_t M_f M_r \sin \delta \tag{3.4.37}$$

where

$$k_t = -\mu_o \pi D \ell/(2g) \tag{3.4.38}$$

Analysis of different parts of the system can now be tied together as follows:

Step I. Knowing the output power, power factor, rated voltage and filter circuit parameters, obtain the effective impedance and voltage at the output terminals of the parallel-bridge rectifier system (PBRS).

Step II. From an analysis of the circuit shown in Figure 39, find the values of E_1, I_1 and ϕ_1.

Step III. Obtain M_r, M_a and M_f using equations (3.4.16), (3.4.24) and (3.4.23). Then equation (3.4.2) can be used to find I_r. Knowing L_{re} and C_4; V_r, i_{cr} and i_e can be calculated.

Combining Figures 42 and 45, high frequency (ω_r) vector diagram for the idealized FMGS model is obtained as shown in Figure 46. Maximum values of V_{a1} and V_ℓ are assumed to occur at the same instant of time as

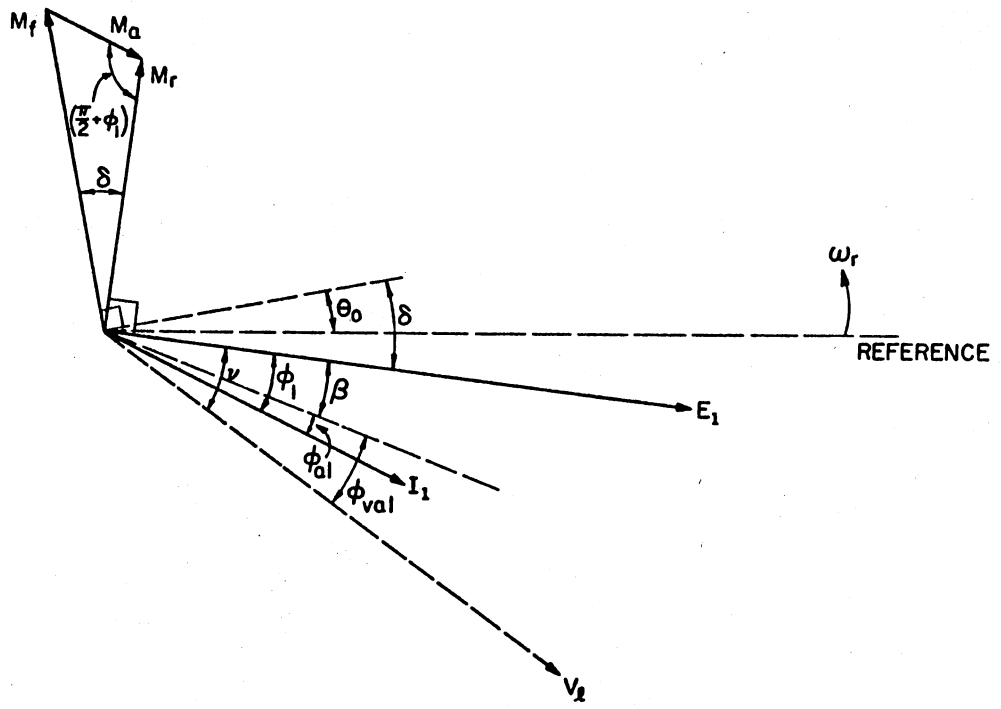

Figure 46. High Frequency (ω_r) Vector Diagram Illustrating Phase-Relationships Between Fundamental Quantities for the Idealized FMGS

discussed in Section 3.3. V_ℓ is shown as a dotted line only to indicate its angular position. Notice that reference axis is chosen to correspond to Figure 38.

Figure 47 shows the low frequency (ω_m) vector diagram for the FMGS. This vector diagram is obtained by aligning E_1 of Figure 43 to correspond to its position in Figure 46. Phase angles in Figure 46 are scaled down by the modulation frequency ratio 'm' and excitation currents and voltages are included.

The system performance equations and vector diagrams developed in this Section form a solid basis for further explorations on field modulated generator systems.

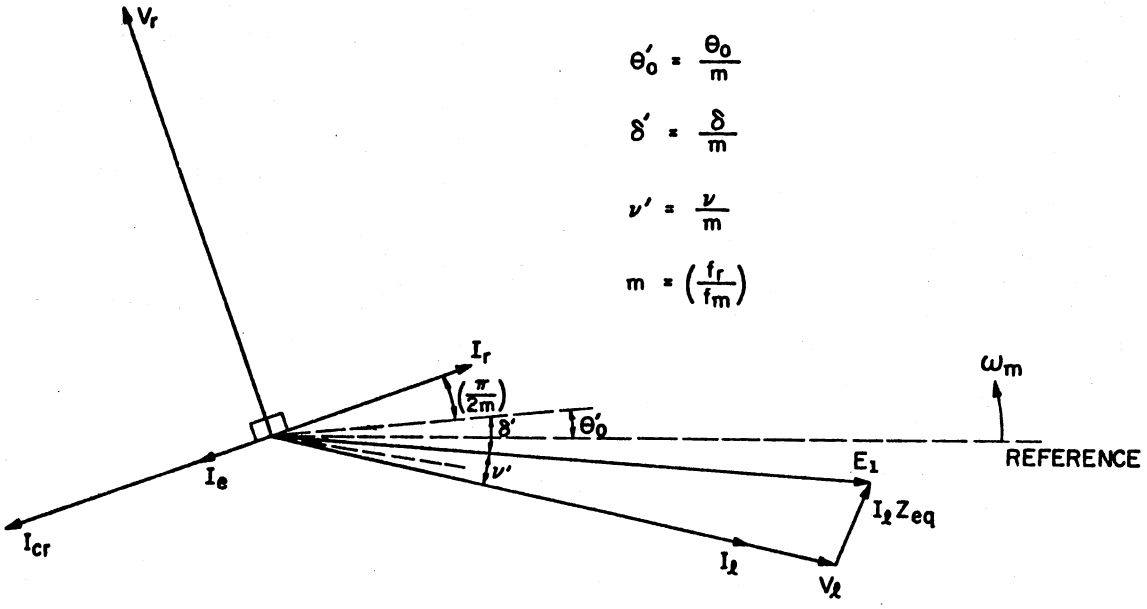

Figure 47. Low Frequency (ω_m) Vector Diagram Illustrating Phase-Relationships Between Fundamental Quantities for the Idealized FMGS

CHAPTER IV

EXPERIMENTAL INVESTIGATIONS

4.1 Introduction

The theoretical developments of idealized PBRS and FMGS models in Chapters II and III have been verified experimentally to assess the validity of the assumptions made in the analyses. The purpose of this Chapter is to present the results and discuss the three experimental investigations undertaken; namely a) operation of PBRS with capacitors at bridge-inputs and the effect of varying the capacitance and load resistance values over a wide range on various current and voltage waveforms and regulation characteristics for resistive load conditions; b) verifying the validity of PBRS model developed in Chapter II by comparing experimental and theoretical values of angles γ and β, and magnitudes of I_d and E_d; and c) checking the correctness of FMGS model developed in Chapter III by comparing theoretical and experimental values of certain input and output parameters [31].

For each experimental investigation, the laboratory setup and the testing method are described and recorded data (including oscillograms) are documented and their significances are discussed. Sample calculations to obtain theoretical results are presented where necessary.

Section 4.2 summarizes PBRS experiments and verification of waveform equations as well as the results of harmonic analysis presented in

Chapter II. Section 4.3 deals with experiments conducted to verify the validity of FMGS model. The Chapter concludes with an overall discussion in Section 4.4 of all the experimental studies.

4.2 PBRS Studies

Idealized circuit model of PBRS with bridge-input capacitors under resistive load condition ($L_\ell = 0$) is shown in Figure 3 (Chapter II). Experimental studies related to PBRS are presented in several stages as follows.

(A) Experimental Setup for Studying the Operation of PBRS

Figure 48 shows the schematic of the experimental setup used in studying the operation of PBRS. Three identical single-phase transformers and three choke coils were used as shown to simulate a high-reactance three-phase power source. Each transformer had four identical windings. Two windings in parallel was used as the primary and the three primaries were connected in delta to the output of a three-phase variac. One winding was left open for measuring the ideal source voltage behind the source impedance. The fourth one was used as the secondary and the choke coil was connected in series with it. The equivalent impedance per phase of the source was experimentally determined to be (3.23 + j 46.63) ohms.

Three full-wave bridges were connected, one each across the three isolated terminals of the transformer secondary-choke combinations, and the three bridge outputs were tied in parallel across the variable load resistance. Three identical capacitors were connected across the three pairs of bridge-input terminals as shown. Proper shunts were installed

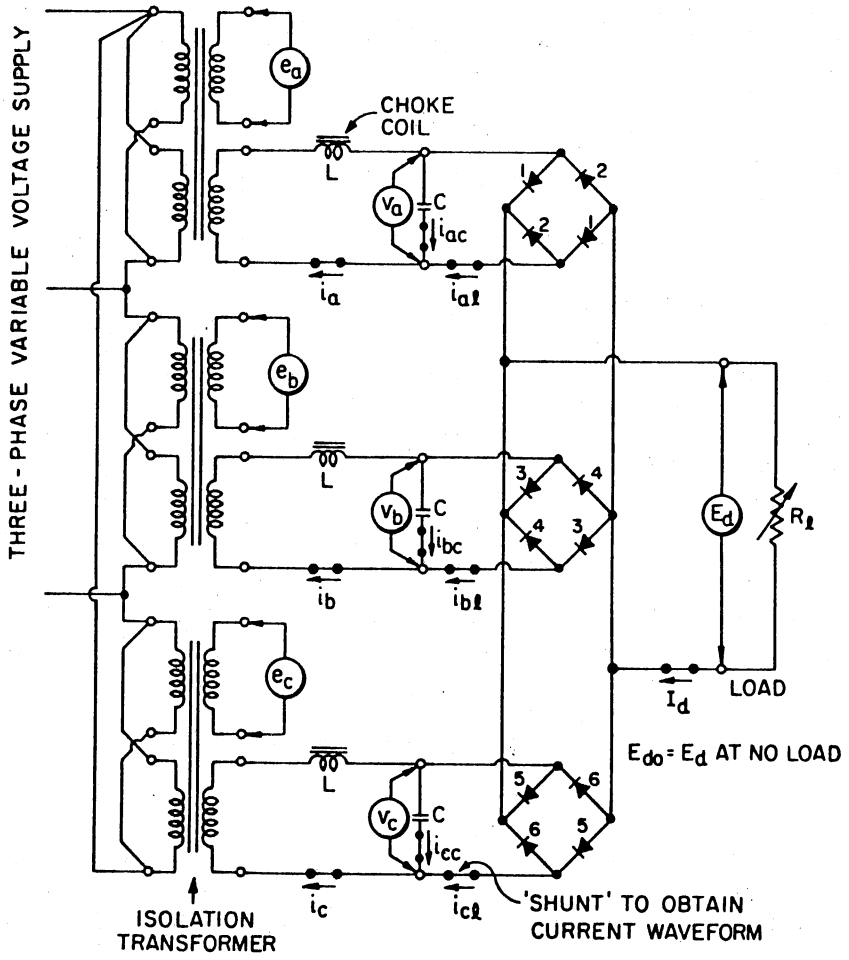

Figure 48. Experimental Setup for PBRS Studies

at various points in the circuit to observe and record current waveforms. A photograph of the experimental setup is shown in Figure 49.

The experimentation was conducted as follows. Four different trios of capacitors and six different load resistances were selected out of available hardware and corresponding to each capacitor trio, the load resistance was varied over a series of six different values. This allowed the investigation of four different (X_L/X_C) ratios - namely 0.04, 0.09, 0.43 and 0.80 - for each value of load resistance. Four oscillograms - (e_a,v_a), (i_a,v_a), $(i_{a\ell},v_a)$ and (i_{ac},v_a) - were taken for each of the twenty-four combinations of capacitance and resistance values. These, in addition to the oscillograms with no capacitors $(X_L/X_C = 0)$ form the bulk of the results presented. Regulation data was taken by varying the load resistance over the full range, from ∞ to 0, for each

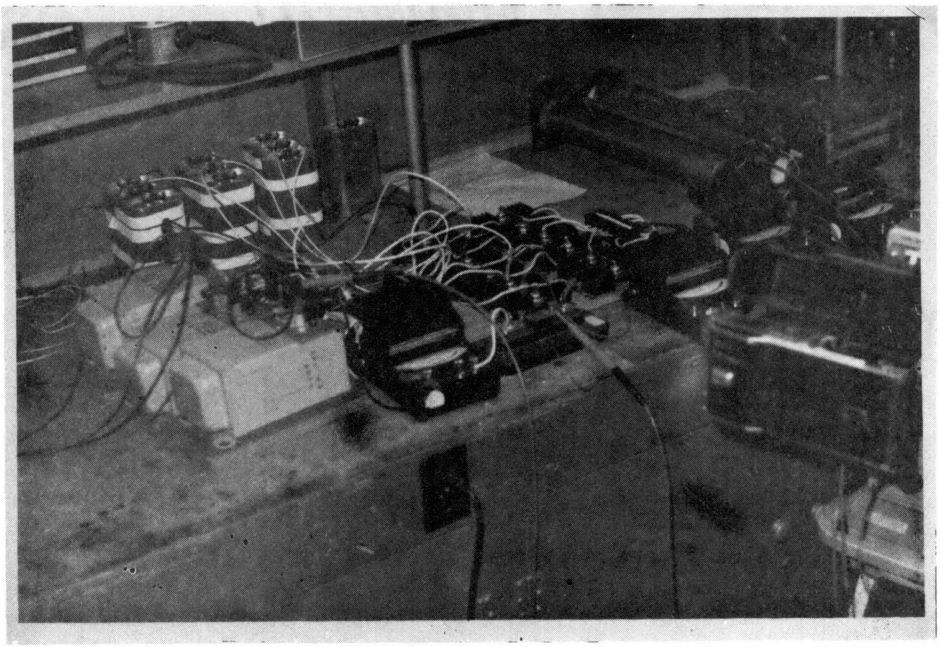

Figure 49. Photograph of the PBRS Experimental Setup

of the capacitance values.

(B) Experimental Results

Each of the oscillograms recorded during this experiment is identified by a notation consisting of two numbers followed by two symbols and three more numbers. As an example, consider the oscillogram identified as: $2.44/26.92/e_a,v_a/20,20/50$

The first number (2.44) denotes the capacitance in micro-farad (μF) across each of the bridge-inputs, the second number (26.92) denotes the value of the load resistance in ohms, the symbols e_a and v_a denotes the waveforms contained in the oscillogram, the next two numbers represent the vertical scales in A/cm and/or V/cm respectively as applicable, and the last number represents the RMS value of the per-phase source voltage. Obviously, for the case with no capacitors at bridge-inputs, the first number will be zero. The horizontal time scale is 2 ms/cm for all the oscillograms. The general nature of waveforms for phase-a, and waveforms of load current and bridge-input currents have been shown in Figures 5 and 4, Section 2.2 (Chapter II). Figures 50 through 53 present the majority of oscillograms taken. The oscillograms are arranged in such a way that each row corresponds to a fixed load resistance value and each column corresponds to a fixed capacitance value at the bridge-inputs. As one moves from left to right, the capacitance value increases. Load resistance values increase as one moves from top to bottom.

The effect of adding capacitors at bridge-inputs on the bridge-input voltage (v_a) can be seen, for example, by comparing the

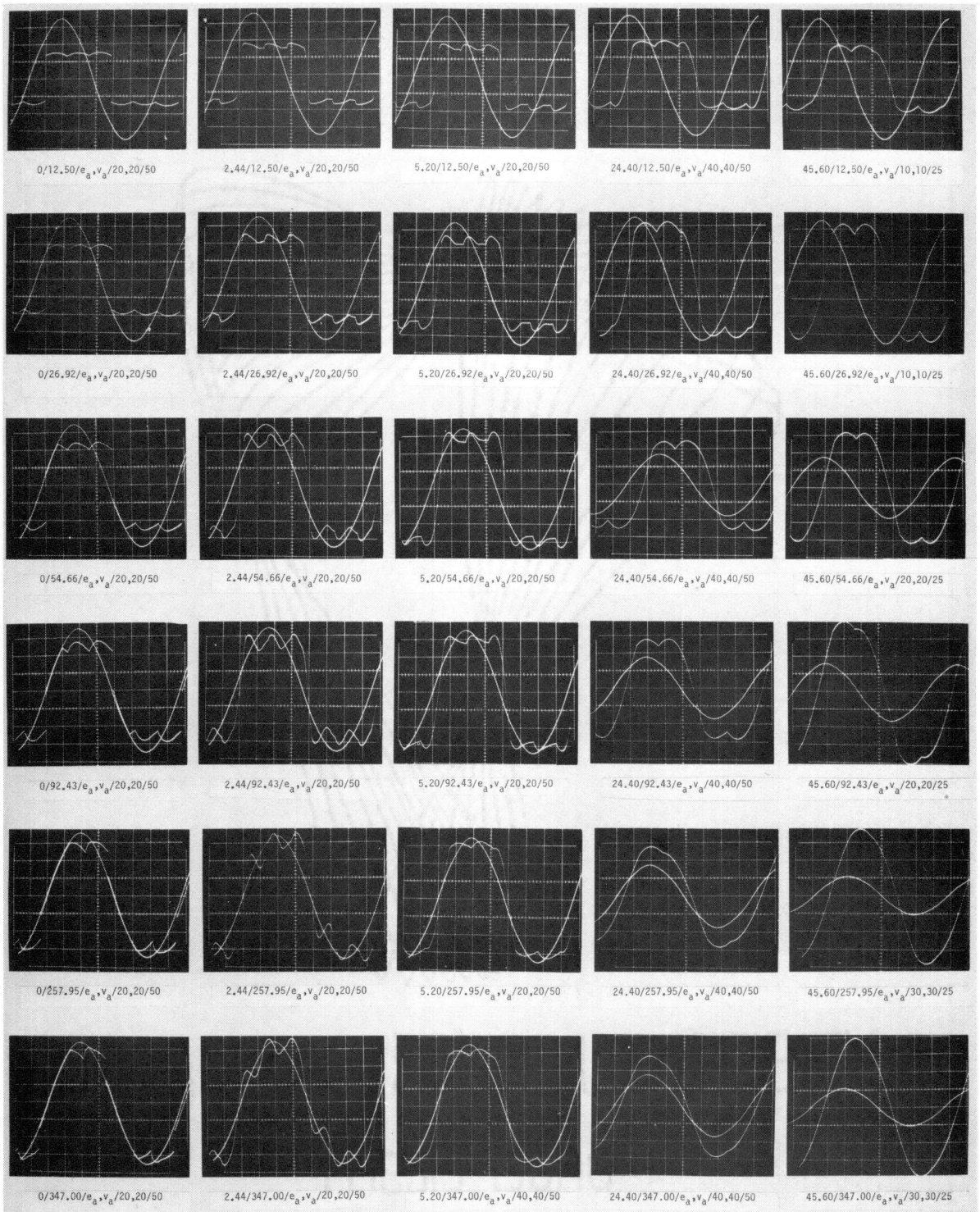

Figure 50. Oscillograms of e_a and v_a

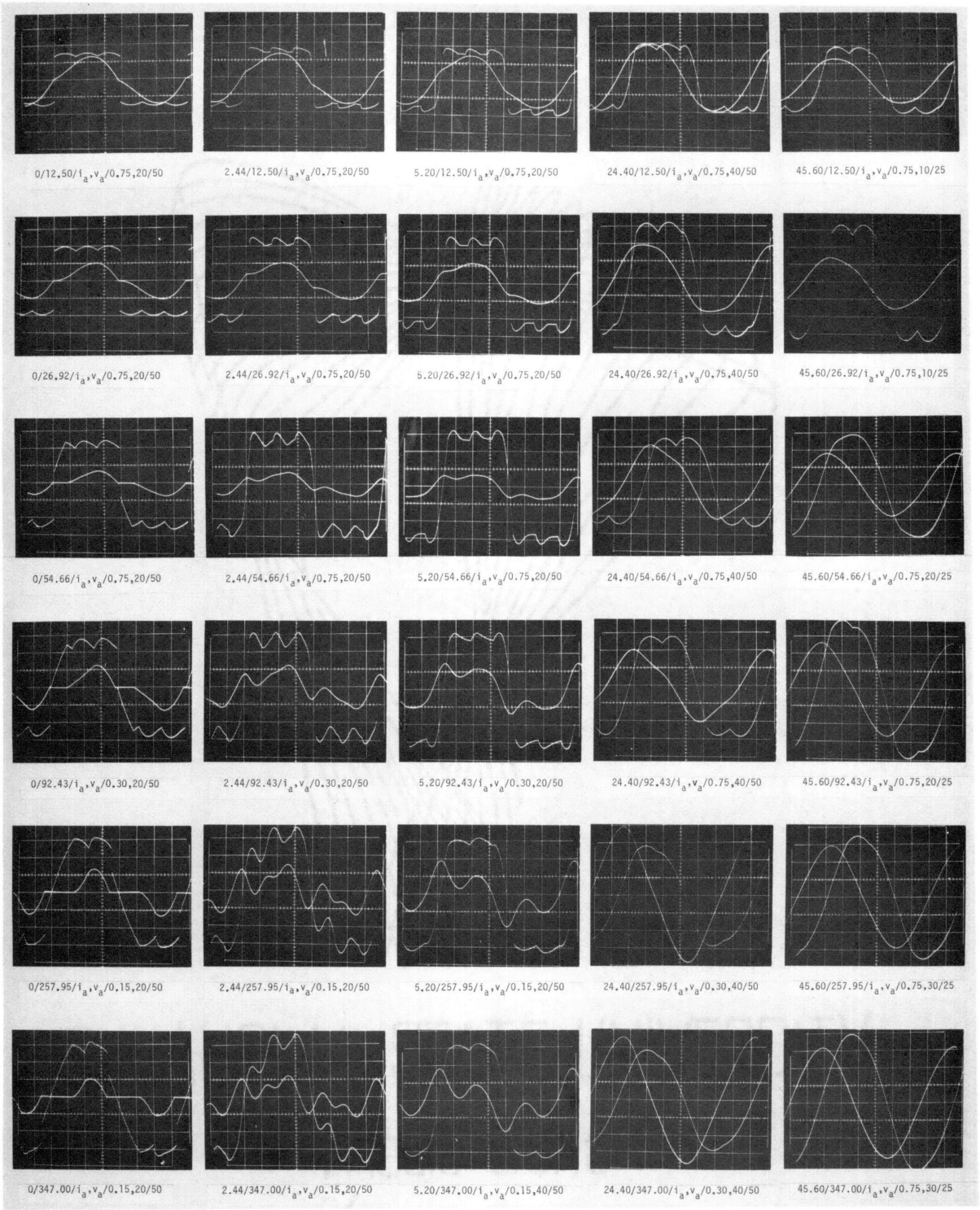

Figure 51. Oscillograms of i_a and v_a

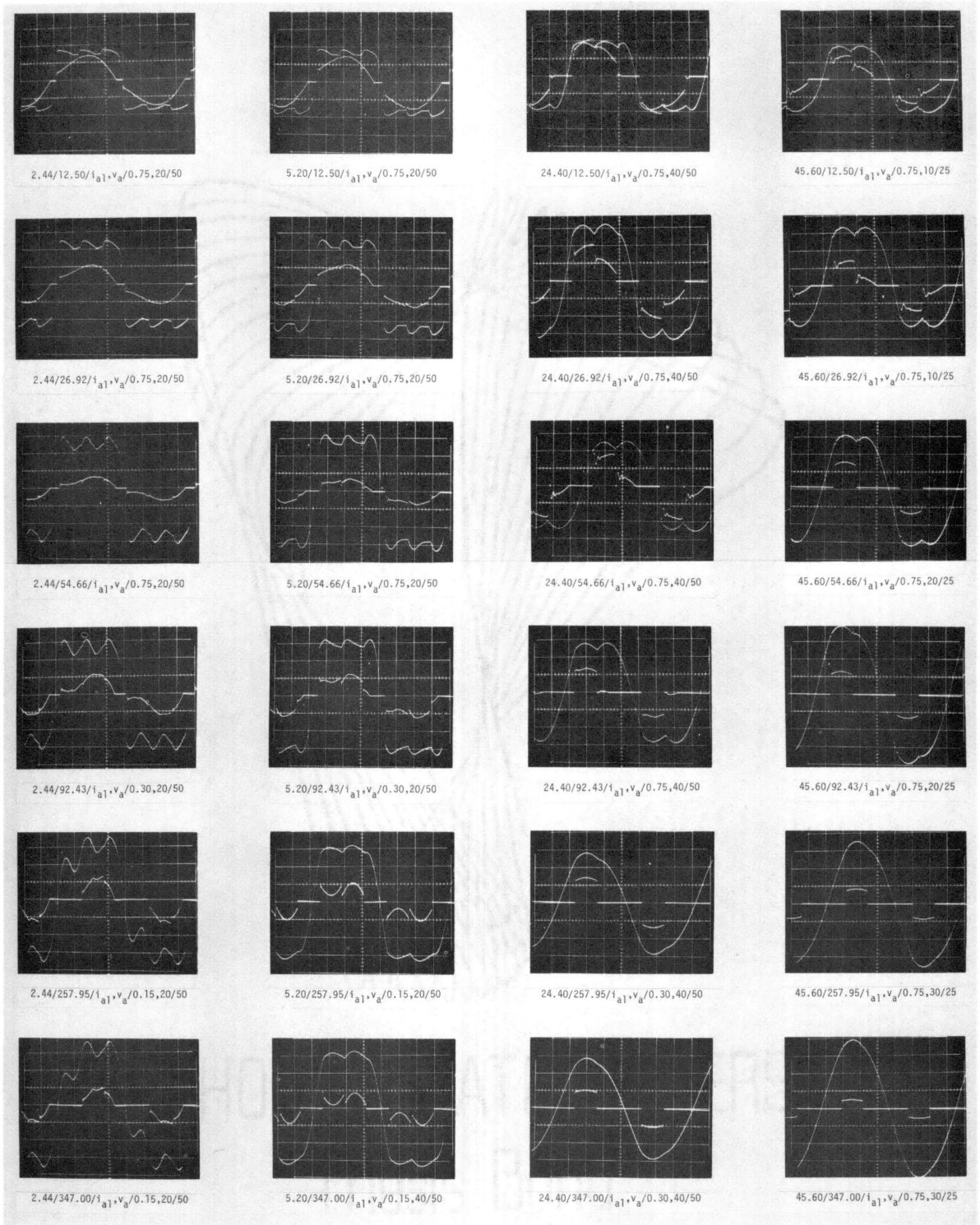

Figure 52. Oscillograms of $i_{a\ell}$ and v_a

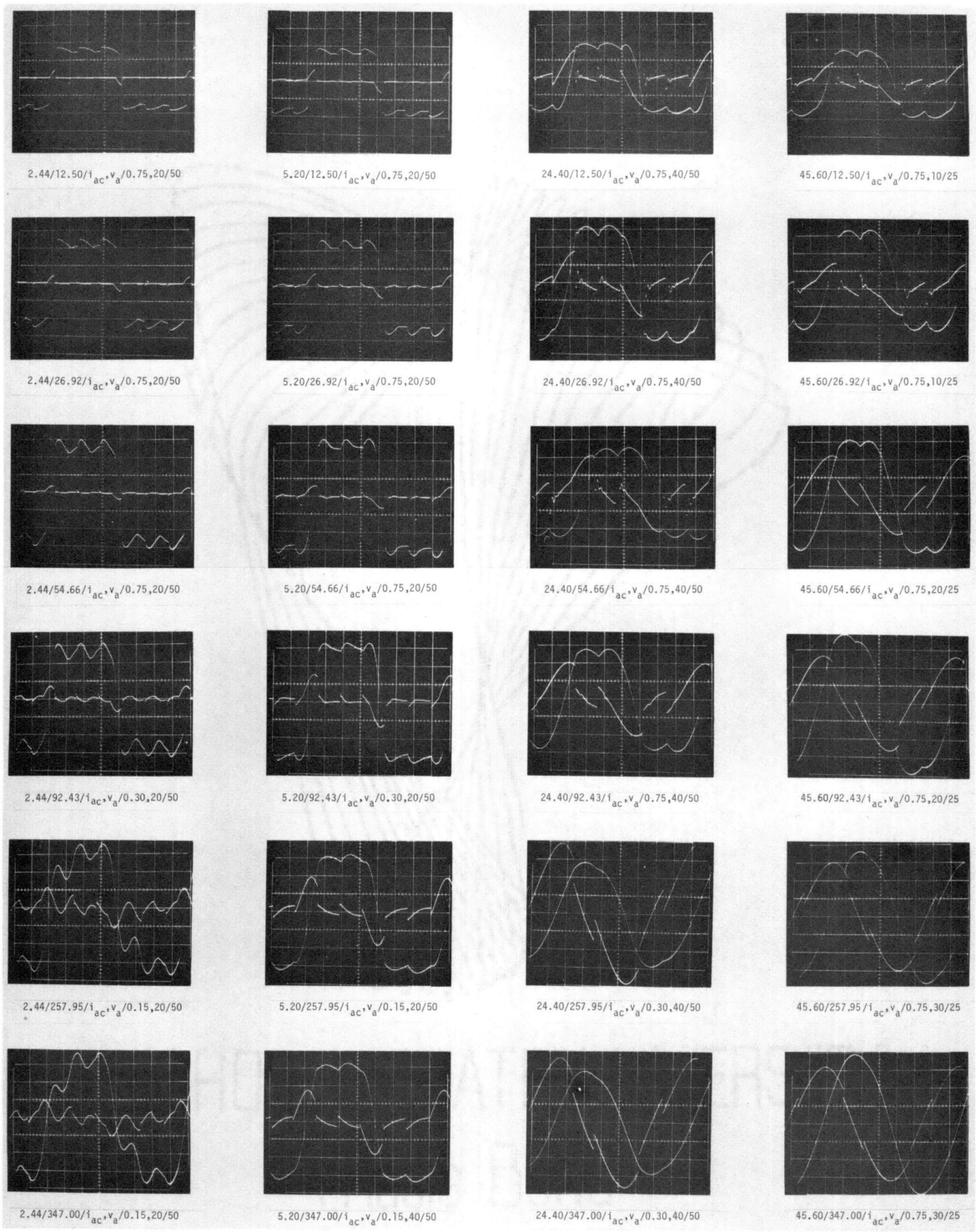

Figure 53. Oscillograms of i_{ac} and v_a

oscillograms 0/12.50/e_a,v_a/20,20/50 and 2.44/12.50/e_a,v_a/20,20/50 in Figure 50. With no capacitors, as long as $|e_a| \geq |v_a|$, conduction is transferred from diodes 2 to diodes 1 at the instant of switching. Similar transfers take place at other instances between different diode pairs in phases b and c. This results in a bridge-input voltage which is essentially a square wave, with a ripple made up of the middle third sections of the half cycles of sine waves. But, with capacitors present, when conduction in diodes 2 stops at $t = 0^-$, phase-a circuit gets decoupled from the other two phases. In other words, all four diodes of phase-a bridge are off, $i_{a\ell} = 0$, and $i_a = i_{ac} = i_{al}$. This state of affairs continues until $t = (\gamma/\omega)$. During this period, phase-a circuit exhibits oscillatory behavior with initial conditions being $v_a = -V_o$ and $i_a = I_o$ (refer Figure 5, Section 2.2). At $t = (\gamma/\omega)$, diodes 1 starts to conduct. Rererring back to Figure 5, sections of v_a marked v_{a3} and v_{a5} are formed by the decoupling of phases c and b respectively from the other two phases. During the time periods corresponding to sections marked v_{a2}, v_{a4} and v_{a6}, all three bridges are simultaneously conducting.

Studying the top row of oscillograms in Figure 50 from left to right, it can be seen that the decoupling duration (γ/ω) increases with increasing capacitance values and eventually becomes equal to $(\pi/3\omega)$. Under such circumstances, only two of the three bridges conduct at any one time. If, in addition, the load resistance is also increased, the bridge-input voltage tends to become a sine wave and at any instant of time only one bridge will be conducting (γ becomes equal to $2\pi/3$). Each bridge will then be on for only one third of the period. This process can be visualized by observing the last column of oscillograms in Figure

50 from top to bottom.

Figure 51 illustrates the influence of bridge-input capacitors on the source current. The provision of an added path through the capacitor for current flow contributes to the formation of an additional crest (during $0 \leq t \leq \gamma/\omega$) in the current waveform. The height of this crest increases with increasing capacitance and with increasing load resistance (refer oscillograms $0/12.50/i_a,v_a/0.75,20/50$ with $2.44/12.50/i_a,v_a/0.75,20/50$; $2.44/92.43/i_a,v_a/0.30,20/50$ and $24.40/92.43/i_a,v_a/0.75,40/50$ in Figure 51).

Moreover, zero crossings of the source current do not coincide with the switching instances of corresponding diodes as is the case with no capacitors. Increasing the capacitance (with or without increasing the load resistance) tends to make the source current to be nearly sinusoidal. This can be seen by studying the last column of oscillograms in Figure 51.

Bridge-input current waveforms shown in Figure 52 clearly illustrate the influence of capacitors on the 'on' and 'off' periods of the diode bridges. Earlier statements regarding conduction periods of the bridges are reinforced by these oscillograms.

Comparison of $0/257.95/e_a,v_a/20,20/50$ and $0/257.95/i_a,v_a/0.15,20/50$ with $2.44/257.95/e_a,v_a/20,20/50$ and $2.44/257.95/i_{a\ell},v_a/0.15,20/50$ brings up a significant point in the behavior of the parallel-bridge rectifier system with capacitors at bridge-inputs. With no capacitors, the bridge-input voltage coincides with the source voltage whenever that particular bridge is not conducting. This is not necessarily true when capacitors are present. During the oscillatory behavior ($0 \leq t \leq \gamma/\omega$), when the bridge is completely off, the bridge-input voltage can go above

or below the source voltage.

Capacitor current and capacitor voltage (which is the same as bridge-input voltage) waveforms are shown in Figure 53 for the range of capacitance and load resistance values investigated. Obviously, at any instant of time, the following two relationships must be satisfied for phase-a:

$$i_{ac} = C \frac{dv_a}{dt}$$

$$i_a = i_{a\ell} + i_{ac}$$

As the capacitance and/or load resistance increases, significant capacitor current flow results. These currents are highly non-sinusoidal. The advantages of using capacitors must be carefully balanced against the additional losses that are bound to occur in the source due to the flow of these currents.

The angle β (refer Figure 5, Section 2.2) changes with load resistance as well as with capacitance values. In general, it decreases with an increase in load resistance (compare oscillograms 2.44/12.50/e_a,v_a/20 ,20/50 with 2.44/347.00/e_a,v_a/20,20/50) and increases with an increase in the capacitance value. The latter is evident from an examination of any row of oscillograms in Figure 50.

Experimental regulation data is presented in Table I. This data is plotted in normalized form in Figure 54. It is seen that the curves for different (X_L/X_C) ratios intersect over the full range of load resistance values, extending from ∞ to 0. In general, the use of capacitors at bridge-inputs improves the regulation. However, continued increase of capacitance value eventually leads to poor regulation and may even make it worse than the regulation for the case with no capacitors. It

TABLE I

EXPERIMENTAL DATA FOR PBRS REGULATION CURVES

Source Voltage Maintained at 50 V rms per phase for C = 0, 2.43, 5.20, 12.20, and 24.40; 25 V rms per phase for C = 45.60
ωL = 46.63 Ω

C (μF) \ R_1 (Ω)		12.50	26.92	54.66	75.00	92.43	150.00	200.00	257.95	347.00
0	I_d(A)	2.19	1.41	0.82	0.63	0.53	0.35	0.27	0.21	0.17
	$\frac{46.63}{50} I_d$	2.042	1.315	0.764	0.587	0.493	0.326	0.249	0.200	0.154
	E_d(V)	27.20	36.60	44.60	47.80	49.70	52.70	54.10	56.70	58.80
	$\frac{E_d}{E_{do}}$	0.407	0.548	0.668	0.716	0.744	0.789	0.810	0.849	0.880
2.43	I_d(A)	2.38	1.67	0.92	0.67	0.56	0.35	0.29	0.23	0.17
	$\frac{46.63}{50} I_d$	2.215	1.554	0.854	0.628	0.518	0.325	0.267	0.213	0.160
	E_d(V)	30.30	42.90	50.30	50.75	52.20	52.60	57.65	59.60	61.35
	$\frac{E_d}{E_{do}}$	0.433	0.613	0.719	0.725	0.746	0.751	0.824	0.851	0.876
5.20	I_d(A)	2.45	1.83	1.05	0.77	0.63	0.40	0.30	0.23	0.17
	$\frac{46.63}{50} I_d$	2.280	1.710	0.981	0.722	0.586	0.372	0.278	0.215	0.157
	E_d(V)	32.30	47.15	57.15	58.40	58.80	59.60	60.00	60.15	60.40
	$\frac{E_d}{E_{do}}$	0.450	0.657	0.796	0.813	0.819	0.830	0.836	0.838	0.841
12.20	I_d(A)	2.67	2.22	1.25	0.95	0.78	0.49	0.37	0.28	0.22
	$\frac{46.63}{50} I_d$	2.486	2.069	1.168	0.884	0.723	0.459	0.347	0.265	0.203
	E_d(V)	35.30	55.20	68.35	70.40	71.90	74.10	74.70	75.10	76.40
	$\frac{E_d}{E_{do}}$	0.425	0.664	0.822	0.847	0.865	0.891	0.898	0.903	0.919
24.40	I_d(A)	2.69	2.37	1.69	1.36	1.12	0.71	0.54	0.42	0.32
	$\frac{46.63}{50} I_d$	2.510	2.214	1.578	1.266	1.046	0.665	0.504	0.395	0.295
	E_d(V)	36.00	63.50	92.25	102.00	104.20	107.90	109.40	110.01	110.50
	$\frac{E_d}{E_{do}}$	0.319	0.562	0.816	0.903	0.922	0.955	0.968	0.974	0.978
45.60	I_d(A)	1.42	1.33	1.20	1.07	0.98	0.74	0.60	0.49	0.39
	$\frac{46.63}{25} I_d$	2.649	2.481	2.238	1.996	1.828	1.380	1.110	0.918	0.733
	E_d(V)	17.50	34.25	65.40	80.75	91.20	112.80	121.70	128.50	136.20
	$\frac{E_d}{E_{do}}$	0.112	0.220	0.419	0.518	0.585	0.723	0.780	0.824	0.873

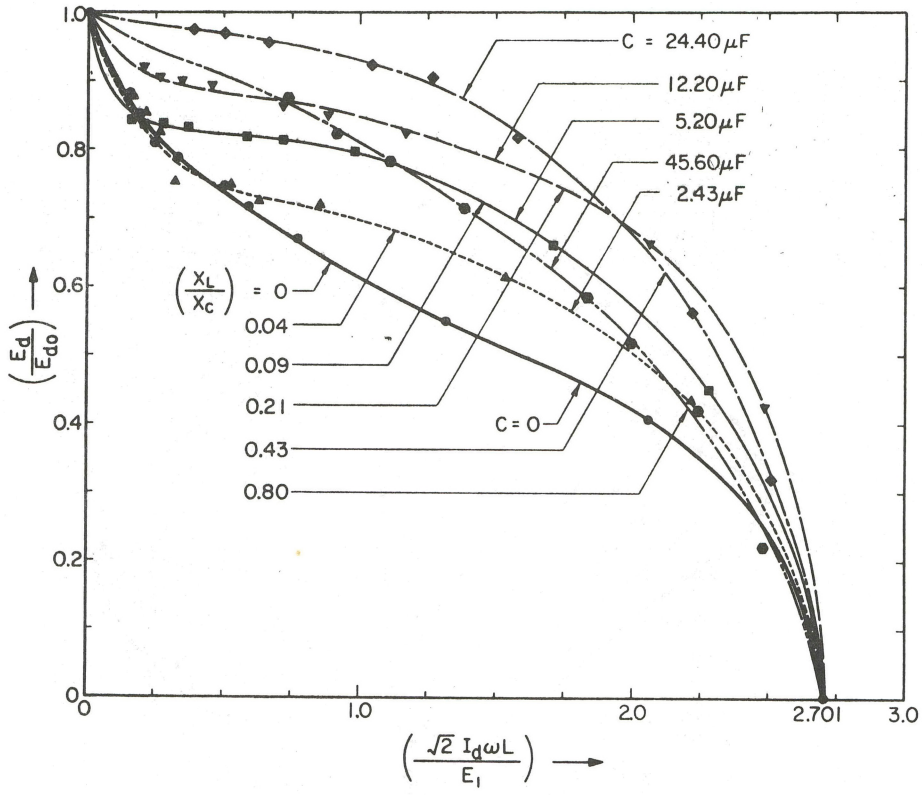

Figure 54. Experimental PBRS Regulation Curves (Normalized)

is also clear that for a set of specified load conditions, there is an optimum capacitance value that gives the best performance in terms of regulation.

Primary conclusions drawn from this part of the experimental study are: a) both the load resistances and the (X_L/X_C) ratio play vital roles in determining the 'on' and 'off' durations of the bridges; b) the transfer conduction from one diode pair to the other of any one bridge is associated with decoupling of that bridge from the other two for a duration denoted as (γ/ω) (refer Figures 4 & 5, Section 2.2);

c) during the period a bridge is decoupled from the other two, the series circuit consisting of the source, its commutating inductance L and the bridge-input capacitor C, exhibits oscillatory behavior and the bridge-input voltage swings both above and below the source voltage; such will be the case for light load (large R_ℓ) conditions and/or for large value of capacitance; d) as the capacitance (and/or load resistance) increases, eventually, each bridge conducts for only one third of the period (of the sinusoidal source) and is decoupled from the other two bridges the rest of the time. This process is also associated with the bridge-input voltage and capacitor current becoming nearly sinusoidal; e) for small values of (X_L/X_C) ratio (around 0.04), the angle β (refer Figure 5, Section 2.2) measured from the oscillograms is slightly smaller than $\tan^{-1}(\frac{\omega L}{3R_\ell})$, the value derived for the case with no capacitors and it decreases with an increase in R_ℓ and increases with an increase in C; and f) the regulation study demonstrates the fact that for any specified load conditions, there is an optimum value of the ratio (X_L/X_C) that results in best regulation.

These conclusions are in accordance with the theoretical analysis presented in Chapter II. In addition, the data recorded during this experiment can be used to compare theoretical values of certain parameters with experimental values to verify the validity of PBRS model as shown below.

(C) Verification of PBRS Model

Two checks were made to verify the validity of PBRS model developed in Chapter II. The first one used the values of angles γ and β measured

from oscillograms for four data points which fall within the region $(X_L X_C / R_\ell^2) > 36$. Correlation between theoretical and experimental values is illustrated in Figure 55. Maximum deviations in the values of γ and β are 9.8 and 17.9 per cent, respectively. In addition, employing the waveform equations derived and theoretical coefficients, k_1, k_2, k_5 and k_6 computed in Chapter II, several waveforms were plotted (not shown in the thesis) using Continuous System Modeling Program (CSMP) on an IBM-360 computer. The waveforms agreed fairly well with the oscillograms.

The second check applied equation (3.3.4) to compute theoretical values of I_d for the five data points. Since I_d is equal to $I_{\ell o}$ for this case, theoretical values of $K_{\ell o}$ as given in Figure 13 can be used.

Table II compares theoretical and experimental values of I_d and E_d. Maximum deviations are less than 6.79 and 9.67 per cent, respectively. Theoretical E_d is computed using I_d and known values of R_ℓ.

4.3 FMGS Studies

The idealized FMGS model developed in Chapter III is verified experimentally by following the steps outlined below.

(A) Approach for Experimental Studies

As a first step, theoretical values of excitation parameters (rotor applied voltage and current) were calculated for assumed (resistive) load conditions and compared with experimental values. Calculation of these theoretical values uses the results of several steps in the analysis of FMGS (refer Section 3.4, Chapter III). As such, it was felt that such a verification would lead to better understanding and confidence in the assumptions made in building the idealized model.

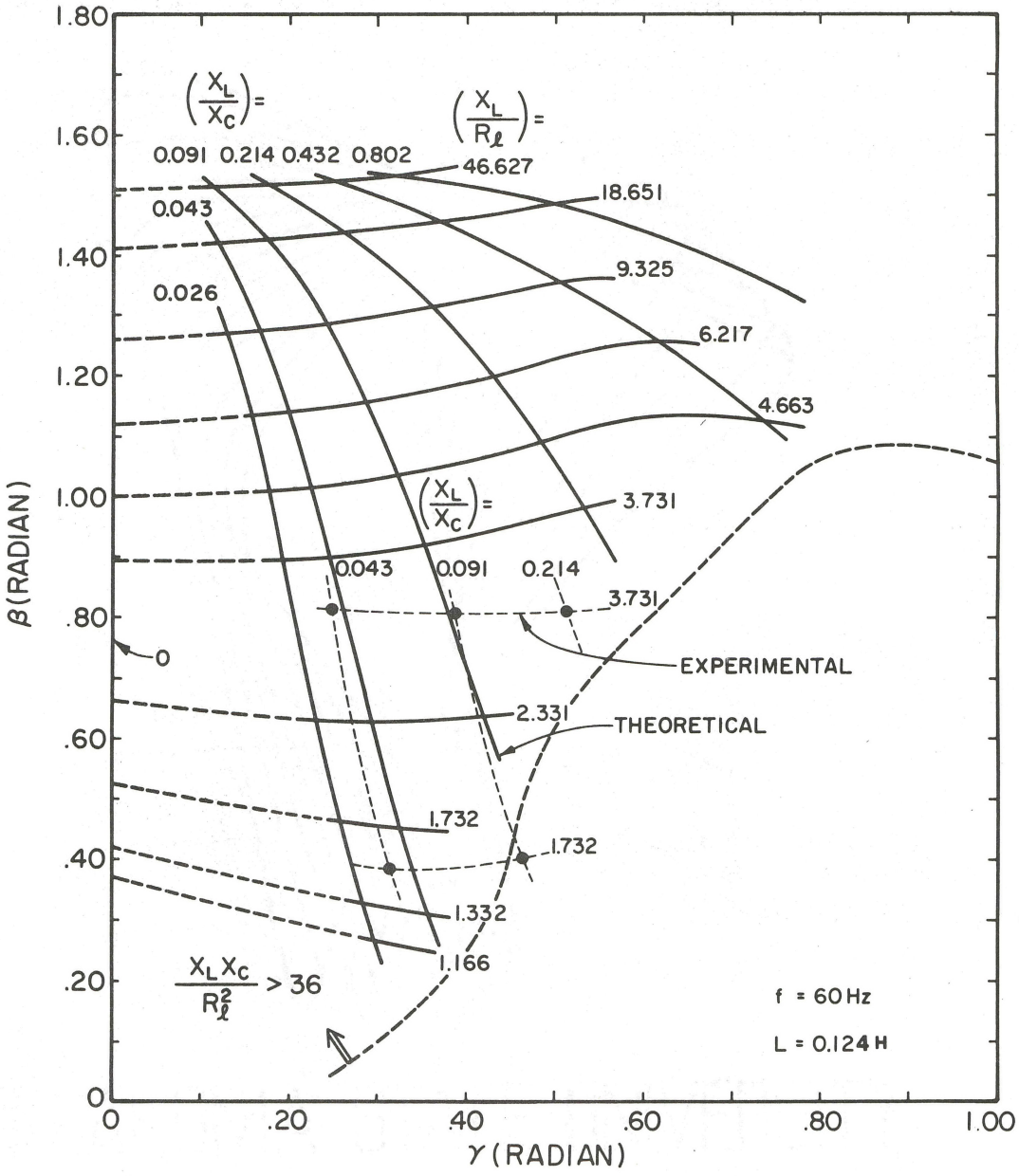

Figure 55. Comparison of Theoretical and Experimental Values of γ and β

TABLE II

THEORETICAL & EXPERIMENTAL VALUES OF I_d, E_d FOR PBRS

$X_L(\Omega)$	46.63				
$C(\mu F)$	2.44	5.20	12.20	2.44	5.20
$R_\ell(\Omega)$	—12.49 —			—26.92 —	
X_L/R_ℓ	— 3.73 —			— 1.73 —	
X_L/X_C	0.0428	0.0914	0.2140	0.0428	0.0914
$K_{\ell o}$	1.648	1.722	1.853	1.138	1.269
E_1(V, 0-peak)	——————70.72——————				
Theoretical I_d(A,dc)	2.50	2.61	2.81	1.73	1.92
Experimental I_d(A,dc)	2.38	2.45	2.67	1.67	1.83
Deviation in I_d(%)	+5.22	+6.79	+5.40	+3.60	+4.74
Theoretical E_d(V,dc)	31.23	32.63	35.12	46.46	51.71
Experimental E_d(V,dc)	31.30	32.30	35.30	42.90	47.15
Deviation in E_d(%)	-2.24	+1.02	-5.10	+8.30	+9.67

Excitation voltage and current are at modulation frequency (60 Hz for the test) and are sinusoidal. Output of FMGS is also at the same frequency. Output of the parallel-bridge rectifier system (which is the same as input to switching circuit constituted by thyristors SCR1 through SCR4; see Figure 2) is very nearly a fullwave rectified sine wave at modulation frequency with some harmonics (lowest order being at six times the basic machine frequency) superimposed. Since the idealized model assumes ideal solid-state switching and filtering, it is logical to perform the load test by connecting the load across output terminals of the PBRS and eliminate the switching and filtering components of the system. Measurement of 60 Hz rotor input and fullwave rectified sinusoidal PBRS output currents and voltages can be done fairly accurately using the instrumentation normally available. For these reasons, all experiments were performed by using power line to modulate the field and loading the system at the output terminals of the parallel-bridge rectifier system.

(B) Experimental Setup

Figure 56 shows the schematic of experimental setup used to conduct the investigations. A 20 kVA, 120/208 V, three-phase, 16-pole, 7200 r/min alternator was belt driven by a 30 hp induction motor, resulting in a basic alternator frequency in the range of 850 to 960 Hz. With field modulation at 60 Hz, the frequency ratio is at least 14, well above the minimum value of 10 assumed in the idealized model. A 36-turn full-pitch search coil was located in the stator slots to observe the voltage induced in the stator windings. Figure 57 shows views of the laboratory setup.

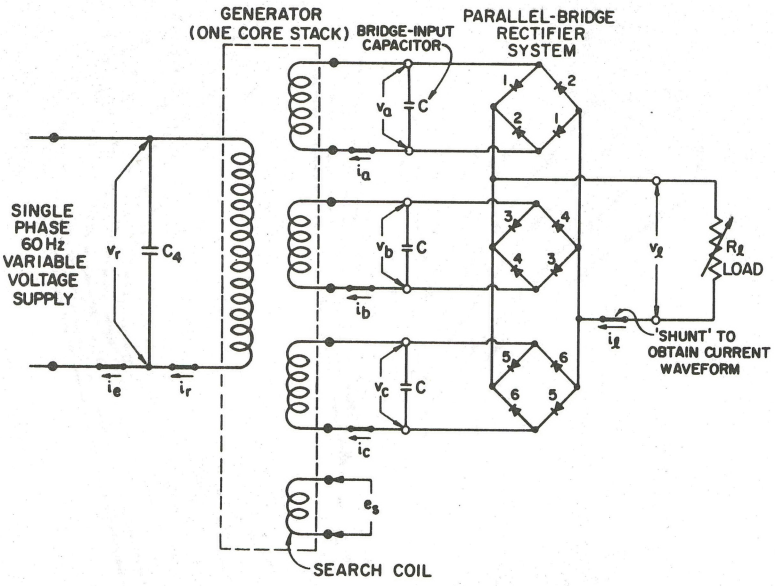

Figure 56. Schematic of the FMGS Experimental Setup

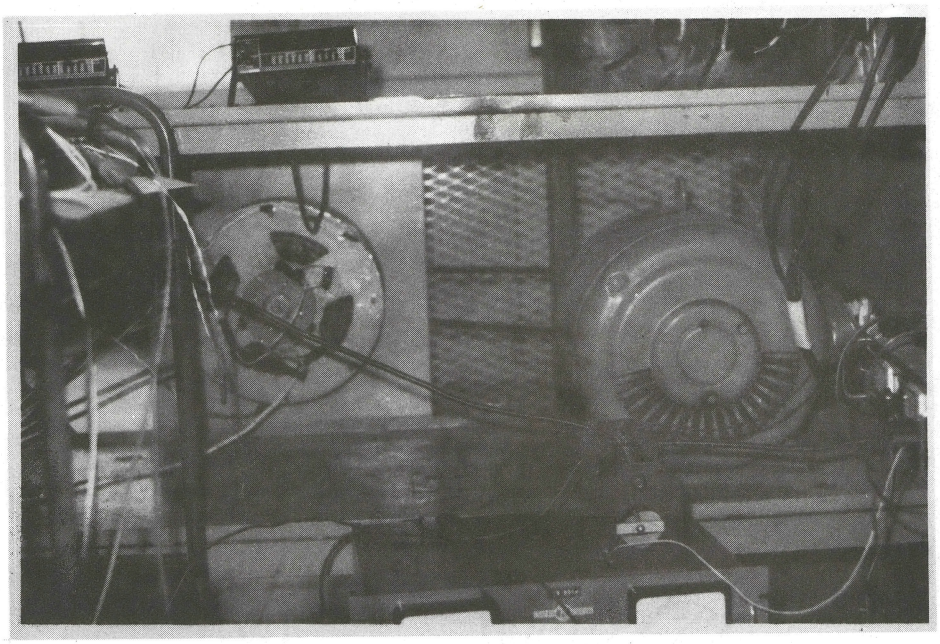

a. 20 kVA Alternator (Left) Driven by a
30 hp Induction Motor (Right)

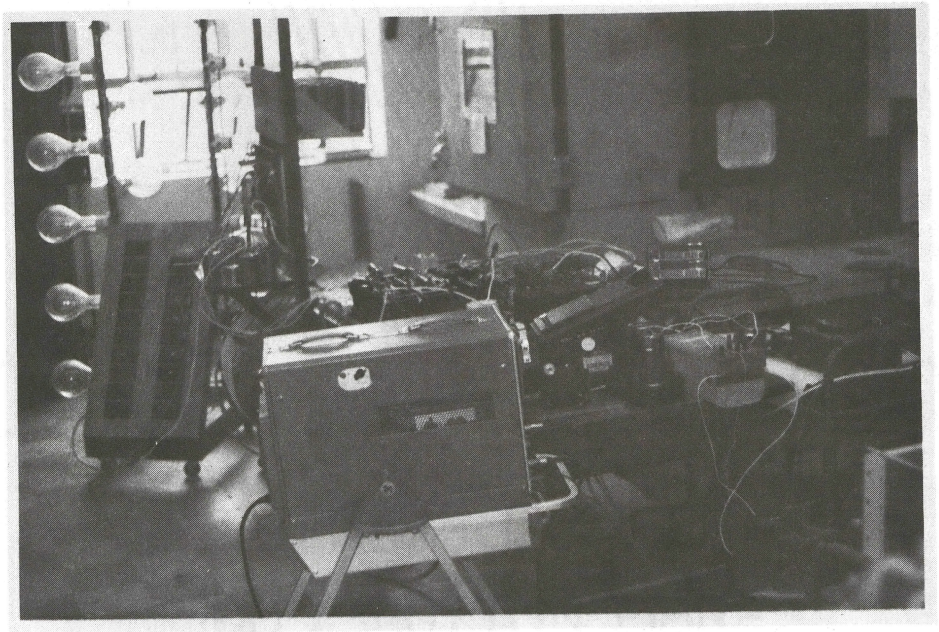

b. Instrumentation Setup

Figure 57. View of the FMGS Experimental Setup

(C) Experimental Procedure

No-load saturation and short-circuit characteristics were obtained using standard procedures and ac excitation (field modulation). Commutating inductance per phase of the alternator was experimentally obtained by the method suggested in Reference 22 and was found to be 0.327 mH. Rotor winding inductance was measured (using a 60 Hz power source) to be 0.184 H.

Physical data of the experimental alternator are summarized below.

Diameter at mean air-gap	$d = 0.22480$ m.
Active iron length	$\ell = 0.03810$ m.
Radial air-gap (sinusoidally shaped)	$g = 0.00151$ m, minimum.
No. of turns per phase in stator	$N_s = 64$
No. of turns per pole in rotor	$N_r = 120$
Full pitched stator coils	$k_p = 1$
One slot/pole/phase in stator	$k_d = 1$
No. of poles	$p = 16$
Rotor winding inductance (experimental value)	$L_r = 0.184$ H.
Stator commutating inductance/phase (experimental value)	$L = 0.327$ mH.

A lamp bank was used as load in the experiments. For a fixed value of bridge-input capacitance, the load was varied from 8 through 10 bulbs (each rated at 1500 W at 120 V) while maintaining the output at 80 volts dc (measured by a dc digital voltmeter). This allowed the examination of (X_L/R_ℓ) ratios from 1.696 to 2.102. For each combination of bridge-input capacitance and load resistance, oscillograms of various waveforms were taken and measurement of necessary data was performed. Three

values of bridge-input capacitors (3.00, 5.27 and 9.14 micro-farad) were used in the experiments.

(D) Experimental Results

Experimental no-load saturation and short-circuit characteristics of the test machine are shown in Figure 58 for ac excitation (field modulation at 60 Hz). Data is plotted in terms of zero-to-peak values for computational convenience.

Oscillograms of no-load waveforms are given in Figure 59 for two different values of dc excitation. Departures from sinusoidal waveshape are not drastic, considering the fact that stator coils are full pitched with only one slot per pole per phase.

Figure 60 shows oscillograms of v_r, i_r and e_a under no-load with field modulation. It is seen that v_r leads i_r by nearly 90 electrical degrees and i_r leads the envelope of e_a by a small angle.

Nine different load test runs were conducted and the data is summarized in Table III. The slight change in operating speed is due to slip in induction motor under load. Four sets of oscillograms corresponding to two different bridge-input capacitance values and two load resistance values are shown in Figures 61 through 64. The oscillograms are identified by the notation introduced in Section 4.2, with the last number now representing the horizontal time scale in ms/cm.

Numerical data for peak values of load voltage and current were read (values tabulated in Table III) from oscilloscope traces, corresponding to average ripple at peak of modulated envelope.

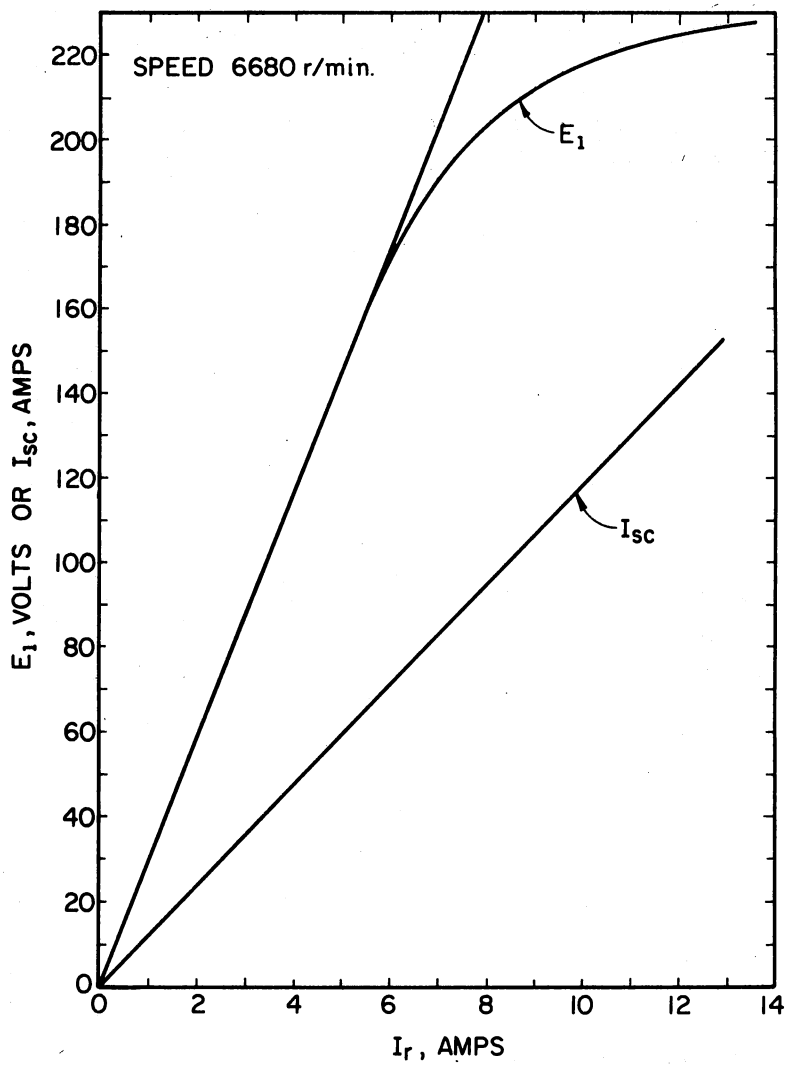

Figure 58. NO-Load Saturation and Short-Circuit Characteristics of the Test Machine With Modulation

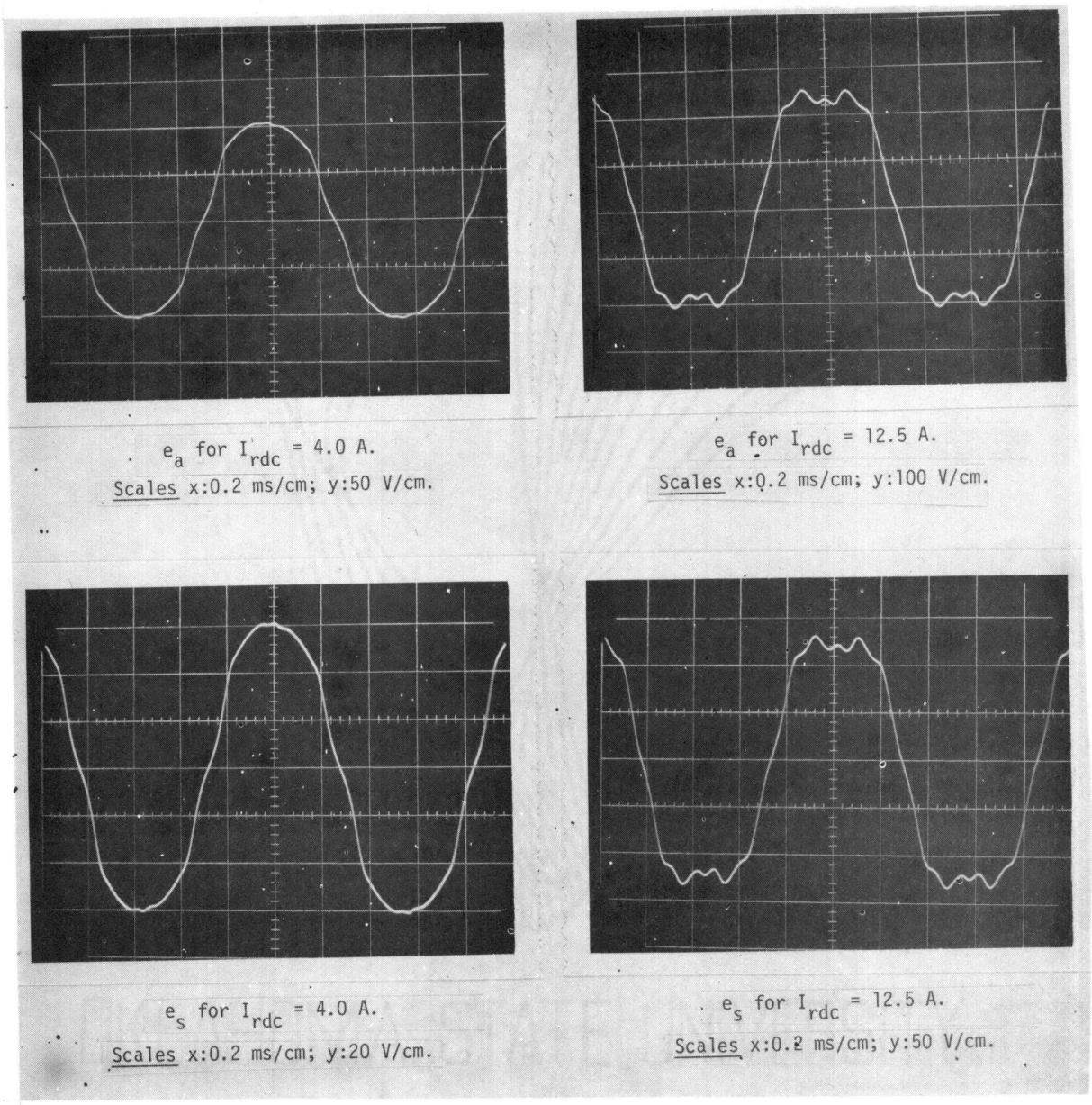

Figure 59. No-Load Waveforms Under dc Excitation

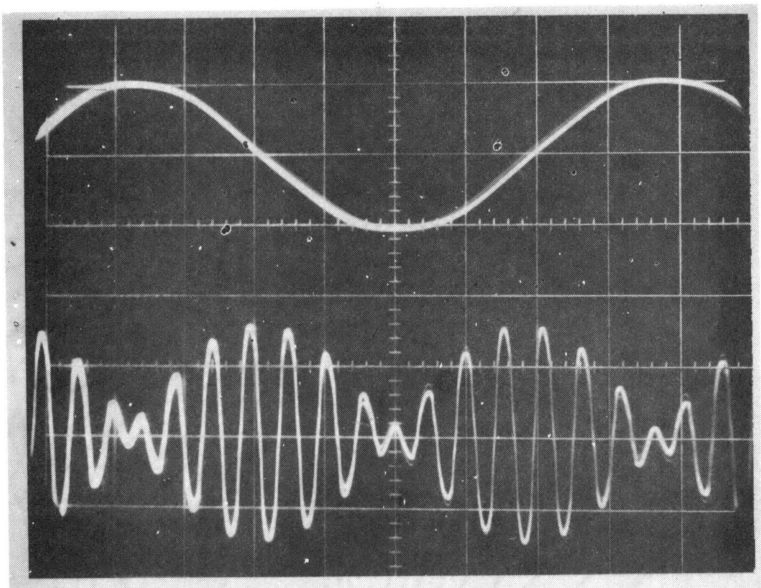

v_r; Scales x:2 ms/cm; y:100 V/cm.

e_a; Scales x:2 ms/cm; y:25 V/cm.

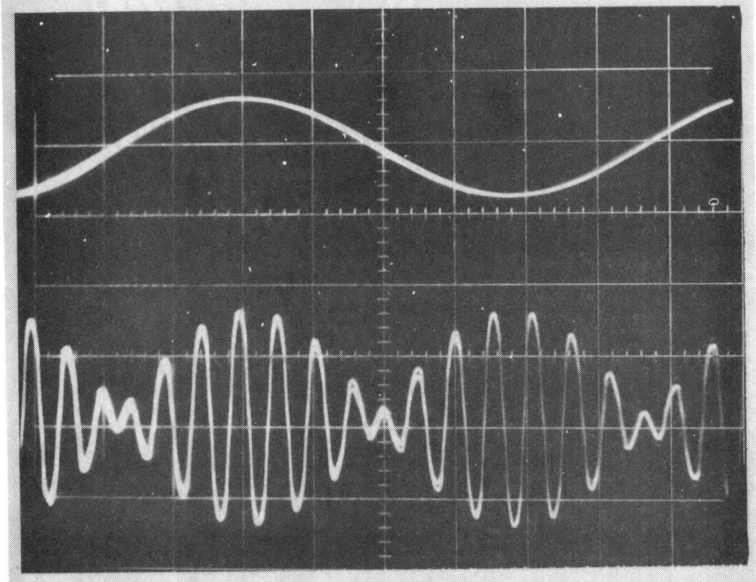

i_r; Scales x:2 ms/cm; y:2 A/cm.

e_a; Scales x:2 ms/cm; y:25 V/cm.

Figure 60. Oscillograms of v_r, i_r & e_a Under No-Load With Modulation

TABLE III

FMGS LOAD TEST DATA

C (μF)	3.00			5.27			9.14		
Nbr of Lamps in Parallel @1500W, 120V	8	9	10	8	9	10	8	9	10
I_g (A, 0-peak)	109.5	122.9	136.4	109.5	122.9	136.4	109.5	122.9	136.4
V_g (A, 0-peak)	116.8								
V_{rms} (V)	358.0	369.5	382.5	343.5	355.0	368.0	323.5	335.0	347.0
I_{rms} (A)	6.44	6.85	7.29	6.10	6.50	6.95	5.68	6.11	6.55
$I_{c\ rms}$ (A)	5.99	5.94	5.92	5.84	5.83	5.81	5.44	5.43	5.40
ω_r (rad/sec)	5526.	5511.	5497.	5526.	5511.	5497.	5526.	5511.	5497.

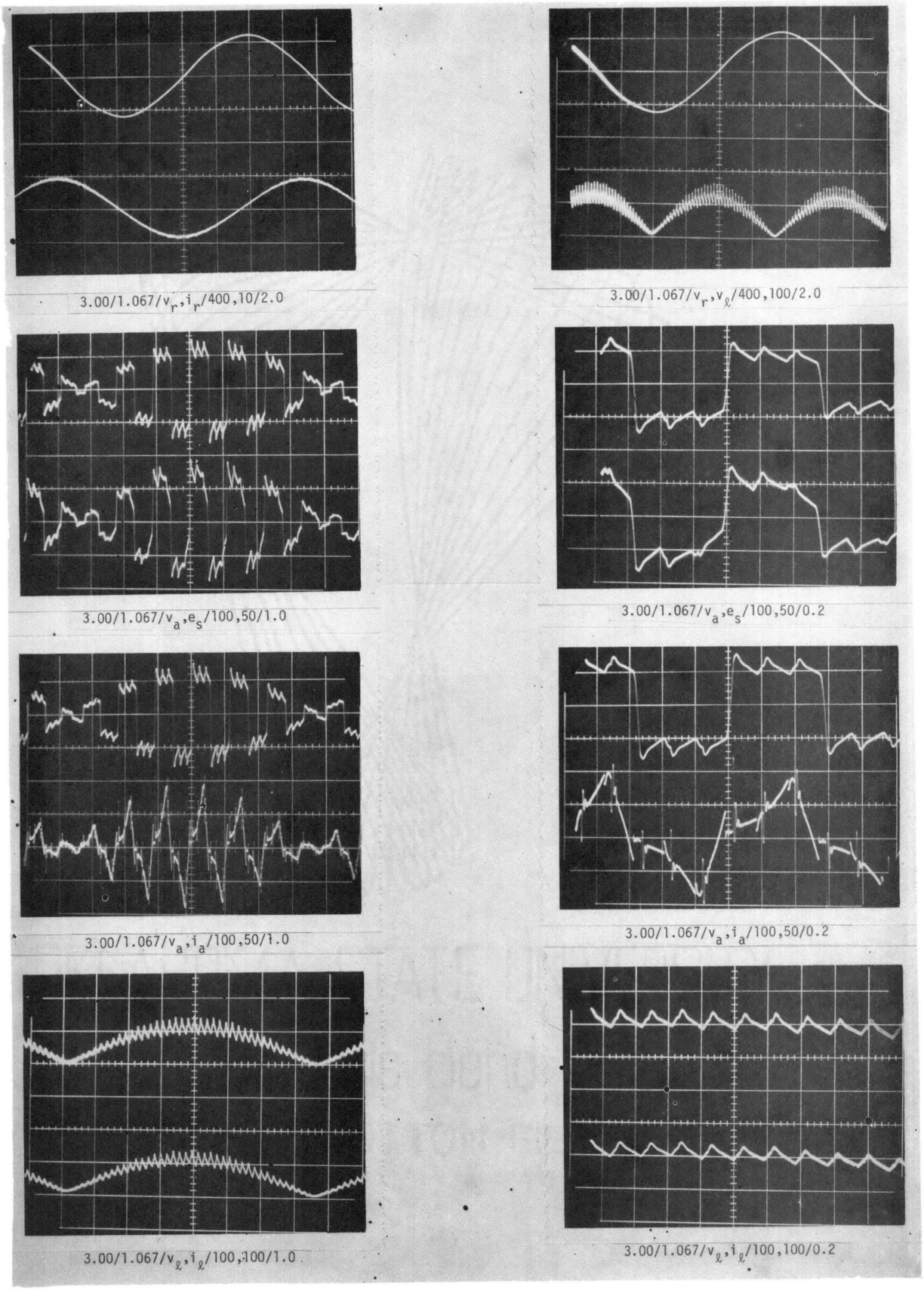

Figure 61. FMGS Waveforms Under Load (X_L/X_C = 0.0300; X_L/R_ℓ = 1.696)

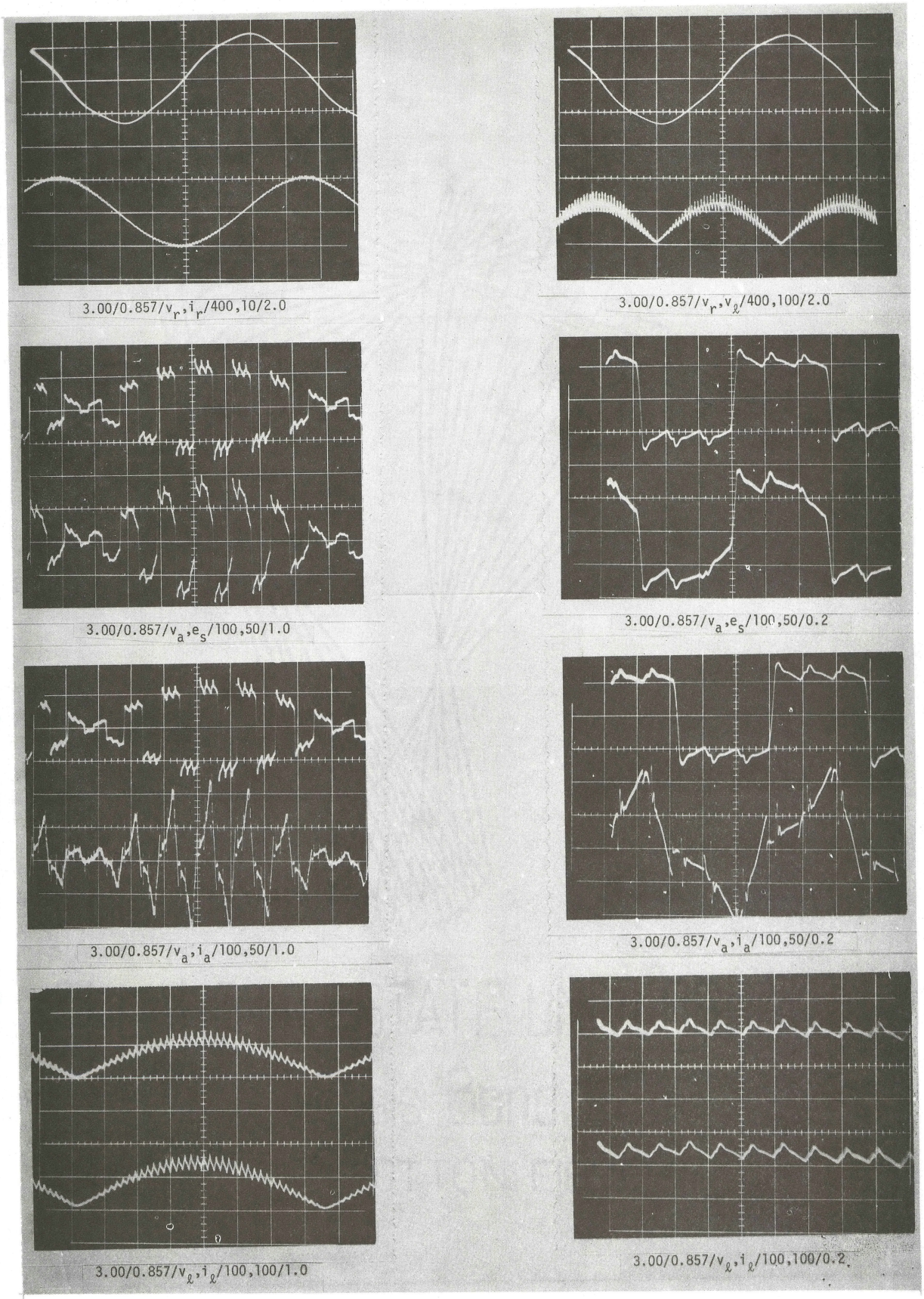

Figure 62. FMGS Waveforms Under Load (X_L/X_C = 0.0297; X_L/R_ℓ = 2.102)

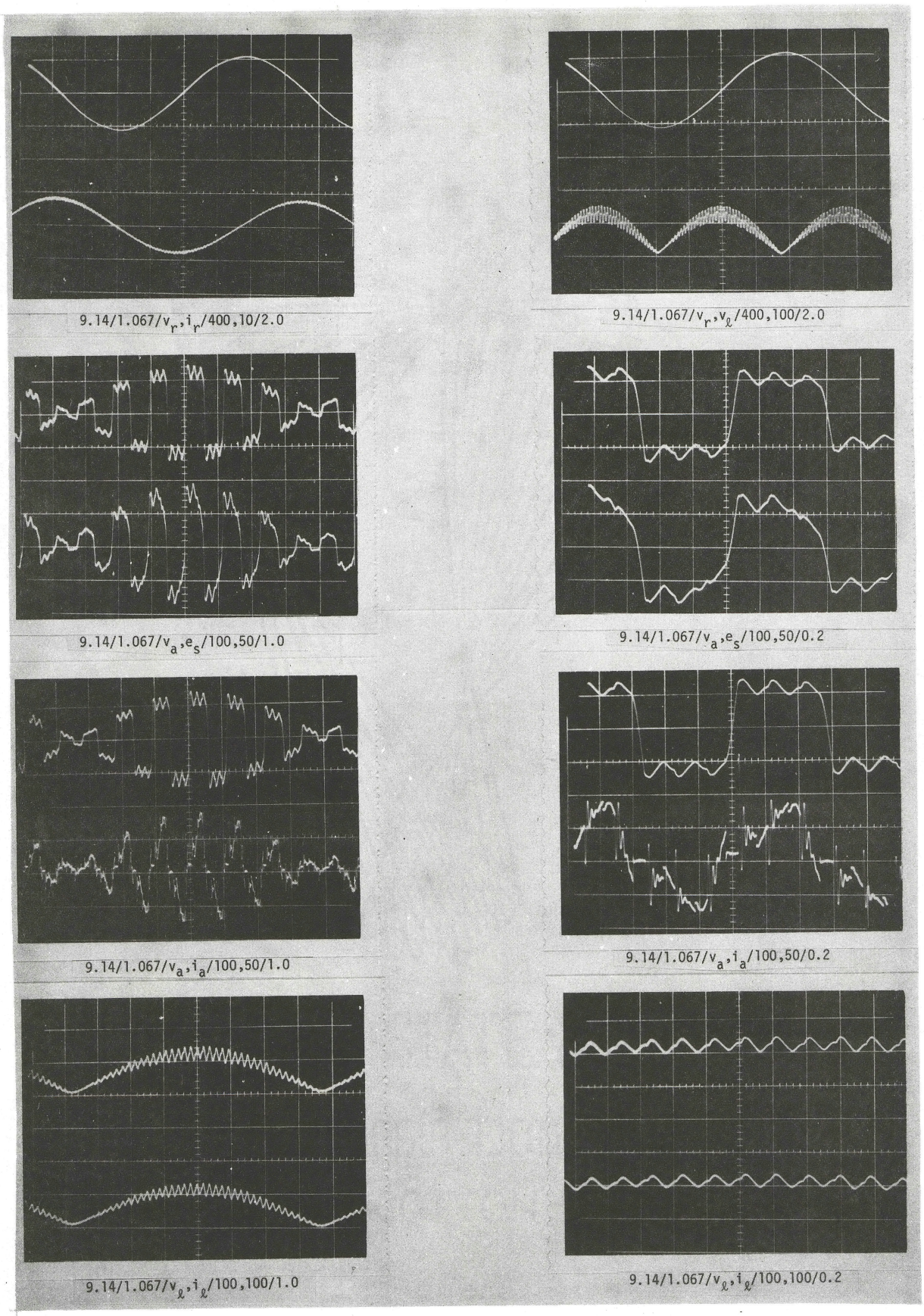

Figure 63. FMGS Waveforms Under Load (X_L/X_C = 0.0914; X_L/R_ℓ = 1.696)

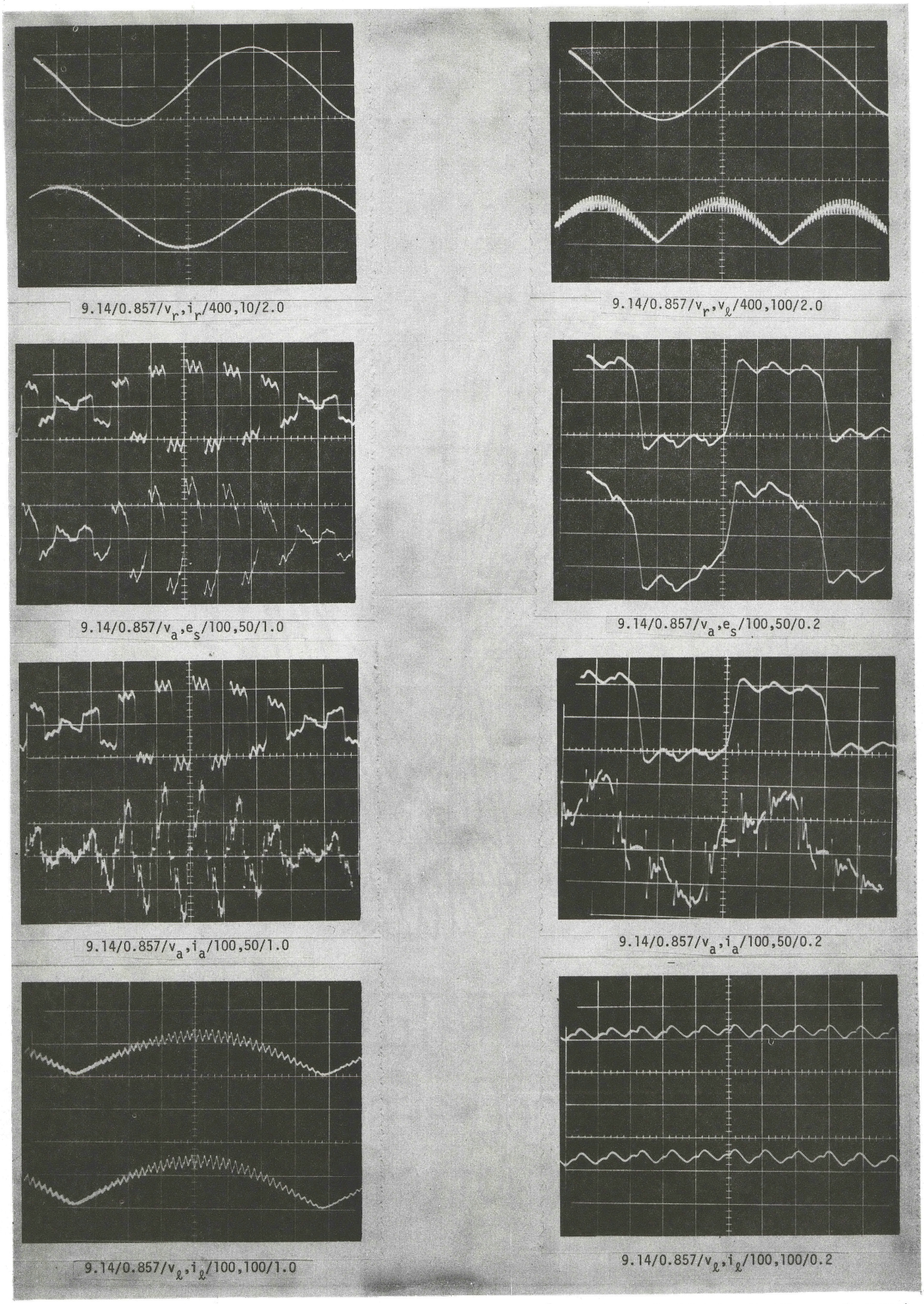

Figure 64. FMGS Waveforms Under Load (X_L/X_C = 0.0905; X_L/R_ℓ = 2.102)

(E) Sample Calculation and Results

Some of the equations developed in Chapter III are used to compute theoretical values of quantities investigated. Slight modifications are necessary to consider a 'p' pole instead of a 2 pole machine.

Initial data:

$$R_\ell = 1.067\ \Omega$$

$$C = 3.00\ \mu F$$

$$\omega_r = 5526\ \text{rad/sec}$$

$$V_\ell = 116.8\ V$$

$$I_\ell = 109.5\ A$$

$$C_4 = 89.65\ \mu F$$

Calculations:

$$X_L = (5526)(0.3274 \times 10^{-3}) = 1.809\ \Omega$$

$$X_C = ((5526)(3.00 \times 10^{-6}))^{-1} = 60.32\ \Omega$$

$$(X_L/R_\ell) = (1.809/1.067) = 1.696$$

$$(X_L/X_C) = (1.809/60.320) = 0.030$$

The following values are read from Figures 13. 24, 25 and 8.

$$K_{\ell o} = 1.096$$

$$K_{a1} = 0.581$$

$$\phi_{a1} = 9.13^\circ$$

$$\beta = 25.33^\circ$$

$$\phi_1 = \phi_{a1} + \beta = 34.46^\circ$$

I_1 and E_1 can now be calculated.

$$I_1 = \frac{K_{a1}\ I_\ell}{K_{\ell o}} = \frac{0.581 \times 109.5}{1.096} = 58.05\ A$$

$$E_1 = \frac{X_L\ I_\ell}{K_{\ell o}} = \frac{1.809 \times 109.5}{1.096} = 180.7\ V$$

The various magnetomotive forces are calculated next.

$$M_a = \frac{3}{2p}\frac{4}{\pi} N_s I_1 k_p k_d$$

$$= \frac{3}{2 \times 16}\frac{4}{\pi} (64 \times 58.05 \times 1 \times 1) = 443.5 \text{ At/pole}$$

$$M_r = \frac{(p/2)\, g}{\mu_o \ell d N_s k_p k_d}$$

$$= \frac{(16/2)(0.00151)}{(4\pi \times 10^{-7})(0.03810 \times 0.22480 \times 64 \times 1 \times 1)}$$

$$= 573.7 \text{ At/pole}$$

$$M_f = \sqrt{M_a^2 + M_r^2 + 2M_a M_r \sin \phi_1}$$

$$= \sqrt{443.5^2 + 573.7^2 + (2)(443.5)(573.7) \sin 34.46^\circ}$$

$$= 902.1 \text{ At/pole}$$

Corresponding to the air-gap line of no-load saturation curve, ratio of voltage to current is 29.57 ohms at an electrical angular frequency ω_r of 5595 rad/sec.

Therefore, $$M = \left.\frac{E_1}{\omega_r I_r}\right|_{i_a = 0} = \frac{29.57}{5595} = 0.005284 \text{ H}$$

$$k_f = \frac{(p/2)\, g\, M}{\mu_o \ell d N_s k_p k_d N_r}$$

$$= \frac{(16/2)(0.00151 \times 0.005284)}{(4\pi \times 10^{-7})(0.03810 \times 0.22480 \times 64 \times 1 \times 1 \times 120)}$$

$$= 0.7723$$

Since, $$M_f = N_r I_r k_f$$

$$I_r = \frac{M_f}{N_r k_f} = \frac{902.1}{120 \times 0.7723} = \underline{\underline{9.73 \text{ A}}}$$

$$\delta = \cos^{-1}\left[\frac{M_r + M_a \sin \phi_1}{M_f}\right]$$

$$= \cos^{-1}\left[\frac{573.7 + 443.5 \sin 34.46^\circ}{902.1}\right] = 23.91^\circ$$

$$L_{re} = L_r - \frac{3}{2} M \frac{I_1}{I_r} \sin(\phi_1 + \delta)$$

$$= 0.1843 - (\frac{3}{2})(0.005284)(\frac{58.05}{9.73}) \sin(34.46^\circ + 23.91^\circ)$$

$$= 0.1440 \text{ H}$$

$$V_r = \omega_m L_{re} I_r = 120\pi \times 0.1440 \times 9.73 = \underline{\underline{528.5 \text{ V}}}$$

$$I_e = |I_r - V_r \omega_m C_4|$$

$$= |9.73 - 528.5 \times 120\pi \times 89.65 \times 10^{-6}|$$

$$= \underline{\underline{8.13 \text{ A}}}$$

Theoretical and experimental values of I_r, V_r and I_e are listed in Table IV. Theoretical values were obtained by computations similar to the sample calculation shown above. Maximum deviations in the magnitudes of I_r, V_r and I_e are 15.3, 12.2 and 12.1 per cent, respectively.

4.4 Discussion of Experimental Results

The series of experimental investigations started with the study of the operation of PBRS with bridge-input capacitors under resistive loads. This particular experiment provided a wealth of data and, more importantly, a good insight to the behavior of PBRS with bridge-input capacitors. This data also enables the verification of the mathematical results by two different methods. Experimental waveforms and values of angles γ and β (refer Figure 55) agree fairly well with theoretical predictions. Comparison of experimental and theoretical values of Id and E_d (refer Table II) show good agreement (deviations less than 9.67 per cent). Results (Table IV) of FMGS experiments also show good agreement between experimental and theoretical values of I_r, V_r and I_e.

TABLE IV

THEORETICAL & EXPERIMENTAL VALUES OF I_r, V_r & I_e FOR FMGS

C (μF)	3.00			5.27			9.14		
Nbr of Lamps in Parallel @1500W, 120V	8	9	10	8	9	10	8	9	10
I_ℓ (A, 0-peak)	109.5	122.9	136.4	109.5	122.9	136.4	109.5	122.9	136.4
V_ℓ (V, 0-peak)	116.8								
R_ℓ (ohm)	1.067	0.950	0.857	1.067	0.950	0.857	1.067	0.950	0.857
X_L/R_ℓ	1.696	1.899	2.102	1.696	1.899	2.102	1.696	1.899	2.102
X_L/X_C	0.0300	0.0298	0.0297	0.0527	0.0525	0.0522	0.0914	0.0909	0.0905
Theoretical I_l(A, 0-peak)	58.05	64.94	72.18	58.45	65.36	72.45	59.74	66.93	74.05
Theoretical E_l(V, 0-peak)	180.7	189.3	195.9	171.4	179.5	186.2	156.8	166.5	174.0
Theoretical I_r(A, 0-peak)	9.73	10.65	11.51	9.32	10.22	11.10	8.76	9.75	10.68
Experimental I_r(A,0-peak)	9.10	9.69	10.31	8.63	9.19	9.83	8.03	8.64	9.26
Deviation in I_r(%)	+6.92	+9.94	+11.72	+8.00	+11.15	+12.95	+9.15	+12.81	+15.33
Theoretical V_r(V,0-peak)	528.5	569.9	607.1	500.2	540.5	578.9	459.3	504.9	546.2
Experimental V_r(V,0-peak)	506.2	522.5	540.9	485.7	502.0	520.4	457.5	473.7	490.7
Deviation in V_r(%)	+4.40	+9.08	+12.23	+2.98	+7.66	+11.25	+4.04	+6.58	+11.30
Theoretical I_e(A,0-peak)	8.13	8.61	9.01	7.59	8.05	8.47	6.77	7.31	7.78
Experimental I_e(A,0-peak)	8.41	8.40	8.37	8.26	8.25	8.22	7.69	7.67	7.63
Deviation in I_e(%)	-3.29	+2.55	+7.65	-8.09	-2.35	+3.03	-12.06	-4.67	+1.93

Main sources of disparity are: a) numerical errors inherent in the evaluation of angles γ and β, integration constants k_1, k_2, k_5 and k_6 and Fourier coefficients; b) harmonics in the machine (source) waveforms; c) instrumentation and measurement errors; and d) deviations inherent in the idealizing assumptions.

In spite of the many sources of errors, correlation between theory and experiment is fairly good and departures are within acceptable limits, thus supporting the validity and usefulness of the idealized models developed.

CHAPTER V

SUMMARY AND CONCLUSIONS

5.1 Summary of Results and Conclusions

The primary objective of this thesis work was to analyze and develop a mathematical model for the field modulated generator system (FMGS). Absence of previous work on modeling this specific system made it logical, as a first step, to develop an idealized model to understand the interaction of basic factors involved in its operation. The task of FMGS modeling was performed in steps as follows: a) split the system into two sub-systems, namely, field modulated alternator and parallel-bridge rectifier system (PBRS), formulate and analyze circuit models for each sub-system using certain idealizing and simplified assumptions; b) tie the two sub-systems together to form an idealized model for FMGS; and c) experimentally verify the validity of the mathematical model developed.

The development of an idealized mathematical model for FMGS appears to be fairly successful. This model, in spite of many idealizing assumptions made, gives results which agree with experimental observations within allowable limits. As such, the results of this research have laid a basis for further work and provide guidelines for better design, scale-up, and control of this system.

It is apparent from the system configuration that the PBRS is

central to the operation of the FMGS. Therefore, a thorough analysis of PBRS is the necessary first step in the overall system modeling. Chapter II describes in detail the methods (analytical and numerical) employed in deriving mathematical expressions for various current and voltage waveforms and in evaluating the harmonic content (magnitudes and phase angles) of the waveforms of interest in PBRS (with bridge-input capacitors and resistive loads). Equations derived and plots of numerical results of harmonic analysis are presented for $\infty > (X_L X_C/R_\ell^2) > 36$.

Circuit differential equations are linear for each of the six time intervals into which the high-frequency half-cycle is divided for the purpose of analysis. However, all the equations formulated to find angles γ and β and the integration constants k_1, k_2, k_5 and k_6 are not linear. Therefore, an iterative method was used to solve the simultaneous linear and non-linear equations separately in order to increase computational efficiency and decrease numerical errors. Marquardt's algorithm for least-square estimation of non-linear parameters was employed in the solution of angles γ and β. Integration constants and angles evaluated by this process as well as phase angles and normalized magnitudes of Fourier components are plotted in terms of circuit constant ratios (X_L/X_C) and (X_L/R_ℓ) as parameters.

Chapter III introduces the assumptions made in the development of the idealized FMGS model. Results of PBRS studies derived in Chapter II are utilized to formulate relationships which can be used to find E_1 and I_1 with or without modulation for given load condition (V_ℓ, I_ℓ and R_ℓ) and circuit parameters (X_L/X_C and X_L/R_ℓ). Key equations for field modulated alternator model are developed by assuming E_1 and I_1 are known.

FMGS model is formed by tying these two sub-systems together via

the common link--E_1 and I_1. Employing the FMGS model developed in this Chapter, one can find all the important performance characteristics and optimize certain design parameters for specified (resistive) load conditions.

Low frequency (ω_m) equivalent circuit developed (refer Figure 44) provides a convenient tool for studying problems involved in interfacing FMGS with power grids. High frequency (ω_r) vector diagram (refer Figure 46) illustrates relationships between bridge-input voltage (or current), air gap MMF and induced EMF. This vector diagram, in combination with the low frequency (ω_m) vector diagram (refer Figure 47) gives vital information leading to an understanding of the interactions of fundamental parameters in the operation of the FMGS.

Experimental investigations have shown (References 14 and 23) that the use of proper bridge-input capacitors will decrease excitation requirements and improve efficiency and regulation of a field modulated alternator. However, these capacitances must be carefully selected to avoid excessive losses that may occur in the source (alternator) due to the flow of circulating currents in the closed paths provided by the capacitors.

It is appropriate at this point to formulate a rule-of-thumb for the selection of a proper (X_L/X_C) range within which FMGS will operate optimally. From equation (2.4.5), the normalization factor K is defined as the maximum value of source (stator) current per phase when the bridge-input terminals are shorted. Based on this definition, equation (3.3.2) suggests that an alternator operated at $K_{al} = 1$ implies $I_1 = K$, namely, the alternator is operated with its stator phase current equal to the short-circuit current. As an alternator is not designed to

operate continuously at $K_{al} \geq 1$, operating FMGS under such a condition would entail excessive heating and eventual destructive damage. Therefore, it is proper that FMGS be operated at $K_{al} < 1$. To meet this requirement, comparison of theoretical curves of $K_{\ell o}$ (Figure 13) and K_{al} (Figure 24) and Figure 54 indicates that the upper limit for (X_L/X_C) be less than 0.2. This is equivalent to saying that the optimum choice for (X_L/X_C) is given by

$$0 < (X_L/X_C) < 0.2 \qquad (5.1.1)$$

In addition to the above, one should avoid resonant conditions $(X_L/X_C = 1)$ caused by either harmonic currents or operating speed changes. For example, if the field modulated alternator is operated in the speed range of 2:1 and the n-th harmonic (n = 1 represents fundamental) is of particular concern, then the choice of (X_L/X_C) is further restricted by the condition given below.

$$(X_L/X_C) = \min \{1/(2n)^2 \ , \ 0.2\} \qquad (5.1.2)$$

Within the limits set by (5.1.1) and (5.1.2), several bridge-input capacitances should be considered and the one which yields the best theoretical performance under specified conditions should be selected.

Normal operating range of FMGS in terms of (X_L/R_ℓ) can be expressed as follows.

$$\sqrt{3} \leq (X_L/R_\ell) \qquad (5.1.3)$$

The lower limit, $\sqrt{3}$, is determined by full conduction of PBRS which would then result in nearly square waveform for bridge-input voltages (References 21 and 22). The upper limit is conditioned by other factors such as the choice of (X_L/X_C) value and alternator rating. However, based on the experience gained by operating several available

prototypes, it is concluded that if the choice of (X_L/X_C) is less than 0.2, then the upper limit for (X_L/R_ℓ) lies around 4.0.

Chapter IV starts with a documentation of the experimental investigations conducted for studying the effect of varying bridge-input capacitance and load resistance values over a wide range on various current and voltage waveforms and regulation characteristics of PBRS under resistive load conditions. It is followed by experiments performed with an available 20 kVA alternator prototype to verify the idealized FMGS model developed. Four data points were chosen to correlate experimental and theoretical values of γ and β for the PBRS model. Maximum deviations in γ, β, I_d and E_d values were 9.8, 17.9, 6.79 and 9.67 per cent, respectively. Nine data points were chosen to compare experimental and theoretical values of I_r, V_r and I_e. Deviations were less than 15.73 per cent. For each investigation, experimental approach and setup, recorded data (including oscillograms) and results analyzed are presented and the sources of errors are discussed in detail. On the whole, the results showed that correlation between theory and experiment is fairly good, thus supporting the validity of the idealized model developed.

5.2 Scope for Further Work

Extension of this thesis research is recommended in several areas. Study of PBRS with bridge-input capacitors under resistive load conditions should be extended to include the region $(X_L X_C/R_\ell^2) \leq 36$. PBRS studies (with bridge-input capacitors) should be further extended to include: a) non-resistive load conditions with sinusoidal source voltages; b) both resistive and non-resistive load conditions with non-sinusoidal source voltages; and c) effects of non-ideal solid state

devices and non-ideal switching.

Idealizing assumptions made to develop FMGS model should be relaxed one by one or in groups to make the model more realistic. Some items of particular interest for further studies are: a) the expression of X_L in terms of machine physical characteristics and circuit parameters; b) saturation effects in magnetic circuits by considering X_L as function of load, machine physical characteristics and circuit parameters, and X_r as a function of rotor current; c) influence of non-sinusoidal machine field form; d) effects of phase-shifts in modulation envelopes on the operation of the system as a whole; and e) inclusion of transformer voltages in the machine stator windings. Extensive opportunities exist for further research in the areas of output filtering, transient behavior and stability and control aspects of FMGS employed independently and in parallel with power grids under a multitude of practical operating conditions.

Considerable progress has been made in this thesis towards developing understanding of field modulated generator systems. The idealized model developed and the supporting experimental investigations have laid a solid foundation for further analyses and improvements that are yet to come.

SELECTED BIBLIOGRAPHY

[1] MacNeil, C. I. "Electrical Apparatus." U.S. Patent No. 2,659,044 November 1953.

[2] Owen, T. B. "Variable-Speed Constant-Frequency Devices: A Survey of the Methods in Use and Proposed." AIEE Transactions (Part II. Applications and Industry), Vol. 78 (November 1959), pp. 321-326.

[3] Chirgwin, K. M. and L. J. Stratton. "Variable-Speed Constant-Frequency Generator System for Aircraft." AIEE Transactions (Part II. Applications and Industry), Vol. 78 (November 1959), pp. 304-310.

[4] Hoard, B. V. "Constant-Frequency Variable-Speed Frequency-Make-Up Generators." AIEE Transactions (Part II. Applications and Industry), Vol. 78 (November 1959), pp. 297-304.

[5] Kimbark, E. W. Direct Current Transmission. Vol. I., New York: John Wiley and Sons, 1971.

[6] Adkins, B. and W. J. Gibbs. Polyphase Commutator Machines. London: Cambridge University Press, 1951.

[7] Daniels, A. R. The Performance of Electrical Machines. London: McGraw-Hill, 1968.

[8] Jesse, R. D. and W. J. Spaven. "Constant-Frequency A-C Power Using Variable Speed Generation." AIEE Transactions (Part II. Applications and Industry), Vol. 78 (January 1960), pp. 411-418.

[9] Chirgwin, K. M., L. J. Stratton and J. R. Toth. "Precise Frequency Power Generation from an Unregulated Shaft." AIEE Transactions (Part II. Applications and Industry), Vol. 79 (January 1961), pp. 442-451.

[10] Bird, B. M. and J. Ridge. "Amplitude-Modulated Frequency Changer." Proceedings IEE, Vol. 119, No. 8 (August 1972), pp. 1155-1161.

[11] Wickson, A. K. "A Simple Variable Speed Independent Frequency Generator." Proceedings AIEE Summer and Pacific General Meeting and Air Transportation Conference, Seattle, Washington, Paper No. CP 59-915 (June 1959).

[12] Bernstein, T. and N. L. Schumitz. "Variable Speed Constant Frequency Generator Circuit Using a Controlled Rectifier Power Demodulator." Proceedings AIEE Pacific General Meeting, San Diego, California, Paper No. CP 60-1053 (August 1960).

[13] Hughes, W. L., H. J. Allison and R. Ramakumar. "Apparatus for Providing A-C Electrical Energy at a Preselected Frequency." U.S. Patent No. 3,663,945.

[14] Ramakumar, R., H. J. Allison and W. L. Hughes. "Description and Performance of a Field Modulated Frequency Down Converter." 1972 SWIEEECO Record, IEEE Catalog No. 72 CHO 595-9 SWIECO (April 1972), pp. 252-256.

[15] Allison, H. J., R. Ramakumar and W. L. Hughes. "A Field Modulated Frequency Down Conversion Power System." IEEE Transactions on Industry Applications, Vol. IA-9, No. 2 (March/April 1973), pp. 220-226.

[16] Ramakumar, R., H. J. Allison and W. L. Hughes. "A Self-Excited Field Modulated Three-Phase Power System." IEEE Conference Paper No. C 74-318-2, Summer Power Meeting, Anaheim, California (July 1974).

[17] American Institute of Electrical Engineers. The Bibliography on Electric Power Converters. New York, February 1950.

[18] Dortort, I. K. "Extended Regulation Curves for 6-Phase Double-Way and Double-Wye Rectifiers." AIEE Transactions (Commun. Electron.), Vol. 72 (May 1953), pp. 192-202.

[19] Witzke, R. L., J. V. Kresser and J. K. Dillard. "Influence of A-C Reactance on Voltage Regulation of 6-Phase Rectifiers." AIEE Transactions (Commun. Electron.), Vol. 72 (July 1953), pp. 244-253.

[20] Ross, M. D. and J. W. Batchelor. "Operation of Nonsalient-Pole-Type Generators Supplying a Rectified Load." AIEE Transactions, Vol. 62 (November 1943), pp. 667-670.

[21] Ramakumar, R., H. J. Allison and W. L. Hughes. "Analysis of the Parallel-Bridge Rectifier System." IEEE Transactions on Industry Applications, Vol. IA-9, No. 4 (July/August 1973), pp. 425-436.

[22] Ramakumar, R., H. J. Allison and W. L. Hughes. "Operation of Alternators with Parallel-Bridge Rectifier Systems." IEEE Transactions on Power Apparatus and Systems, Vol. PAS-92, No. 5 (September/October 1973), pp. 1679-1687.

[23] Tsung, Chi-Cheng and R. Ramakumar. "Operation of Parallel-Bridge Rectifier Systems with Capacitors at Bridge Inputs." Midwest Power Symposium Conference Record, Vol. II, University of

Missouri-Rolla, Rolla, Missouri (October 1974).

[24] Tsung, C. C. and R. Ramakumar. "A Study of the Parallel-Bridge Rectifier System with Bridge-Input Capacitors." Proceedings of the 10th Annual Meeting of the IEEE Industry Applications Society, IEEE Catalog No. 75 CHO 999-3 IA, Atlanta, Georgia (September/October 1975), pp. 1012-1019.

[25] Marquardt, D. W. "An Algorithm for Least-Squares Estimation of Nonlinear Parameters." J. Soc. Indust. Appl. Math., Vol. 11, No. 2 (June 1963), pp. 431-441.

[26] Carnahan, B., H. A. Luther and J. O. Wilkes. Applied Numerical Methods. New York: John Wiley and Sons, 1969.

[27] Harnden, J. D., Jr. and F. B. Golden, Editors. Power Semiconductor Applications, Vol. I and II. New York: IEEE Press, 1972.

[28] Ramakumar, R. and C. C. Tsung. "An Approach to Model Field Modulated Generator Systems." Midwest Power Symposium Conference Record, University of Akron, Ohio (October 1975).

[29] Fitzgerald, A. E., C. Kingsley, Jr. and A. Kusko. Electric Machinery. New York: McGraw-Hill, 1971.

[30] Messerle, H. K. Dynamic Circuit Theory. Oxford, New York: Pergamon Press, 1965.

[31] Tsung, C. C. and R. Ramakumar. "Idealized Model of Field Modulated Generator Systems: An Experimental Study." Midwest Power Symposium Conference Record, Kansas State University, Manhattan, Kansas (October 1976).

VITA

Chi-Cheng Tsung

Candidate for the Degree of

Doctor of Philosophy

Thesis: A STUDY OF THE FIELD MODULATED GENERATOR SYSTEM

Major Field: Electrical Engineering

Biographical:

Personal Data: Born in Yi-Lan County, Taiwan, China, on January 10, 1934, the son of Mr. and Mrs. Tai-Si Tsung.

Education: Graduated from Yi-Lan Middle School, Yi-Lan City, Taiwan, in June, 1950; received the Diploma in Electrical Engineering from Taiwan Provincial Taipei Institute of Technology, in July, 1957; received the Master of Science degree in Electrical Engineering from Oklahoma State University in May, 1972; completed requirements for the Doctor of Philosophy degree at Oklahoma State University with a major in Electrical Engineering, in December, 1976.

Professional Experience: Communication Officer, Chinese Air Force Communication Electronics School, Kaohsiung, Taiwan, September, 1955 to September 1956; Teaching Assistant, Electronics Circuit Laboratory, Department of Electrical Engineering, Taiwan Provincial Taipei Institute of Technology, September 1956 to February 1957; Electrical Project Engineer, Military Construction Bureau, Taipei, Taiwan, March 1957 to April 1967; Electrical Engineer, Taiwan Fertilizer Company, Taipei, Taiwan, May 1967 to August 1969; Graduate Research Assistant, School of Electrical Engineering, Oklahoma State University, Stillwater, Oklahoma, September 1972 to September 1976.

Professional Organizations: Member of the Institute of Electrical and Electronics Engineer, Eta Kappa Nu, Chinese Institute of Engineers.